Modulation of the electrocatalytic activity for H2 production and CO2 reduction with bio-inspired MFe (Ni and Co) complexes

Lili Sun

THÈSE

Pour obtenir le grade de

DOCTEUR DE L'UNIVERSITÉ GRENOBLE ALPES

École doctorale : CSV- Chimie et Sciences du Vivant
Spécialité : Chimie inorganique et Bio inorganique
Unité de recherche : Département de Chimie Moléculaire

Modulation de l'activité électrocatalytique pour la production de H2 et la réduction du CO2 avec des complexes MFe (Ni et Co) bio-inspirés

Modulation of the electrocatalytic activity for H2 production and CO2 reduction with bio-inspired MFe (Ni and Co) complexes

Présentée par :

Lili SUN

Direction de thèse :

Carole DUBOC — Directrice de thèse
chercheur CNRS, Université Grenoble Alpes

Rapporteurs :

Jalila SIMAAN
DIRECTRICE DE RECHERCHE, CNRS délégation Provence et Corse
Nicolas LE POUL
DIRECTEUR DE RECHERCHE, CNRS délégation Bretagne et Pays de la Loire

Thèse soutenue publiquement le **16 décembre 2022**, devant le jury composé de :

Carole DUBOC DIRECTRICE DE RECHERCHE, CNRS délégation Alpes	Directrice de thèse
Jalila SIMAAN DIRECTRICE DE RECHERCHE, CNRS délégation Provence et Corse	Rapporteure
Nicolas LE POUL DIRECTEUR DE RECHERCHE, CNRS délégation Bretagne et Pays de la Loire	Rapporteur
Anne MILET PROFESSEUR DES UNIVERSITES, Université Grenoble Alpes	Présidente

Acknowledgment

Time flies and my PhD studies are coming to an end. I came to this beautiful city more than three years ago, and everything here was full of mystery and novelty to me. In spring, I enjoy the blooming of different flowers. In summer, I watch the ever-flowing Isère River and enjoy a barbecue with my friends on “l'Île d'Amour”. In autumn, I pick chestnuts and feel the gift of nature. In winter, I look up at the vast snow-capped mountains, travel freely on the snow-capped mountains, and enjoy the fun of skiing. Of course, I also experienced the outbreak of the new coronavirus and some unexpected situations during this period, which made me feel panic. As the saying goes, time is the best medicine. As time goes by, I can devote myself to life and study again with a peace of mind. These three years have given me a lot.

First of all, I would like to express my sincerest gratitude to my supervisor. It was she who gave me a chance to study at this university. Her patience and careful guidance have greatly improved my thesis writing and gained more professional knowledge.

Second, I really appreciate Marcello's help with my experiments; he always gave me very helpful advice. I am also very grateful to the technical staff for their help with the testing of my samples and data analysis. Then I would like to thank my colleagues in the lab for their help, which enriched my study life.

Third, I would like to thank my parents and brother for their understanding and support, allowing me to study and live here without worries. Then I am very grateful to my boyfriend for his company and help over the past three years. Without him, my parents would be very worried about me in a faraway country.

Finally, thanks to my own perseverance and courage.

Abstract

Hydrogen is recognized as a clean energy carrier, and thus it is being considered a promising alternative to fossil fuels as the next-generation fuel for powering cars, heating homes, and generating electricity. At present, hydrogen is mainly produced from fossil fuels. Currently, water splitting is an appealing approach to produce high-purity H_2, owing to its clean and sustainable process, but relies on Pt-based materials. However, the high price and rarity of Pt prevent its large-scale use. Designing a non-noble metal-free catalytic system is thus needed under the premise of ensuring catalytic activity. In nature, the [NiFe] and [FeFe] hydrogenases (H_2ases) catalyze the production of H_2 reversibly by reducing protons. Some chemists have been inspired by these H_2ases to design molecular electrocatalysts for H_2 production. They focused their efforts not only on mimicking the organometallic complexes responsible for the reactivity present in the active site of the enzymes but also on understanding the mechanism in order to define the key active structural features that ensure their efficiency. To date, many bio-inspired complexes have been designed for H_2 production, but they still need to be optimized for future applications, especially regarding their performance and stability.

CO_2 represents a potential feedstock for the synthesis of value-added fine chemicals and fuels because of its low cost, high abundance, and relative ease of transport. Electrocatalytic CO_2 reduction is thus an attractive pathway to convert CO_2 into organic fuels and useful chemicals. Many electrocatalysts have also been used to catalyze CO_2 reduction. There are also enzymes in nature that can activate, including the NiFe carbon monoxide dehydrogenase (NiFeCODH). CODH reduces CO_2 to CO reversibly close to the thermodynamic potential. In addition, it is noted that the active sites of these two enzymes, the NiFe-CODH and NiFe-H_2ase, display similar key structural features. Their catalytic processes both involve electron and proton transfer as well as synergy between the Ni and Fe sites.

However, the performance of these catalysts is still not comparable to the natural systems ([FeFe] and [NiFe] H_2ases, and NiFeCODH). Fortunately, an understanding of the mechanisms has contributed to providing guidance for the further design of highly active electrocatalysts for H_2 production and CO_2 reduction. In previous works, a family of NiFe and FeFe electrocatalysts has been synthesized, which display similar catalytic performance for H_2 production under similar conditions. Besides, the $Ni^{II}Fe^{II}Cp$ complex can catalyze H_2 production and CO_2 reduction in an acidic aqueous solution after its immobilization on graphite electrodes. Therefore, bio-inspired catalysts of H_2ases have been also used successfully to catalyze CO_2 reduction.

Inspired by the above works, the aim of this thesis is to improve the electrocatalytic activity of these systems by lowering the overpotential for H_2 production and CO_2 reduction. We mainly investigated the redox properties of complexes and their catalytic activities from two aspects, namely the impact of the metal and the design of the ligands.

Firstly, the Ni ion has been substituted by a Co ion to synthesize the corresponding CoFe complex. Unfortunately, it displays no electrocatalytic activity in DMF for H_2 production.

Second, we has modified the $Ni^{II}Fe^{II}Cp$ complex at the Fe site with the introduction of a potential proton relay in the second coordination sphere, by replacing the Fe-bound cyclopentadienyl (Cp) with the picolyl cyclopentadienyl (PyCp) and 2-(diethylamino)ethyl-cyclopentadienide (CpN), to synthesize the NiFeCpPy, NiFeCpN and CoFeCpNH complexes. Both the NiFeCpN and CoFeCpNH complexes display catalytic activity in the presence of Et_3NHBF_4 for H_2 production. NiFeCpN has a lower overpotential than the parent $Ni^{II}Fe^{II}Cp$ complex. These data evidence that the pendant amine play an important role in the electrocatalytic activity for H_2 production. Then, the new NiFeCpN and CoFeCpNH complexes containing a pendant amine also display activity for CO_2 reduction under homogeneous and heterogeneous conditions.

Keywords: hydrogenases, NiFe carbon monoxide dehydrogenase, H_2 production, CO_2 reduction, bio-inspired complexes

Abbreviations

adt	Azadithiolate
APCI	Atmospheric-pressure chemical ionization
ATR	Attenuated total reflectance
bdt	benzene-1,2-dithiolato
CH_2Cl_2	Dichloromethane
Cp	Cyclopentadienide
Cp*	Pentamethylcyclopentadiene
CV	Cyclic voltammetry
DFT	Density functional theory
DMF	Dimethylformamide
dppbz	1,2-bis(diphenylphosphino)benzene
dppe	1,2-bis(diphenylphosphino)ethane
dppv	1,2-bis(diphenylphosphino)ethylene
E_{cat}	Catalytic potential
edt	1,2-ethanedithiolate
E_{pa}	Anodic peak potential
E_{pc}	Cathodic peak potential
EPG	Edge-plane graphite
EPR	Electron paramagnetic resonance
eq	Equivalent
ESI	Electrospray ionization
Et	Ethyl
Et_3NHBF_4	Triethylammonium tetrafluoroborate
Fc	Ferrocene
FE	Faradaic efficiency
H_2ase	Hydrogenase
HBF_4	Fluoroboric acid
HER	Hydrogen evolution reaction
HOAc	Acetic acid
HOTs	Toluenesulfonic acid
i_{cat}	Catalytic current
i_p	Reductive peak current
IR	Infrared
KPF_6	Potassium hexafluorophosphate
Me	Methyl
MeCN	Acetonitrile
MS	mass spectrum
NMR	Nuclear Magnetic Resonance
odt	oxydimethanethiolate
pdt	1,3-propanedithiolate
Ph	Phenyl
Py	Pyridine

TFA	2,2,2-Trifluoroacetic acid
TFE	2,2,2-Trifluroroethanol
THF	Tetrahydrofuran
UV-vis	Ultraviolet–visible
η	Overpotential

Table of Content

Chapter l Introduction

1.1 H_2 production

With the development and progress of society, human beings are increasingly demanding energy, which has led to the depletion of fossil energy and environmental pollution. Therefore, the development of efficient, clean, and renewable energy has become a research hotspot for researchers in many countries. Hydrogen is a recognized clean energy carrier, and thus it is being considered a promising alternative to fossil fuels as the next-generation fuel for powering cars, heating homes, and generating electricity.[1] At present, hydrogen is mainly produced from natural gas and oil by a steam reforming process, which accelerates the consumption of fossil energy and emits large amounts of CO_2, which is not conducive to sustainable development strategies.[2, 3] Therefore, the environmentally friendly production of H_2 is one of the major challenges facing our society in the next decade. In the face of this urgency, all strategies must be studied and explored to find alternatives to current industrial technologies. Water splitting is considered as a promising method to generate high-purity hydrogen. So far, Pt-based materials are still advanced and efficient catalysts for electrochemical H_2 production.[4] However, its high price and rare prevent its large-scale use. Designing a non-noble metal-free catalytic system is needed under the premise of ensuring catalytic activity.

Nature can provide sources of inspiration. Microorganisms use enzymes, the hydrogenases (H_2ases) that produce and metabolize molecular hydrogen. H_2ases catalyze H_2 production by reducing protons in a reversible manner at very high rates (one molecule of H_2ase produces between 20,000 and 1500 molecules of H_2 per second at pH 7 and 37 ℃ in water).[5] Some chemists have been inspired by H_2ases to design molecular electrocatalysts for hydrogen evolution reaction (HER).[6-10] They focused their efforts not only on mimicking the organometallic complexes responsible for the reactivity present in the active site of the enzymes but also on understanding the mechanism in order to define the key active structural features that ensure their efficiency.

According to different active sites, H_2ases are divided into two classes denoted as [NiFe] and [FeFe] H_2ases (**Figure 1.1**).[11, 12] The mechanism of each enzyme has been explored extensively over the past decade. For the active site of [FeFe] H_2ase,[13, 14] the presence of a nearby [4Fe-4S] cluster linked by a bridging thiolate is proposed to be crucial in controlling the sequence of the electron transfer processes with respect to the protonation steps. For the NiFe site,[15, 16] Ni is the only metal involved in the redox chemistry, with the iron site implicated in the generation of bridging hydride species and in the fine-tuning of the redox and electronic properties of the Ni site. The key

intermediates species are considered to be hydride species generated during the catalytic cycle, which can be found in a bridging[17, 18] or terminal coordination mode[19-21]. Moreover, the metal-bound cysteines in the [NiFe] H_2ase and the bridging pendant amine in the [FeFe] H_2ase have important roles during the catalytic process, both thiolate and amine acting as proton relays. The detailed structures and proposed mechanisms of H_2ases have been described in **Section 1.1.1**.

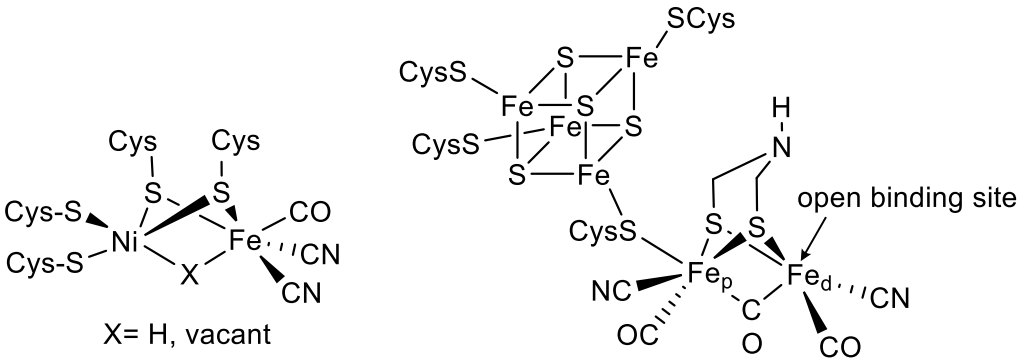

Figure 1.1 Active sites of [NiFe] and [FeFe] H_2ases.

1.1.1 Hydrogenases

1.1.1.1 The structure and function of [FeFe] H_2ase

The active site of [FeFe] H_2ase comprises a cubane [4Fe-4S] subcluster and a [2Fe] moiety linked together through a cysteine ligand (**Figure 1.1**). [5, 7, 13, 22-24] The [4Fe-4S] subcluster is a common redox cofactor, emphasizing the importance of electron transfer in the catalytic mechanism of the [FeFe] H_2ase. The two iron atoms in the [2Fe] moiety are bridged by the bridging S atoms of the azadithiolate ligand (adt^{2-} =-$SCH_2N(H)CH_2S$-) and a bridging CO ligand, and each of the iron is coordinated by one CN^- and one CO ligand. Fe^d (distal to [4Fe-4S]) of the [2Fe] moiety has a vacant site for substrate (H^-/H_2) binding, and switches between octahedral and square-pyramidal geometries during the catalytic cycle. This gives to the H-cluster some flexibility. The Fe^p (proximal to [4Fe-4S]) is connected to [4Fe-4S] cluster via the S atom of the cysteine ligand.

Based on the spectroscopic properties of the enzyme and theoretical calculations, a catalytic mechanism of [FeFe] H_2ase for H_2 reduction and oxidation reactions has been proposed, involving proton-coupled electron transfer (PCET) steps (**Figure 1.2**).[7, 8, 13] This includes the redox states and electronic structure of the H-cluster at the different steps of the cycle. The cubane [4Fe-4S] has two possible oxidation states, reduced $[4Fe\text{-}4S]^+$ and oxidized $[4Fe\text{-}4S]^{2+}$. The [2Fe] moiety has three, the reduced $Fe^I Fe^I$, the oxidized $Fe^{II}Fe^{II}$, and the mixed valence Fe^IFe^{II}. The most studied state corresponds to the "oxidized" state H_{ox} featuring a mixed valence Fe^IFe^{II} moiety and an oxidized $[4Fe\text{-}4S]^{2+}$ cluster. The H_{ox} state is characterized by a rhombic EPR signal

at g = 2.10, 2.04 and 2.00. The IR spectrum reveals vibration of the CO ligand at 1964, 1940 and 1800 cm^{-1}, and of the CN^- ligand at 2088 and 2072 cm^{-1}. When the [FeFe] H_2ase is stabilized at potentials more negative than −395 mV accompanied by a protonation process, the reduced state $H_{red}H^N$ dominates. The $H_{red}H^N$ state features an Fe^IFe^I moiety and an oxidized $[4Fe\text{-}4S]^{2+}$ cluster consistently with an EPR-silent spectrum. The IR spectrum of $H_{red}H^N$ displays vibrations of the CO ligands that are red shifted to 1935, 1891 and 1793 cm^{-1} with respect to the H_{ox} state. The protonation occurs on the N atom of the bridging amine (adt^{2-}). A third active state has been uncovered as a"super-reduced state" H_{sred} corresponding to a reduced $[4Fe\text{-}4S]^+$ cluster and a Fe^IFe^I moiety, that can be observed at or below −540 mV. Its IR spectrum features vibrations of the CO ligand (1954, 1919, and 1882 cm^{-1}) that are more similar to H_{ox} with the vibrations of CN^- ligand shifted to 2070 and 2026 cm^{-1}. The H_{sred} state isomerizes to form a terminal hydride species H_{hyd} associated with the H^+ transfer from adt^{2-} to the reduced Fe^d center. The resulting H_{hyd} state is then protonated at the bridgehead amine, leading to the ammonium hydride heterolysis product H_{ox} (H^+, H^-). Subsequently, the species H_{ox} (H^+, H^-) releases H_2, regenerating the H_{ox} state. Apparently, the amine of the azadithiolate ligand can act as a proton relay and is crucial for the transfer of protons during the catalytic process.

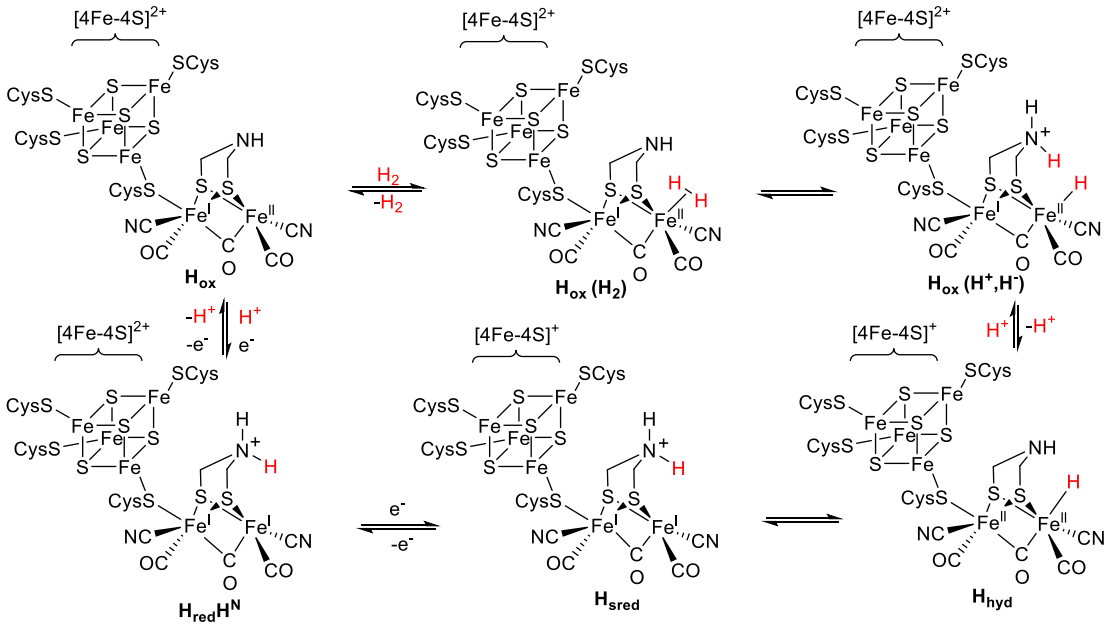

Figure 1.2 Proposed catalytic mechanism of [FeFe] H_2ase.

1.1.1.2 The structure and function of [NiFe] H_2ase

The active site of the [NiFe] H_2ase has a redox-active {Ni(S-Cys)$_4$} center, which is linked *via* two of its cysteine ligands to a redox-inactive {$Fe^{II}(CN)_2(CO)$} fragment.[7, 9, 25] Two additional cysteines from {Ni(S-Cys)$_4$} are terminally bound to the Ni ion, and the

Fe ion is coordinated by one CO and two CN^- ligands (**Figure 1.1**).

Spectroscopic investigations including X-ray crystallographic studies, combined with theoretical calculations have been used to understand the reaction mechanism of the [NiFe] H_2ase, including the redox state and electronic structure of the different states.[7, 9, 25] A redox-active Ni ion exists in several oxidation states (Ni^{2+}, Ni^{3+} and Ni^{+}) during the catalytic cycle, whereas the Fe site retains a low spin, low oxidation state (S = 0, Fe^{2+}). Nowadays, there has been a consensus agreement that three intermediates species are involved during the catalytic cycle. The resting state (**Figure 1.3**) is the diamagnetic Ni–SI_a state ($Ni^{II}Fe^{II}$). Ni-SI_a reacts with one electron and one proton to generate the paramagnetic Ni–L state ($Ni^{I}Fe^{II}$-CysH). Ni–L is proposed to be protonated at the S atom from one cysteine, as confirmed by an observed SH stretching frequency at 2505 cm^{-1}. The proton is then transferred to the metal center to form a bridging hydride species Ni-C state ($Ni^{III}(\mu\text{-H})Fe^{II}$). Ni–C is further reduced and protonated to yield an EPR-silent Ni–R state ($Ni^{II}(\mu\text{-H})Fe^{II}$-CysH). Finally, the Ni–R state releases H_2 and restores the Ni-SI state.

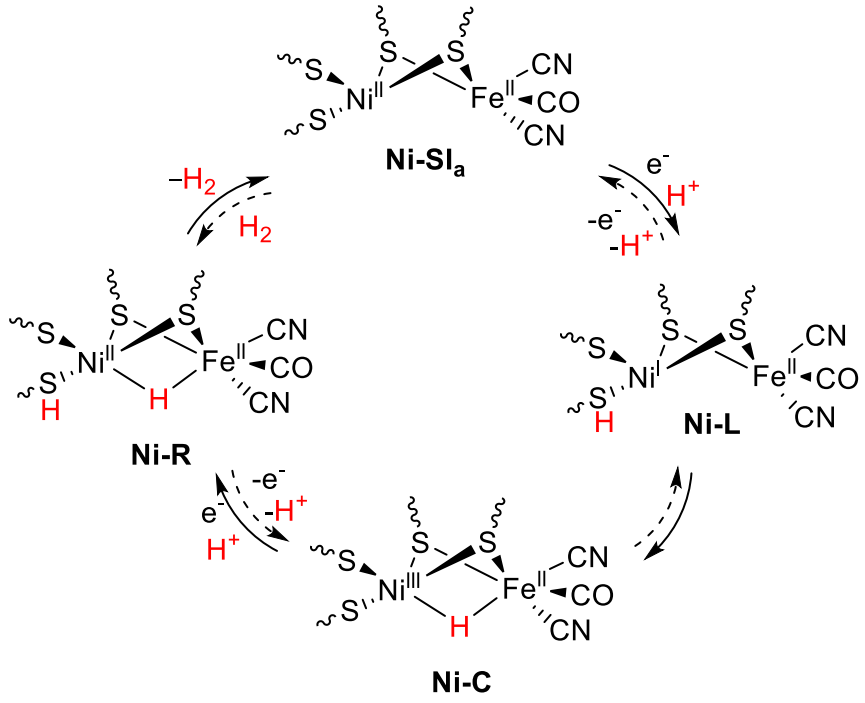

Figure 1.3 Proposed catalytic mechanism of the [NiFe] H_2ase.

In their quest for bio-inspired catalysts with optimal performance, chemists have explored various families of complexes that emphasize several features that seem to be critical, namely the presence of a nearby electron reservoir or potential proton relay, or hydride species with specific structural and electronic properties. The following paragraphs focus on these three aspects in designing series of electrocatalysts to understand and rationalize the impact of these factors. Not only the performance of the different catalysts but also their mechanisms will be discussed to highlight the wide variety of catalytic cycles.

1.1.2 Strategies for optimized electron transfers

As mentioned above, electron transfers are important steps for HER catalytic activity. In this context, two strategies have been developed: (i) the incorporation of ferrocene-derived ligands with one-electron redox properties for their ability to shuttle electrons, and (ii) the use of non-innocent ligands with redox properties.

1.1.2.1 Electron transfer through ferrocene

In nature, an [4Fe–4S] cluster is bound to the [2Fe] moiety by cysteine residue to shuttle the electrons in the [FeFe] H_2ase active site. Inspired by this strategy, several groups have designed complexes where an artificial electron shuttle has been introduced.[26, 27] As an example, the group of Rauchfuss modified the di-iron complex $[FcP^*(CO)_2Fe^{I}(adtBn)Fe^{I}(CO)(dppv)]$ (adt= azadithiolate; Bn= benzyl ; dppv = 1,2-bis(diphenylphosphino)ethene)[28, 29], [1], bearing a ferrocene moiety, $\{Cp^*Fe(C_5Me_4CH_2PEt_2)\}$ (Cp*: pentamethylcyclopentadienyl) abbreviated FcP* **(Figure 1.4**). It can catalyze H_2 production in the presence of $H(OEt_2)_2]BAr^F{}_4$ (10 eq, eq = equivalent) and a reducing agent (Fc*, 5 eq), albeit slow (TON = 3 in 30 min). The proposed mechanism is that [1] is initially protonated at the amine to give $[1H^N]^+$ featuring Fe^{II}, Fe^{I}, and Fe^{I} sites in the presence of $H(OEt_2)_2]BAr^F{}_4$. The $[1H^N]^+$ complex then undergoes the second protonation at iron to generate an ammonium terminal hydride species $[1(t\text{-}H)H^N]^{2+}$(Fe^{II}, Fe^{II}, and Fe^{II} sites). The rapid release of H_2 from $[1(t\text{-}H)H^N]^{2+}$ is triggered by its reduction, accompanied by one electron transfer from PFc^*Et_2 to FeFe core ($[1]^{2+}$ with Fe^{III}, Fe^{II}, and Fe^{I} sites). Otherwise, terminal hydride will fast isomerize to the inactive bridging hydride species. Afterward, $[1]^{2+}$ undergoes reduction to regenerate $[1]^+$ in the presence of a reducing agent (Fc*). The reference complex $(PMe_3)(CO)_2Fe(adtBn)Fe(CO)(dppv)$ does not produce H_2 upon treatment with 5 eq of acid compared to [1] (TON≈4) under similar conditions. This result enhances the function of FcP* as an electron relay. Interestingly, the complex [1] can also catalyze the reversible reaction, i.e. oxidation of H_2. Exposure of [1] to H_2 in the presence of an excess of an oxidizing agent (Fc^+) and a proton acceptor ($P(o\text{-}tolyl)_3$) results in their complete conversion to Fc and $[HP(o\text{-}tolyl)_3]^+$, respectively, but at a slow rate (TOF = 0.4 h^{-1}). This system evidences the interest of functionalizing the second coordination sphere with such an electron transfer cluster in the field of bio-inspired HER catalysts.

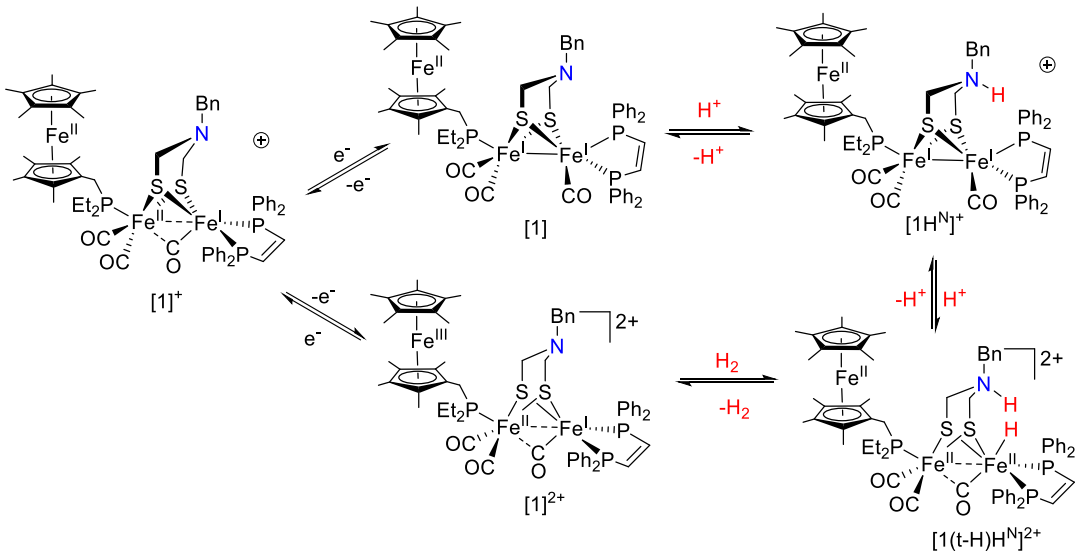

Figure 1.4 Catalytic cycle for chemical hydrogen production and oxidation with complex [1].

1.1.2.2 Non-innocent ligands as potential electron reservoirs

In the above example, the complex catalyzes both the production and oxidation of hydrogen without using the electrocatalytic method but instead in the presence of reducing and oxidizing agents, respectively. However, it remains a rare example among the few catalysts operating under such conditions. Generally, the catalysts are tested for HER activity under electrocatalytic conditions, in which electrons directly transfer to the complex. To assist such electrocatalytic processes, the use of complexes with non-innocent ligands is an attractive strategy since the redox-active ligand can act as an electron reservoir and thus support the whole process.

As reported in the literature, the redox-active bipyridine[30] and phenanthroline[31] have proven to be useful in controlling and modulating the properties of the complexes of the [FeFe] H_2ase models. They have been introduced in the prototype $[(CO)_3Fe^I(pdt)Fe^I(CO)_3]$ [2] complex (pdt = 1,3-propanedithiolate) by replacing two CO ligands. For the bipyridine-based complex $[(CO)_3Fe^I(pdt)Fe^I(^{bpy}N_2)(CO)]$ [3], the strong σ-donating properties of the pyridine units enhance the electron density at the FeFe core leading to the direct protonation of the Fe^IFe^I species in the presence of a strong acid ($HBF_4{\cdot}Et_2O$) in acetonitrile (MeCN) to generate proposed bridging hydride species. In detail, complex [3] shows a two-electron irreversible reduction process at E_{pc} = −2.06 V vs $Fc^{+/0}$ at scan rates lower than 1 V/s in MeCN. However, at scan rates faster than 1 V/s, the reductive peak begins to split into two reductive features, separated by 0.25 V, which have been assigned to the reduction of Fe^IFe^I to Fe^IFe^0 and to the bipyridine moiety bpy^0/bpy^{1-}, respectively. Compared to [2], it leads to a negative shift of the Fe^IFe^I/Fe^IFe^0 reduction potential by 0.4 V, accompanied by an average shift of the ν_{CO} vibration of about 70 cm^{-1} to lower energy. The reduction of H^+ under different acidic conditions can thus occur through different pathways.

In the presence of a strong acid ($HBF_4{\cdot}Et_2O$, pK_a^{MeCN} = 0.1) in MeCN, the catalytic process observed at E_{cat} = −1.33 V vs $Fc^{+/0}$ (E_{cat}: catalytic potential) has been assigned to a [C(ECEC)] (C: chemical process, e.g., a protonation step in the present case and E: electron transfer process) mechanism with $[3(\mu\text{-H})]^+$ being the entry of the catalytic cycle (**Figure 1.5**, pathways A). A milder acid (TsOH, < 4 eq) tends to favor pathway B with a catalytic potential at E_{cat} = −1.70 V vs $Fc^{+/0}$. A [CE(CECE)] or [CE(CEEC)] process is proposed to occur with the reduced hydride species, [3(μ-H)], being the active electrocatalytic species (pathway B, **Figure 1.5**). When excess TsOH (> 4 eq) is present, the acidity of the solution is sufficiently high that pathway A becomes more prominent than pathway B. In the presence of a weak acid (AcOH), the reduction process occurs first instead of a protonation step, followed by protonation to release H_2 to regenerate complex [3] (E_{cat} = −2.06 V vs $Fc^{+/0}$, η = 0.68 V, η: overpotential) with a [EECC] mechanism. Compared to [2] (E_{cat} = −1.83 V vs $Fc^{+/0}$, η = 1.06 V), complex [3] is characterized by a lower overpotential under similar conditions. Indeed, the introduction of a redox-active ligand into the complex facilitates proton reduction catalysis. Besides, this demonstrates that the strength of the acid plays an important role in controlling the mechanism of electrocatalytic proton reduction.

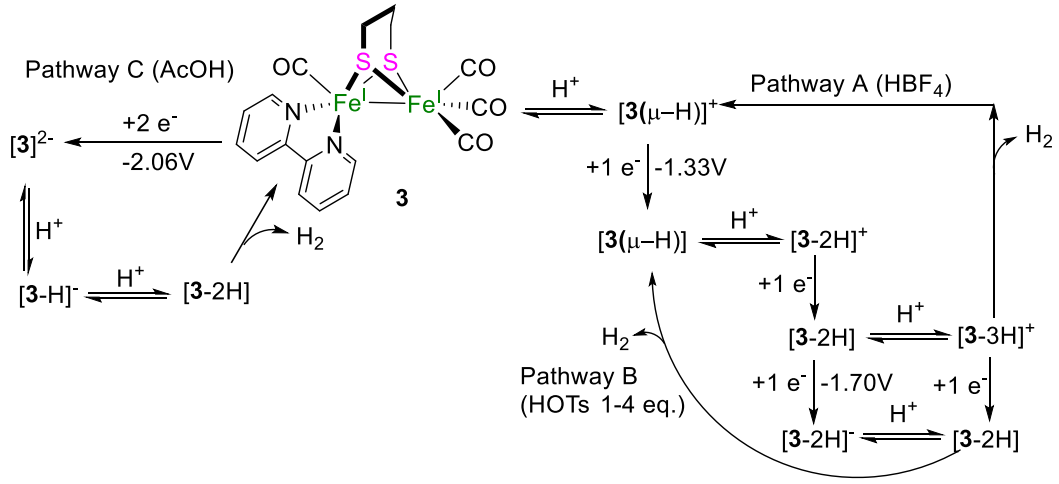

Figure 1.5 Proposed mechanisms for electrocatalytic proton reduction by the complex [3] in presence of different acids.

Bio-inspired FeFe and NiFe complexes have been synthesized with a bipyridine substituted by two alkyl thiolates. The two $[(L^{N2S2})(MeCN)Fe^{II}(CO)Fe^{II}Cp]^+$ $[4]^+$ and $[(L^{N2S2})Fe^{II}(\mu\text{-CO})Fe^{II}Cp(CO)]^+$ $[4(\mu\text{-CO})]^+$ complexes (L^{N2S2} = 2,2'-(2,2'-bipyridine-6,6'-diyl)bis(1,1-diphenylethanethiolate) , Cp = cyclopentadienide) can be obtained quantitatively in solution through the reversible (de)coordination of one CO ligand. The $[4]^+$ complex displays an electrocatalytic activity in the presence of Et_3NHBF_4 (Et_3NH^+, pK_a^{MeCN} = 18.6) in MeCN at $E_{cat/2}$ = −1.90 V vs $Fc^{+/0}$ (overpotential and turnover number: η = 0.73 V, TON=15) (**Figure 1.6**).[32] The NiFe analogue, $[(L^{N2S2})Ni^{II}Fe^{II}Cp(CO)]^+$ $[5]^+$ displays comparable HER activity under similar conditions ($E_{cat/2}$ = −1.85 V vs $Fc^{+/0}$, η = 0.68 V, TON=16).[33]

In both cases, the one electron-reduced species represents the entry of the catalytic

cycle in a proposed [E(ECEC)] mechanism (**Figure 1.6**). For the FeFe complex, the reduction of $\{FeFe'\}_{CO}^{+}$ occurs at E_{pc} = −1.21 V vs $Fc^{+/0}$ and generates a delocalized mixed-valence $Fe^{1.5}Fe^{1.5}$ species with a terminal CO bound to the Fe site bearing the bpy unit, while $[(L^{N2S2})Ni^{II}Fe^{II}Cp(CO)]^{+}$ is reduced ($E_{1/2}$ = −1.29 V vs $Fc^{+/0}$) into a $Ni^{I}Fe^{II}$ species with the CO becoming bridging between the two metallic ions. The $Ni^{I}Fe^{II}$ species displays structural and electronic features similar to those of the Ni-L state (one catalytic state of the [NiFe] H_2ase). The mixed-valence $Fe^{1.5}Fe^{1.5}$ species mimics the H_{ox} state, which is one catalytic state of the [FeFe] H_2ase. The second one-electron reduction process is proposed to mainly occur at the bipyridine moiety of the L^{N2S2} ligand for both the FeFe and NiFe complexes at –1.65 V and –1.90 V vs $Fc^{+/0}$, respectively, leading to a species better described at a $L°M^{I}Fe^{II}$ (M = Fe, Ni) species. The fact that the $Fe^{1.5}Fe^{1.5}$ species is easier to reduce than the $Ni^{I}Fe^{II}$ one is proposed to be due to the stronger back bonding of the terminal CO ligand in the $Fe^{1.5}Fe^{1.5}$ *vs* the bridging CO in the $Ni^{I}Fe^{II}$ one. The fact that the L^{N2S2} ligand is reduced instead of the Fe-Cp site evidences how the bipyridine moiety can act as an electron reservoir, like the proximal [4Fe-4S] cluster in [FeFe] H_2ase. It has also been proposed that the catalytic process is mainly dominated by the redox properties of the bipyridine unit since both complexes display similar HER performances (E_{cat}, η, and TON).

To further clarify the role of bipyridine ligands and the role of the Fe-Cp unit, the complex $[(L^{N2S2})Ni^{II}Fe^{II}Cp^{*}(CO)]^{+}$ $[6]^{+}$ have been synthesized with Cp^{*-} instead of Cp^{-}.[34] Both the redox and structural properties of the complex is modified as a consequence of the steric hindrance of Cp^{*-}. In complex $[6]^{+}$, the Ni···Fe distance of 3.391 Å is significantly longer than in $[5]^{+}$ with a butterfly structure (2.88(4) Å), leading to a quasi-planar $\{NiFeS_2\}$ diamond core. The complex $[6]^{+}$ displays in MeCN two one-electron-reduction processes: (i) one irreversible reduction at E_{pc} = –1.46 vs $Fc^{+/0}$ corresponding to the reaction of Ni^{II} to Ni^{I} resulting in the decomposition of dinuclear NiFe to two mononuclear Fe and Ni complexes; and (ii) a second reversible reduction at $E_{1/2}$ = −1.83 V vs $Fc^{+/0}$ assigned to the bipyridine-centered one-electron-reduction process of the mononuclear $[NiL^{N2S2}]$ complex. The HER activity of $[6]^{+}$ ($E_{cat/2}$ = −1.86 V vs $Fc^{+/0}$, η = 0.690 V, TON=17) is comparable to that of complexes $[4]^{+}$ and $[5]^{+}$ under similar conditions. It has been demonstrated that under catalytic conditions, complex $[6]^{+}$ does not decompose. Its catalytic mechanism has been proposed to follow a [E(CEEC)] cycle. In essence, the non-innocent bipyridine ligand coordinated to the Ni center controls the performance of H_2 production, while the Cp-based ligand coordinated to the Fe ion modulates the redox and structural properties of the dinuclear unit. Interestingly, both complexes $[4]^{+}$ and $[5]^{+}$ display HER activity in acidic aqueous solutions after their physical adsorption onto carbon-based electrodes[35, 36] ($[4]^{+}$: TON = 4.9(0.1)*10^5 in 9 hours, TOF = 15.3(0.3) s^{-1}, at −0.80 V vs SHE, pH 4; $[5]^{+}$: TON = 7.2*10^6 in 10 hours, TOF = 200 s^{-1}, at −0.85 V vs SHE, pH 3).

The complex $[CpNi^{II}(pdt)Fe^{II}(dppe)(CO)]^{+}$ (dppe = 1,2-bis(diphenylphosphino)ethane), $[7]^{+}$,[37] in which the L^{N2S2} ligand is replaced by a diphosphine, displays an

electrocatalytic activity for H_2 production at E_{cat} = −1.16 V vs $Fc^{+/0}$ in the presence of TFA (CF_3CO_2H, pK_a^{MeCN} = 12.7) in CH_2Cl_2. Compared to $[7]^+$, a better HER performance is observed with respect to $[5]^+$, especially with respect to the TOF, 250 s^{-1} *vs* 4 s^{-1} with $[5]^+$ and $[7]^+$, respectively, illustrating further how the presence of a non-innocent redox ligand can lead to optimized efficiency.

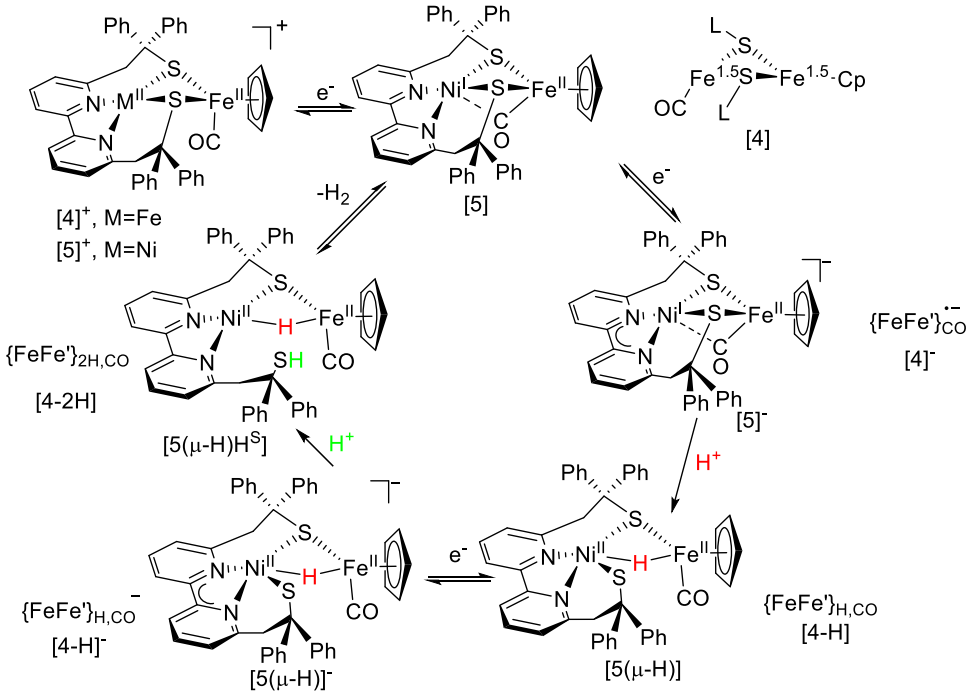

Figure 1.6 Catalytic cycle for H_2 production with the complexes $[4]^+$ and $[5]^+$.

The Reek's group has reported on a synthetic [FeFe] H_2ase mimic containing a redox-active phosphole ligand with conjugated N-heterocycles.[38] This phosphole-based ligand acts as an electron reservoir, which is synergistically activated through protonation processes. The $[(CO)_2L^{PNP}Fe(bdt)Fe(CO)_3]$ ([8], bdt = benzene-1,2-dithiolato) complex displays HER activity at E_{cat} = −2.0 V vs $Fc^{+/0}$ in the presence of Et_3NH^+ in CH_2Cl_2 solution. The complex requires an activation step through a double protonation and a two-electron reduction process (ECCE process, E_{pc} = −1.44 V and −1.18 vs $Fc^{+/0}$) to generate the $[8(\mu\text{-}H)H^N]$ species, which corresponds to the entry of the catalytic cycle (**Figure 1.7**). This mixed-valence $Fe^{II}Fe^{I}$ complex $[8(\mu\text{-}H)H^N]$ bears a bridging hydride, and the initial phosphole-based ligand is reduced by two electrons and protonated on the generated secondary amine. This $[8(\mu\text{-}H)H^N]$ species thus undergoes a two-electron reduction and a protonation (ECE process, E_{pc} = −2.0 V and −1.9 V vs $Fc^{+/0}$) leading to the key intermediate, $[8(\mu\text{-}H)(H^N)_2]^-$, which can release H_2 upon the last protonation with a rate-determining constant of k_{cat} = 10^5 M^{-1} s^{-1}. Interestingly, during the catalytic cycle, an electron is transferred from the phosphole ligand to the iron center, which contributes to the leveling of redox potentials within the catalytic cycle. This is similar to the enzyme's catalytic cycle where the reduced state H_{red} is protonated with concomitant electron transfer from the [4Fe-4S] cluster to diiron site.[13, 39] In analogy,

we can mention here that the H-cluster in the [FeFe] H_2ase, can be protonated at the [4Fe-4S] cluster under specific alkaline and reducing conditions.[40] Overall, the bipyridine unit allows this ligand to store electrons assisted by protonation steps enhancing PCET processes. It has been emphasized that its performance arises from the redox-active ligand.

Moreover, this electrocatalyst is not only water-soluble but also air-tolerant. The catalytic activity in air-saturated solution retains 60% of the catalytic performance (in terms of current density) compared to experiments performed in degassed solvents under N_2. It can produce H_2 in the presence of H_2SO_4 in an aqueous solution at E_{cat} = −0.66 V vs NHE at TOF = 70 000 s^{-1} (k_{cat} = 3.5 × 10^4 M^{-1} s^{-1} under an acid-independent regime).

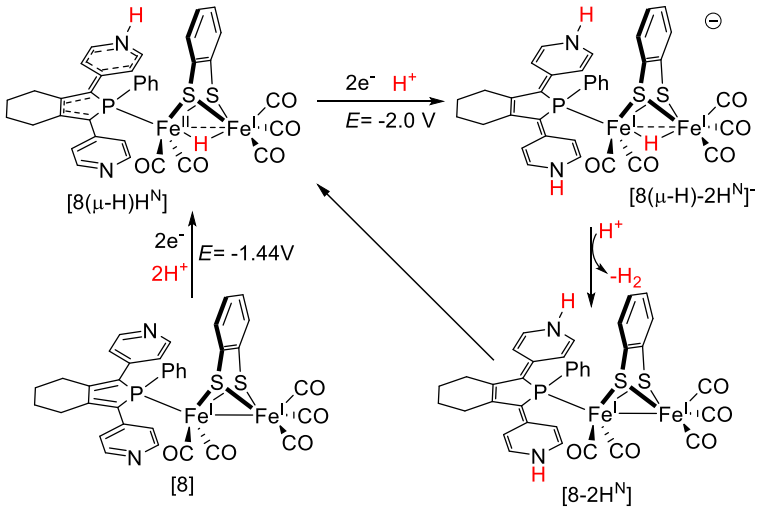

Figure 1.7 Catalytic cycle for H_2 production with the complex [8].

1.1.3 Strategies for optimized proton transfers

1.1.3.1 Pendant amines as proton relays

As mentioned in section 1.1.1.1, the pendant amine as a proton relay is considered critical for the exceptional rate of the catalytic activity in the [FeFe] H_2ase and its model complexes. This point is demonstrated when hybrids of [FeFe] H_2ase have been designed by introducing different bridges, $[Fe_2[(SCH_2)_2X](CN)_2(CO)_4]$ with X = O (odt), CH_2 (pdt) or NH (adt). While no H_2 production is observed in the case of X = O and CH_2, efficient HER is measured with X = NH in the presence of methyl viologen and sodium dithionite.[41] Inspired by this observation, series of structural and functional models of the [FeFe] and [NiFe] H_2ases with pendant amine have been developed.[7]

As a prototype, the $[(CO)_3Fe(adt)Fe(CO)_3]$[42] (adt = $-SCH_2NHCH_2S-$) complex, [9], with its pendant amine, displays efficient electrocatalytic activity for H_2 production in

MeCN. Depending on the acidity of the proton source, a [ECEC] or [CECE] catalytic mechanism has been proposed (**Figure 1.8**). The complex [9] displays a reversible two-electron reduction wave at $E_{1/2}$ = −1.58 V (vs $Fc^{+/0}$) under CO atmosphere in the absence of acid. After the addition of 1 eq of $ClCH_2CO_2H$ (pK_a^{MeCN} = 15.3), the redox system becomes irreversible and a second irreversible process appears at E_{pc} = −1.75 V vs $Fc^{+/0}$. $ClCH_2CO_2H$ is not acidic enough to protonate complex [9] (DFT-predicted pK_a of the protonated form, $[9\text{-}H^N]^+$, of 8.2). After the one-electron reduction of complex [9], the basicity of both the amine group and the Fe is enhanced (DFT-predicted $pK_{a(Fe\ site)} > pK_{a(adt\text{-}N\ site)}$). The reduced form $[9]^-$ can thus be protonated by $ClCH_2CO_2H$ to generate an intermediate bearing a terminal hydride on one Fe site ([9(μ-H)], DFT-predicted $pK_{a(Fe\ site)}$ = 17.1). Afterward, [9(μ-H)] is reduced to generate $[9(\mu\text{-}H)]^-$ at E_{pc} = −1.75 V. The hydride $[9(\mu\text{-}H)]^-$ is further protonated at the amine group to yield $[9(\mu\text{-}H)H^N]$ (DFT- predicted $pKa_{adt\text{-}N}$ =15.3). Finally, H_2 is released concomitantly with the regeneration of the complex [9]. The overpotential (η) is calculated to be 0.64 V (E_{cat} = −1.60 V vs $Fc^{+/0}$) under these conditions.

When a stronger acid acts as a proton source (HOTs = $p\text{-}CH_3C_6H_4SO_3H$, pK_a^{MeCN} = 8.6), the CV of [9] also displays two irreversible reduction processes at −1.27 V and −1.58 V vs $Fc^{+/0}$, respectively. Since the DFT-predicted pK_a of $[9\text{-}H^N]^+$ is 8.2, the protonation of the amine occurs prior to the one-electron reduction under these strong acid conditions to generate $[9\text{-}H^N]^+$. The reduction process occurring at E_{pc} = −1.27 V is assigned to the reduction of $[9\text{-}H^N]^+$ to produce the $[9\text{-}H^N]$ species. The resulting reduced species $[9\text{-}H^N]$ undergoes a tautomerization process: the proton is transferred to one iron center to generate a terminal hydride species [9(t-H)]. This can be rationalized by the fact that the hydride in [9(t-H)] is more basic than the amine in $[9\text{-}H^N]$ (DFT-predicted $pK_{a(Fe\ site)}$ = 13.8). However, this tautomerization process could not be evidenced experimentally,[43] and the catalytic activity of [9] in the presence of a weak acid has been rationalized by the reduction of the catalyst at a much less negative potential. Based on the DFT-calculated mechanism (**Figure 1.8**), [9(t-H)] is then protonated at the amine site, leading to formation of $[9(t\text{-}H)H^N]^+$ (DFT-calculated $pK_{a(adt\text{-}N)}$ = 9.5). It releases H_2 after its one-electron reduction. The overpotential of the electrocatalytic reaction in the presence of HOTs is 0.86 V (E_{cat} = −1.27 V vs $Fc^{+/0}$). Thus complex [9] is readily protonated at the amine group rather than reduced under strong acid conditions (pK_a<11), while when a relatively weak acid (pKa>11) is used, it first undergoes a reduction that enhances the basicity of the iron site to promote its protonation. Therefore, the acidity of the proton source is of crucial importance, and different acidities lead to different catalytic mechanisms during the catalysis process.

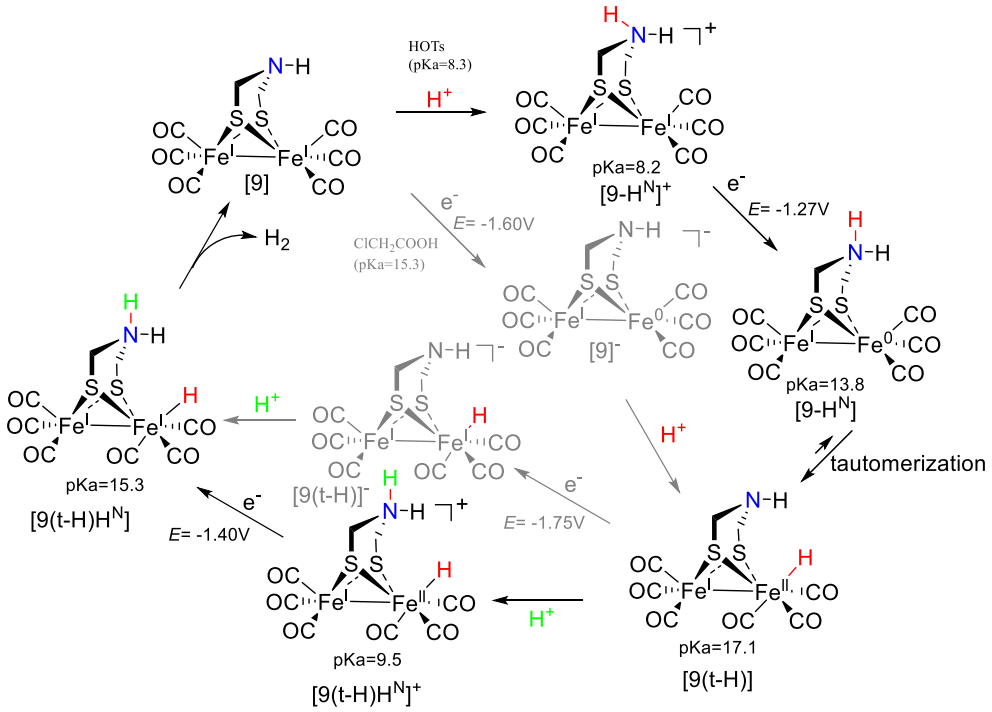

Figure 1.8 Catalytic cycles for H_2 production with complex [9] in the presence of either $ClCH_2CO_2H$ (black) or HOTs (gray).

Complex [9] displays a lower overpotential compared to a similar complex $[(CO)_3Fe(pdt)Fe(CO)_3]$ ([2], η=1.06 V), which does not contain a potential proton relay under similar acid conditions. This well illustrates the notable impact of the presence of the pendant amine on the activity of the electrocatalyst. Numerous other analogous FeFe complexes with a pendant amine have been also synthesized, and they all display HER activity with a lower overpotential compared to their parent compounds without proton relay. As a few other examples (**Figure 1.9**), complex [10],[44, 45] in which two CO on one Fe site have been substituted by a P-N-P ligand, displays HER activity in the presence of HOAc (acetic acid, pK_a^{MeCN} = 22.3) with an overpotential of 0.67 V, a value that is much smaller than that measured with the parent complex [2] without pendant amine (η=1.06 V). However, only a slightly lower overpotential (η=0.60 V) has been measured under similar conditions with complex [11], which contains an additional pendant amine at the bridge. The complex [12] with a bridging nitrogen heterocyclic-based ligand (pyrazine) also shows a lower overpotential (η=0.58 V, in the presence of HOAc) compared with the $[(CO)_3Fe(SPhS)Fe(CO)_3]$ complex (η=0.63 V, in the presence of HOTs) that bears a phenyl group instead of the pyrazine.[46] These examples highlight the effect of the addition of a pendant amine well positioned in the second coordination sphere of the FeFe unit. Not only protonation of the pendant amine lowers the overpotential of the reaction, but the formation and release of H_2 is promoted because of the proximity between the ammonium proton and the Fe-H hydride in the last intermediates species of the catalytic cycle.[47]

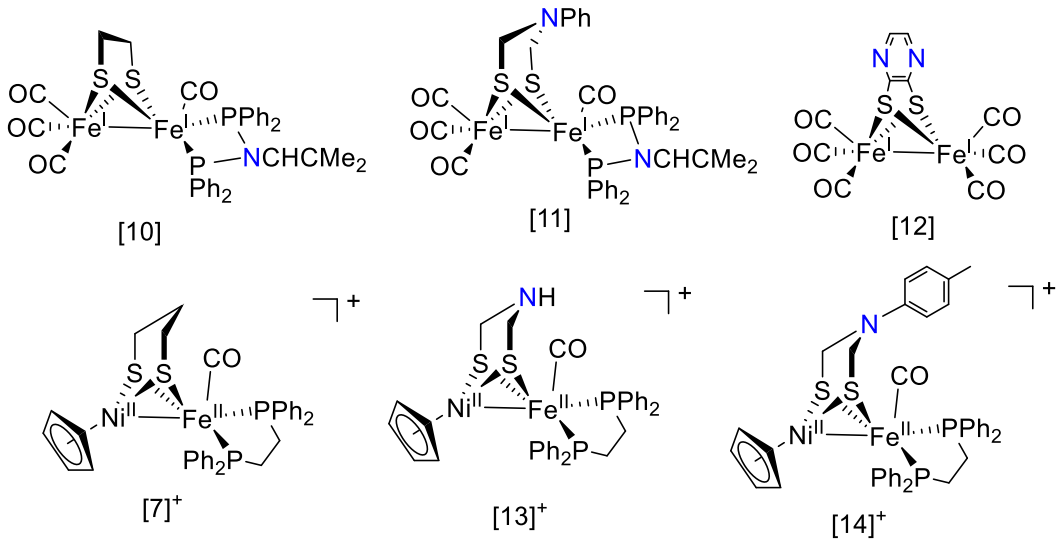

Figure 1.9 Different bio-inspired FeFe or NiFe complexes with or without the presence of a potential proton relay.

More recently, the first series of azadithiolato-bridged NiFe complexes bearing a pendant amine has been synthesized and tested for their ability as HER electrocatalysts.[48] The overpotential of the $[CpNi^{II}(adt)Fe^{II}(CO)(dppe)]^+$complex, $[13]^+$ (**Figure 1.9**), has been measured to be 0.54 V (E_{cat} = −1.43 V vs $Fc^{+/0}$) in the presence of TFA in MeCN. The authors have compared the ratio between the catalytic current (i_{cat}) and the reductive peak current (i_p) to probe the kinetics of the reaction (higher i_{cat}/i_p values indicate faster catalysis). In the presence of TFA, the value of i_{cat}/i_p is calculated to be 5.3, while the parent complex $[CpNi^{II}(pdt)Fe^{II}(CO)(dppe)]^+$, $[7]^+$,[37] without the pendant amine leads to a lower value (i_{cat}/i_p = 2, E_{cat} = −1.16 V vs $Fc^{+/0}$) under similar conditions. This investigation demonstrates that the presence of a potential proton relay in bio-inspired NiFe complexes is also beneficial for enhanced HER performances. The nature of the R substituents of the azadithiolate bridging ligand also affects the overpotential. Indeed, the complex $[CpNi^{II}(SCH_2NRCH_2S)Fe^{II}(CO)(dppe)]^+$ (R= 4-MeC_6H_4) $[14]^+$ displays HER activity with an overpotential of 0.78 V, a higher value than that for the analogue complex $[13]^+$ (η= 0.54 V) with R = H.[48]

1.1.3.2 Pendant phosphine oxides (P=O group) as proton relays

As early as about 10 years ago, the Weigand's group reported a novel type of bio-inspired FeFe complexes [15] bearing the μ-$(SCH_2)_2$(Ph)P=O ligand (**Figure 1.10**).[49] In the presence of $HBF_4{\cdot}Et_2O$, a shift of the CO vibrations to higher energy by ∼10 cm^{-1} is observed in the IR spectrum of the CH_2Cl_2 solution of the complex [15]. The $^{31}P\{^1H\}$ NMR spectrum of complex [15] in the presence of $HBF_4{\cdot}Et_2O$ displays a downfield shift by 36.6 ppm. These data evidence that protonation occurs at the P=O site in the presence of the very strong acid, $HBF_4{\cdot}Et_2O$. However, [15] is not

protonated with the moderate acid [HPy][BF_4] (p$K_{a\ [HPy][BF_4]}$ > p$K_{a\ HBF_4\cdot Et_2O}$). More recently, using the μ-$(SCH_2)_2$(Et)P=O ligand, the corresponding complex ([$(CO)_3$Fe(μ-$(SCH_2)_2$(Et)P=O)Fe$(CO)_3$], [16])[50] can be protonated with the mild acid TFA. Interestingly, the overpotential of 0.38 V (E_{cat} = −1.27 V vs $Fc^{+/0}$) for complex [16] is significantly lower than for [2] (η=1.06 V) under similar conditions. Based on DFT calculations and digital simulations, a three-electron and three-proton process has been proposed. The key step corresponds to the proton transfer from the P=O-H function to the Fe sites to form a bridging hydride after double reduction of the protonated initial complex. Both the experimental observations and the mechanistic investigation evidence that the R-P=O bridgehead can act as a proton relay as an effective alternative for a pendant amine.

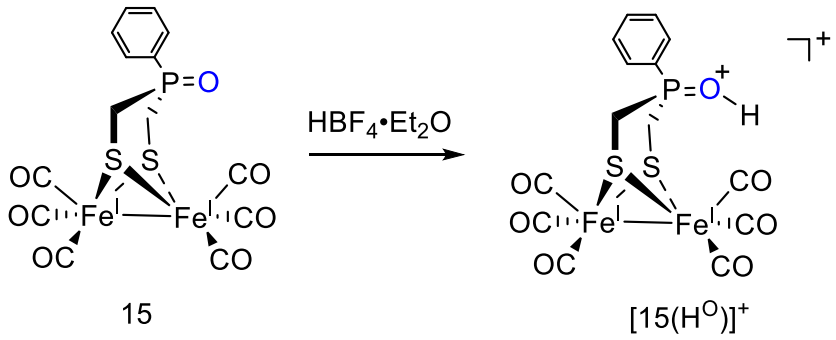

Figure 1.10 Protonation step of complex [15].

1.1.3.3 Role of metal-bound thiolates

As described in sections 1.1.3.1 and 1.1.3.2, the reported works demonstrated that the bridging ligands in bio-inspired dinuclear NiFe or FeFe complexes bearing a –NR or R–P=O function can act as proton relays to promote the electrocatalytic activity for H_2 production during the catalytic process. In these dinuclear complexes, the two metals are connected by a dithiolate bridge, also prone to protonation.

Take the simplest bio-inspired complex of the [FeFe] H_2ase as an example ([$(CO)_3Fe^{I}$(pdt)$Fe^{I}(CO)_3$], [2]),[51, 52] different possible catalytic cycles have been proposed based on experiments and DFT calculations. The initial complex [2] is first reduced ($E_{1/2}$ = −1.59 V vs $Fc^{+/0}$) and then protonated leading to a bridging hydride species in the presence of the HOTs acid in MeCN. After the second reduction and its further protonation, two hydride species are produced: (i) a dihydride species with two terminal hydrides coordinated to each of both Fe sites and (ii) a dinuclear Fe species with a bridging hydride and a protonated thiolate (**Figure 1.11**). In case (ii), the corresponding thiol remains coordinated to only one Fe site, resulting in a structural isomerization with the CO becoming bridging. The two hydride species are further reduced, then releases H_2 and restores the reduced state [$(CO)_3Fe^{I}$(pdt)$Fe^{0}(CO)_3]^-$ (E_{cat} = −1.84 V vs $Fc^{+/0}$). Therefore, the dithiolate ligand not

only acts as a bridging ligand to generate stable dinuclear complexes and to tune their redox potential but also serves as a proton relay during the catalytic cycle thanks to its hemilabile character when protonated.

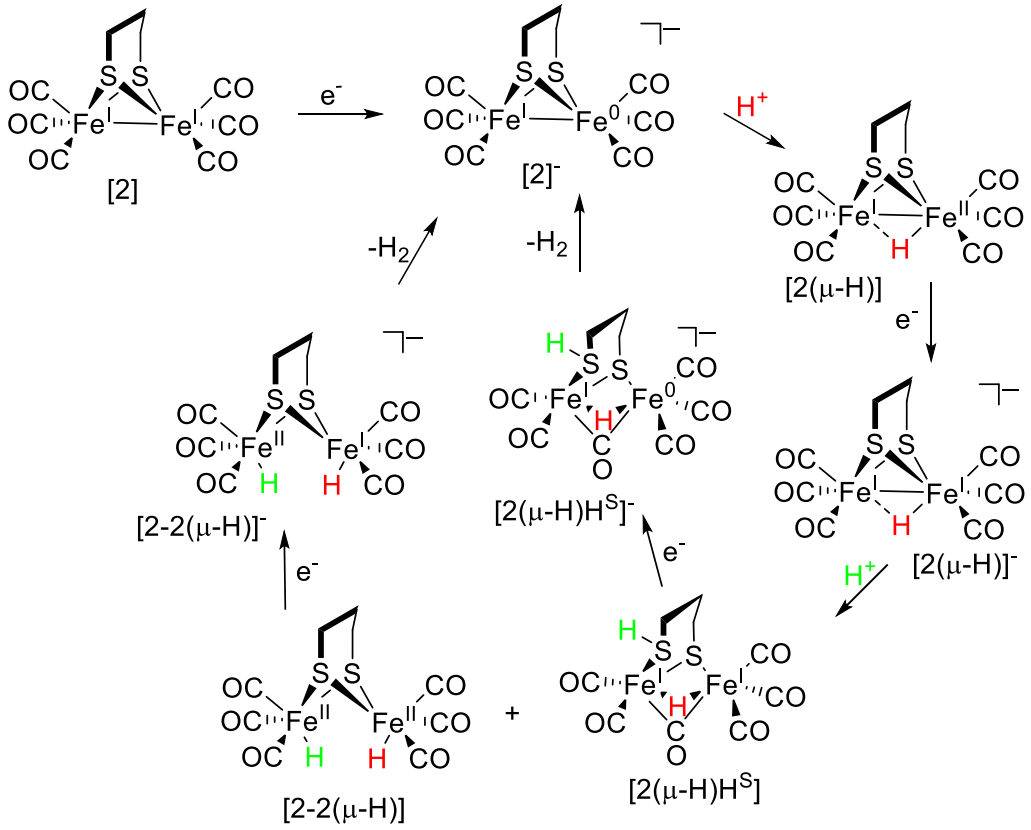

Figure 1.11 Different proposed catalytic cycles for H_2 production with complex [2].

The $[(^{alkyl}N_2S_2)Fe(NO)Fe'Cp(CO)]^+$ complex ($^{alkyl}N_2S_2$ = bismercaptoethane diazacycloheptane),[53] $[17]^+$, displays similar hemilability properties and a proposed mechanism has been predicted based on DFT calculations. The crucial step of the catalytic cycle has been identified as the decoordination of the thiol from the Fe' site to generate reactive sites on both the thiolate and the Fe' site to allow the formation of an intermediate species with a protonated thiolate and a terminal hydride during the catalytic process (**Figure 12**). After the first reduction, a protonation leads to a thiol species $[17\text{-}H^S]^+$. Its further reduced species reacts with another proton to produce a terminal hydride species $[17(t\text{-}H)H^S]^+$. The close proximity of the hydride and the thiol proton allows H^+/H^- heterocoupling to produce H_2. The catalytic potential has been determined at E_{cat} = −1.56 V vs $Fc^{+/0}$ in the presence of TFA in MeCN (TON = 0.33(±0.02) in 30 min, faradic yield = 77.2(±7.9) %). Moreover, its overpotential (η = 0.938 V) is slightly lower than that of the complex [2] complex (η=1.06 V).

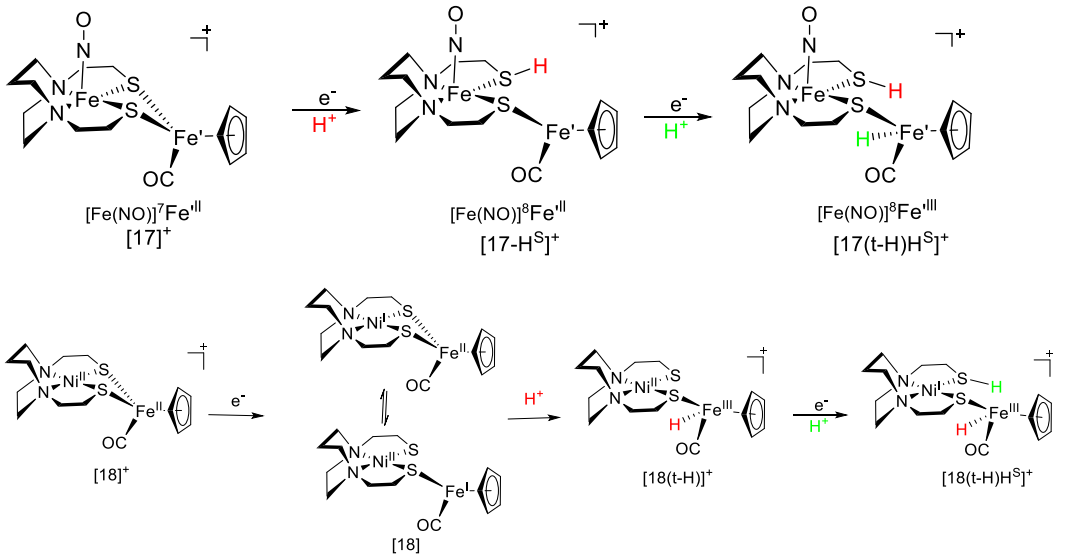

Figure 1.12 Formation of key protonated species within the catalytic cycle with complexes $[17]^+$ (top) and $[18]^+$ (bottom).

An analogous complex $[(^{alkyl}N_2S_2)Ni^{II}Fe^{II}Cp(CO)]^+$, $[18]^+$, has been described with Ni instead of the $\{Fe(NO)\}^7$ center and a DFT-predicted mechanism has been proposed (**Figure 1.12**, bottom). Complex $[18]^+$ is reduced by one electron to produce the [18] species. During the reduction of $[18]^+$, one thiolate becomes monodentate leading to an electron transfer from Ni^I to Fe^{II} to generate a $Ni^{II}Fe^I$ species. The resulting Fe^I site has then enough electron density to accept a proton. The [18] is thus protonated to form a terminal Fe^{III}-hydride species $[18(t\text{-}H)]^+$ at the Fe site in the presence of TFA. The further protonation of its reduced form occurs at the terminal thiolate. Finally, the close proximity of the hydride and the thiol proton allows H^+/H^- heterocoupling to release H_2 as in $[17]^+$. The complex $[18]^+$ is active as a HER electrocatalyst with a faradaic yield of 96(±2.9)% (E_{cat} = −1.56 V vs $Fc^{+/0}$, TON = 0.26(±0.01) in 30 min). Its overpotential (η = 0.942 V) is only slightly higher than that of $[17]^+$ (η=0.938 V).

Compared with the complex $[5]^+$ (η = 0.68 V), which possesses a redox-active ligand, complex $[18]^+$ displays a much higher overpotential under similar conditions. This result underscores once more the important role of the innocent redox-active bipyridine ligand in the activity of H_2 production. Based on DFT calculations, it has been proposed that the bridging dithiolate of the L^{N2S2} ligand in complex $[5]^+$ (described in **section 1.1.2.2**, **Figure 1.6**) also displays hemilability properties and can act as a proton relay to accept H^+ during the HER catalytic process.[54] It can be seen that these complexes containing hemilabile bridging thiolates are also valuable catalysts for electrocatalytic H_2 production.

The protonation of thiolate has also been experimentally evidenced. The heterodinuclear $[(S_4)Ni(\mu\text{-}CO)Fe(CO)_2]$ (S_4H_2 = 1,2-bis(4-mercapto-3,3-dimethyl-2-thiabutyl)benzene) complex, [19],[55] can be protonated in the presence of $HBF_4{\cdot}Et_2O$ **(Figure 1.13)**. The signal of the –SH function has been identified at 4.79 ppm in the ^1H NMR spectrum of the protonated species.

A –SH vibration is also observed at 2512 cm^{-1} in the IR spectrum. Thus, the proposed protonation site is at the terminal thiolate bound to the nickel site leading to $[19\text{-}H^S]^+$. Both [19] and $[19\text{-}H^S]^+$ display comparable HER electrocatalytic activity in the presence of CF_3CO_2H in MeCN (E_{cat} = −1.60 V vs $Fc^{+/0}$). The overpotential (and observed TOF) values for [19] and $[19\text{-}H^S]^+$ are 0.54 V (5 h^{-1}) and 0.57 V (8 h^{-1}), respectively. Since [19] is not protonated by CF_3CO_2H, $[19\text{-}H^S]^+$ is not implicated in the catalytic cycle of [19] as an intermediate species. Interestingly, DFT calculations predicted a bridging hydride $Ni^{II}Fe^{II}$ species, $[19(\mu\text{-}H)]^+$ as a tautomeric form of $[19\text{-}H^S]^+$, which structure is energetically higher (~5 kcal mol^{-1}) than the most stable $[19\text{-}H^S]^+$ isomer. This observation implies that an Fe(μ-H)Ni intermediate species should be accessible during the electrocatalytic cycle. This example demonstrates that metal-bound thiolate can act as a proton shuttle to assist the transfer of protons during the HER catalytic process. An analogy can be made with the [NiFe] H_2ase, for which it has been experimentally demonstrated that a Ni-bound cysteine can be protonated after photolysis of the bridging hydride ligand in the Ni^IFe^{II} state.[17, 56, 57]

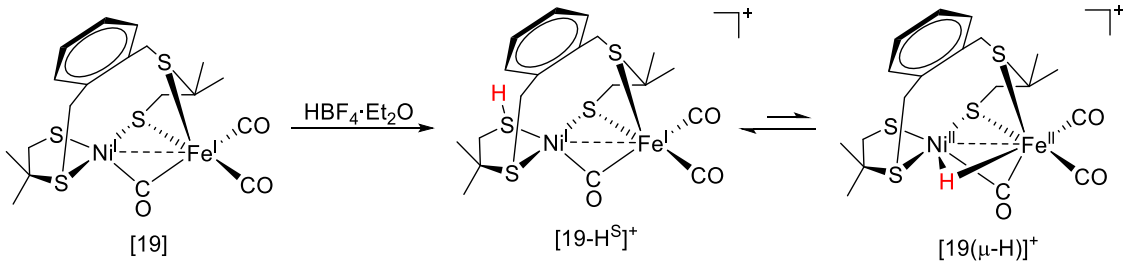

Figure 1.13 Equilibrium between the two $[19\text{-}H^S]^+$ and $[19(\mu\text{-}H)]^+$ tautomers.

In these sections, we have discussed three strategies to synthesize bio-inspired HER catalysts with potential proton relay: (i) pendant amines; (ii) –P=O group; (iii) hemilabile thiolate. Based on DFT calculations, they can act as proton acceptors to assist the transfer of protons to the metal site under certain acidic conditions during the catalysis process. Besides, depending on the acid used, and thus its pK_a, it is possible to control the E and C steps sequence allowing the fine-tuning of the catalytic mechanism. Therefore, the study of this impact can contribute to a better understanding of the catalytic mechanism, especially regarding the properties of the involved intermediates species, and thus indirectly to the design of catalysts with optimal activities.

1.1.4 Nature of the hydride intermediate and reactivity

As discussed above, in the case of the [FeFe] and [NiFe] H_2ases or their bio-inspired complexes, hydrides represent key intermediates during the catalytic cycle and are the outcomes of the protonation or the H_2 activation of the metal site. [58, 59] Two different hydride binding modes have been observed, i.e., terminal or bridging. In general, the bridging hydrides are more thermodynamically favored than the terminal hydrides. Bridging hydrides can thus be generated by (spontaneous) isomerization of a terminal hydride precursor, but they often lead to electrocatalysts

with low HER performance.[60-63] In contrast, terminal hydrides are usually directly formed through protonation of the FeFe or NiFe complexes.[63]

1.1.4.1 Hydride in bio-inspired FeFe complexes

In generally, hydride is found in bridging mode because of its thermodynamically favorable in room temperature. For example, $[2(\mu\text{-H})]^+$ is generated from the reaction between $[(CO)_3Fe^I(pdt)Fe^I(CO)_3]$ [2] and $[SiEt_3]B(C_6F_5)_4$ and HCl (**Figure 1.14**).[64] $[2(\mu\text{-H})]^+$ has been characterized by ^{1}H NMR with a sharp singlet at −15.9 ppm and the X-ray data revealed an Fe···Fe distance of 2.5540(4) Å, slightly elongated with respect to the initial complex [2] (2.5103(11) Å). The electrocatalytic properties of [2] have been investigated in the presence of HOTs (see **section 1.1.3.3.**). The complex [2] is insufficiently basic to be protonated by HOTs and needs to be reduced (E_{pc} = −1.59 V vs $Fc^{+/0}$) before undergoing a protonation leading to the proposed [2(μ-H)] complex, which is then readily reduced (E_{pc} = −1.48 V vs $Fc^{+/0}$) into another bridging hydride $[2(\mu\text{-H})]^-$ (**Figure 1.11**).[51, 52]

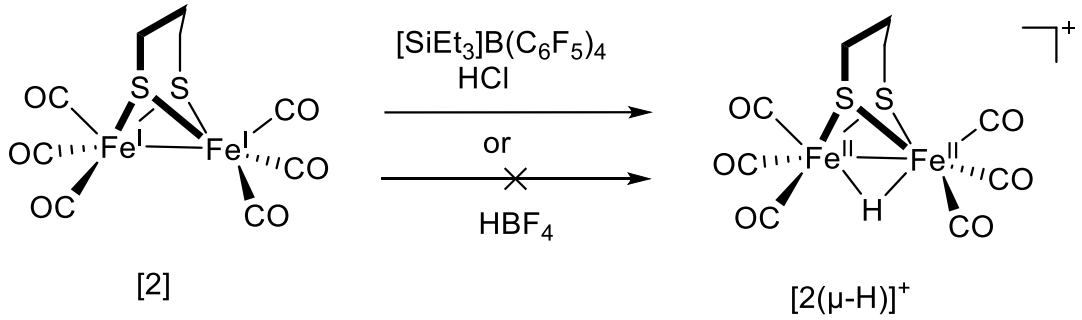

Figure 1.14 Protonation of the complex [2].

In addition, the $[(CO)_3Fe^I(pdt)Fe^I(CO)dppe]$ complex, [20], is formed, by replacing two CO ligands with a σ-donating diphosphine ligand (dppe) in the complex [2]. At −203 K, complex [20] reacts with HBF_4•Et_2O to generate a terminal hydride (^{1}H NMR δ = −4.33 ppm), which isomerizes to a more thermodynamically favorable bridging hydride (^{1}H NMR δ = −14.1 ppm) upon warming to 298 K (**Figure 1.15**). X-ray data confirm that the bridging hydride species displays a longer Fe···Fe distance (2.581(5) Å and Fe-H: 1.627(3), 1.640(4) Å) compared to its initial unprotonated form (2.547(7) Å). However, no reaction is observed between complex [2] and HBF_4•Et_2O, due to the low basicity of [2] (**Figure 1.14**).

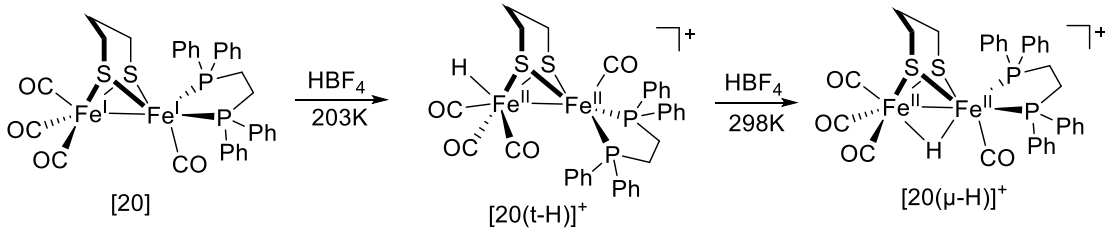

Figure 1.15 Protonation of the complex [20].

The above examples illustrate that the formation of hydrides is related to the basicity

of the iron-iron core and the strength of the exogenous acid, and that the thermal stability of bridging hydride is higher than that of terminal mode. In contrast, terminal hydride facilitates H_2 production by lowering the reduction potential (~200 mV) of the complex with respect to intermediates with bridging hydride[65] thanks to their higher hydridic character[66, 67] and by a closer proximity to an internal proton (in the complexes bearing a proton relay).[68] It is noted that the main contribution to the kinetically favored formation of terminal hydride arises from the azadithiolate moiety, which plays a crucial role in the catalytic activity of both models and enzymes (see **session 1.1.3.1**).[7] In addition, it is proposed that protonated amine groups can transfer protons to the metal center to provide a terminal hydride by DFT calculations, as in [FeFe] H_2ase during the catalytic cycle.

For example, the $[(CO)(dppv)Fe(adt)Fe(dppv)(CO)]$[47] [21] is protonated by $[H(OEt_2)_2]BArF_4$ in CH_2Cl_2 to offer terminal hydride species (^{1}H NMR δ = −4.2 ppm) at −80°C. Above −20°C, the broaden signal in the ^{1}H and ^{31}P NMR spectrum is defined as the exchange between the hydride and ammonium tautomer. The terminal hydride species isomerizes to a bridging hydride species (^{1}H NMR δ = −13.7 and −14.8) at room temperature. The terminal hydride species is readily protonated to produce the ammonium hydride species. The crystal structure of the ammonium hydride species shows that the ammonium center of the dithiolate cofactor $adtH^+$ is adjacent to the Fe-H center (Fe-H: 1.44(4) Å; NH···HFe: 1.88(7) Å), providing unique insights into the proposed enzymatic intermediate $H_{ox}(H^+,H^-)$. The ammonium hydride $[21(t\text{-}H)H^N]$ is a faster electrocatalyst for H_2 production in the presence of CF_3COOH (E_{cat} = −1.11 V vs $Fc^{+/0}$, TOF = 58 000 s^{-1}, η = 0.51 V). The analogue complex $[(t\text{-}H)(CO)(dppv)Fe(pdt)Fe(dppv)(CO)]$ provides a very low catalytic efficiency with $HBF_4{\cdot}Et_2O$ (E_{cat} = −1.49 V vs $Fc^{+/0}$, TOF = 5 s^{-1}, η > 1 V) under similar conditions, compared to the ammonium hydride species. The proposed [CCEE] or [CECE] pathway described in the presence of different acids (**Figure 1.16**), indicates that the combination of a terminal hydride with the azadithiolate cofactor greatly facilitates the reduction of protons to generate H_2.

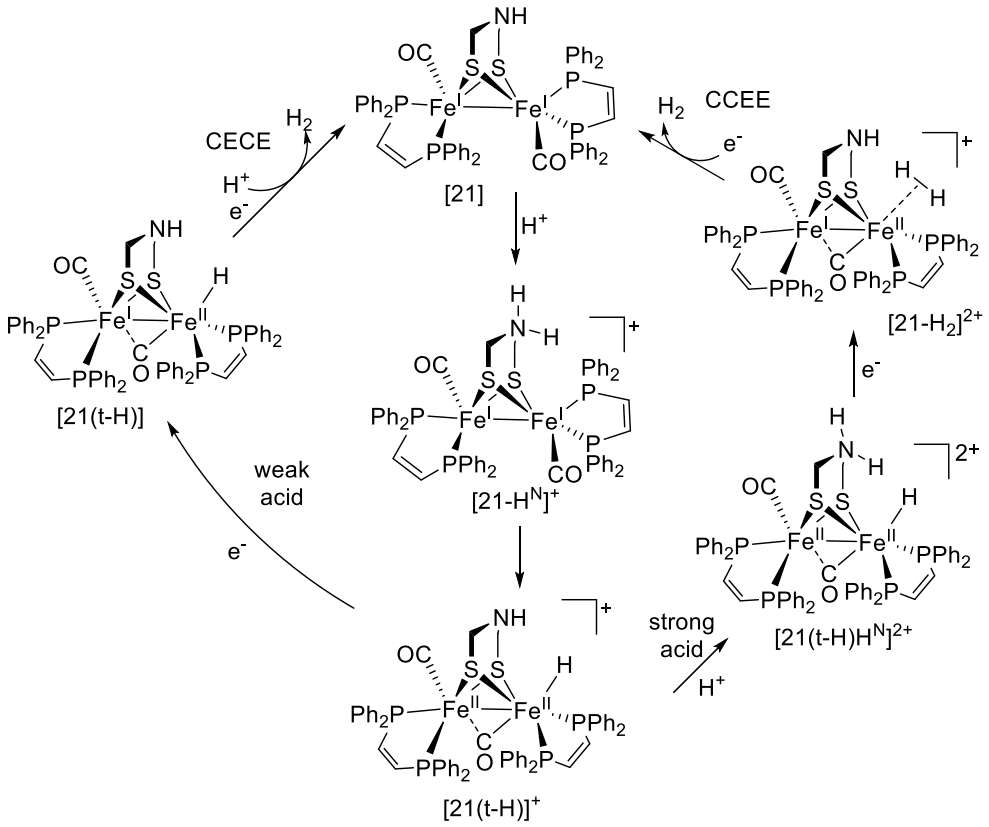

Figure 1.16 Catalytic cycles for H_2 production with [21].

In nature, the terminal hydride observed in the [FeFe] H_2ase is further stabilized by the amino residues present in the active site, allowing its stabilization even at room temperature. Interestingly, even when the N-H group of adt is substituted by an O atom in [FeFe] H_2ase hybrids, which eliminates the direct proton relay, the corresponding terminal hydride species is more stable than the complex with the bridging adt. However, all these modified thiolate scaffolds (odt, pdt), show inferior reactivity in reducing H_2 to the original adt present in the enzyme.[21, 41]

Based on DFT calculations, it has been proposed that a di-terminal hydride can be involved as a catalytic intermediate. One example of such a species has been generated by protonating the hydride $[(CO)_3Fe^{I}(pdt)(\mu\text{-}H)Fe^{I}(CO)_3]^-$ complex ($[2(\mu\text{-}H)]^-$, see **Figure 1.11**). One of these hydride species is formed with two terminal hydrides coordinated to each of both Fe ion. It is noted that a similar species with two terminal hydrides has been proposed from the H_2 activation of the dinuclear Ni(μ-H)Ru complex, $[22(\mu\text{-}H)]^+$ (**Figure 1.17**).[7, 69]

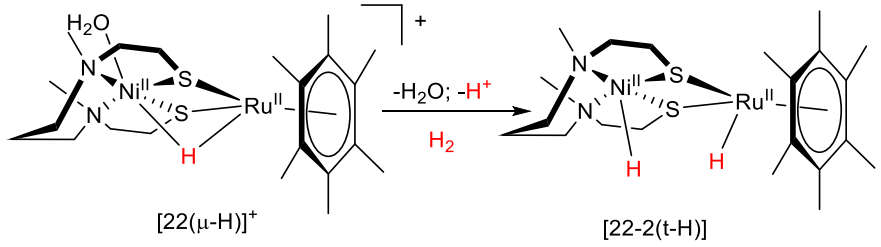

Figure 1.17 Formation of dihydride species [22-2(t-H)].

The transient formation of a terminal hydride species is also proposed to explain how the bridging hydride species, $[(Me_3P)(CO)_2Fe(pdt)(\mu\text{-}H)Fe(CO)_2(PMe_3)]^+$ ($[23(\mu\text{-}H)]^+$), can mediate H/D scrambling under D_2 and ambient light (**Figure 1.18**).[61] The process is rather slow since the hydride exchange requires several weeks in CH_2Cl_2. Besides, it has been observed that no H/D exchange can take place when a coordinating solvent such as MeCN is used, supporting the requirement of an open coordination site created through an isomerization process between a bridging hydride and a terminal one.[70]

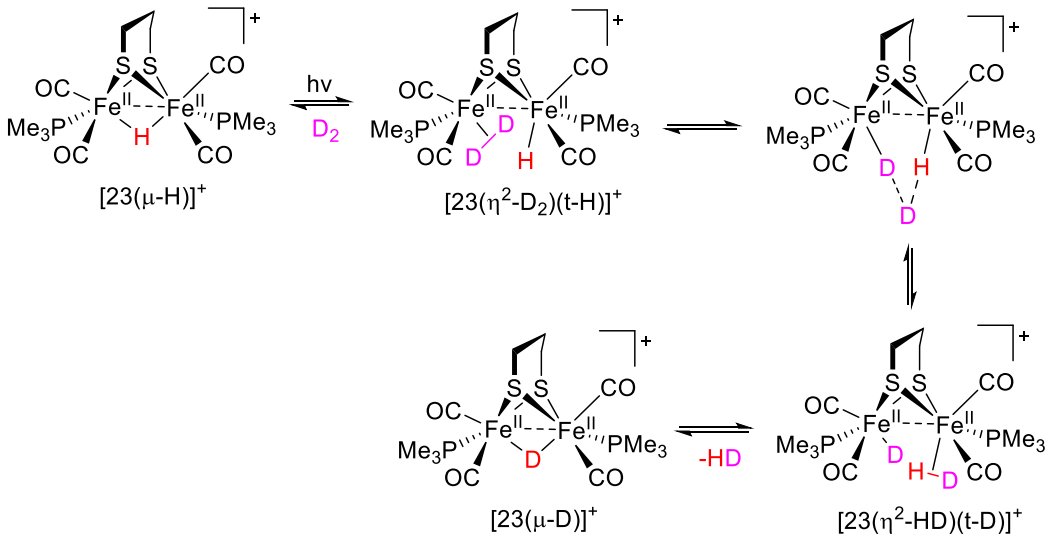

Figure 1.18 H-D exchange through terminal hydride by $[23(\mu\text{-}H)]^+$.

1.1.4.2 Hydride in bio-inspired NiFe complexes

In the [NiFe] H_2ase, bridging hydrides (Fe(μ-H)Ni) with the H atom being closer to the Ni site has been proposed under catalytic process (**see section 1.1.1.2**). In the case of the bio-inspired complexes, the generated hydride species has the tendency to be closer to the M site in the NiM (M= Fe, Ru or Mn) complexes, but not on the Ni site as in the enzyme.[9] The presence of this more thermodynamically favorable bridging hydride structure is proposed to be one of the factors explaining the lower performance of the [NiFe] H_2ase with respect to [FeFe] H_2ase.[24, 71]

Apart NiFe hydride species described above, others have been stabilized with the Ni in a P_2S_2 environment. The first observed NiFe hydride species, $[(dppe)Ni^{II}(pdt)(\mu\text{-}H)Fe^{II}(CO)_3]^+$ ($[24(\mu\text{-}H)]^+$, ^1H NMR δ = −3.53 ppm, X-ray: Fe-Ni: 2.6131(14) Å; Ni-H: 1.64(6) Å, Fe-H: 1.46(6) Å, **Figure 1.19**), [72-74] has been generated from the protonation of the corresponding Ni^IFe^I complex [24] in the presence of HBF_4. This NiFe hydride species is an active electrocatalyst for H_2 production at E_{cat} = −1.20 V vs $Fc^{+/0}$ (η= 0.31 V). This protonation reaction is assisted thanks to the capacity of [24] to undergo a redox isomerization to a formal $Ni^{II}Fe^0$ state. This $Ni^{II}Fe^0$ state is about eight orders of magnitude more basic than the Ni^IFe^I state allowing its rapid protonation to generate the bridging $Ni^{II}Fe^{II}$ hydride.

When one or two CO ligands are replaced by a mono- or di-phosphine ligand, the corresponding hydride species remain in bridging coordination, but still remaining closer to the Fe site (**Figure 1.19**). Indeed, the $[(dppe)Ni^{II}(pdt)(\mu\text{-}H)Fe^{II}(PPh_3)(CO)_2]^+$ complex ($[25(\mu\text{-}H)]^+$, ν_{CO} = 2016 cm^{-1} and 1964 cm^{-1}, ^1H NMR = −3.08 ppm) displays a $d_{Ni\text{-}H}$-$d_{Fe\text{-}H}$ difference of 0.40 Å,[74] an increase compared to 0.18 Å in $[(dppe)Ni^{II}(pdt)(\mu\text{-}H)Fe^{II}(CO)_3]^+$ ($[24(\mu\text{-}H)]^+$), but a decrease with respect to 0.292 Å, found in $[(dppe)Ni^{II}(pdt)(\mu\text{-}H)Fe^{II}(dppe)(CO)]^+$ (($[26(\mu\text{-}H)]^+$), ν_{CO} = 1954 cm^{-1} and 1938 cm^{-1}, ^1H NMR δ = −3.01 ppm) in which two CO have been exchanged.[75] Therefore, the tendency of H^- binding is difficult to determine and is influenced by both steric and electronic effects of the ligand substitution.[7]

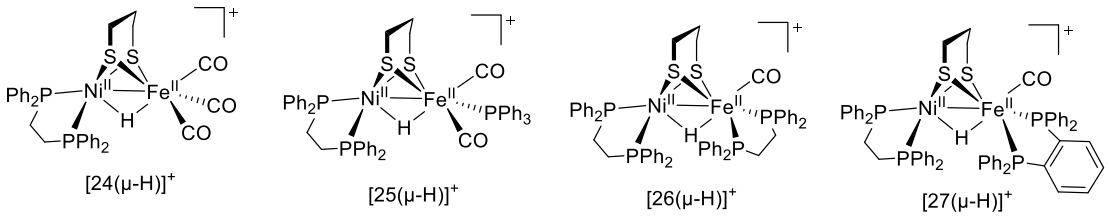

Figure 1.19 The structure of the hydride species.

Interestingly, the value of $d_{Ni\text{-}H}$-$d_{Fe\text{-}H}$ for $[(dppe)Ni(pdt)(\mu\text{-}H)Fe(dppbz)(CO)]^+$ ($[27(\mu\text{-}H)]^+$, dppbz =1,2-bis(diphenylphosphino)benzene, **Figure 1.19**) is −0.010 Å, in which dppe has been replaced by dppbz in complex $[26(\mu\text{-}H)]^+$. This indicates that increasing electron density at the Fe site can shift H^- toward the Ni site, making the structure closer to that found in the [NiFe] H_2ase.[75]

These $Ni^{II}(\mu\text{-}H)Fe^{II}$ models display HER electrocatalytic properties following a [CECE] mechanism (**Figure 1.20** with the $[(dppe)Ni^{I}(pdt)Fe^{I}(CO)_3]$complex, [24], as an example). The hydride $Ni^{II}(\mu\text{-}H)Fe^{II}$ species is proposed to be the first intermediate of the cycle, and its reduction allows a second protonation to occur, followed by the release of H_2. The resulting $Ni^{II}Fe^{I}$ species is then reduced to regenerate the initial $Ni^{I}Fe^{I}$ complex. The electrocatalytic performance of these complexes is comparable with good rate (TOF values around 30 or 60-120 s^{-1}) in the presence of CF_3CO_2H or $ClCH_2CO_2H$, E_{cat} values ranging between −1.20 V and −1.70 V vs $Fc^{+/0}$, and relatively small overpotential (η between 0.50-0.85 V).[7]

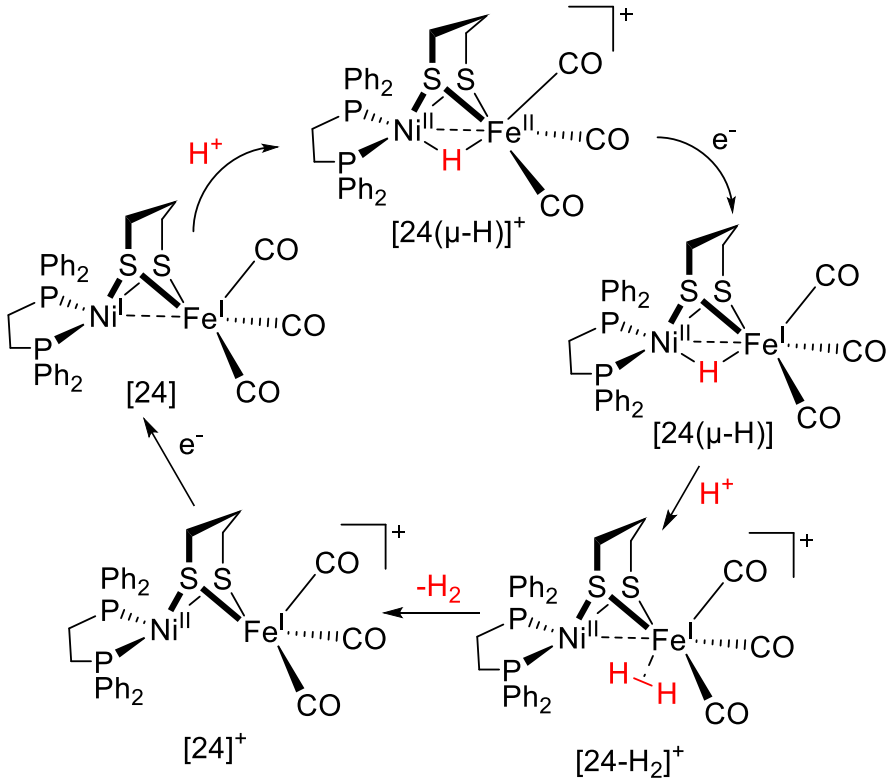

Figure 1.20 Catalytic cycle for H_2 production with the complex [24].

1.1.5 The nature of metals

As mentioned above, the activity of H_2 production can be modulated by ligand modification such as the introduction of basic ligands as proton acceptors or ligands with redox properties in dinuclear NiFe and FeFe complexes. The electrocatalytic activity can also be adjusted by the nature of the metals in the bio-inspired (hetero)dinuclear bio-inspired complexes, including the use of the Co-based complexes.[8, 9]

For example, the Ni site can be replaced by the [Co(NO)] unit in the NiFe ($[18]^+$) complex to generate the heterobimetallic $[(^{alkyl}N_2S_2)Co(NO)FeCp(CO)]^{+}$[76] complex, $[28]^+$. It displays HER activity with a slightly higher overpotential (η =1.06 V, TON = 0.35(±0.05), faradaic efficiency (FE) of 92 ± 1% after 30 min at $E_{cat/2}$ = −1.80 V vs $Fc^{+/0}$) in the presence of TFA, compared to the analogous NiFe complex $[18]^+$ ($E_{cat/2}$ = −1.56 V vs $Fc^{+/0}$, TON = 0.26(±0.01) in 30 min, η = 0.942 V). The complex $[(^{alkyl}N_2S_2)Co(NO)FeCp^*(CO)]^+$ ($[29]^+$), in which Cp has been replaced by Cp* with respect to $[28]^+$ exhibits a milder catalytic performance with a higher overpotential (η = 1.27 V) and a lower value of TON = 0.15(±0.01) (**Figure 1.21**).

In another NiCo complex, the hydride $[Cp^*Co^{II}(pdt)Ni^{III}(t\text{-}H)(dppe)]^{+}$[77] ($[30(t\text{-}H)]^+$) species with a terminal hydride coordinated to the Co site has been isolated (^{1}H NMR δ = −9.77, X-ray: Co–Ni, 2.556(1); Co–H, 1.45(5)). This HER catalyst displays a faradaic efficiency of 91%±5 in the presence of $Cl_2CHCOOH$ (E_{cat} = −1.45 V vs $Fc^{+/0}$, TOF=244 s^{-1})

and follows a [ECEC] mechanism. The Co ion has been replaced by an Fe ion in complex [30] to generate the analogous complex $[Cp^*Fe^{II}(pdt)Ni^{II}(dppe)]^+$. It displays HER electrocatalytic activity in the presence of HOAc in MeCN (TOF = 761 s^{-1}, $E_{cat/2}$ > −2.00 V vs $Fc^{+/0}$) with a proposed [EECC] mechanism.[78] This NiCo complex has a lower value of TOF than $[Cp^*Fe^{II}(pdt)Ni^{II}(dppe)]^+$, but much larger than the analog $[7]^+$. According to the above description, it can be seen that the nature of metal is a factor that can impact the electrocatalytic activity of H_2 production.

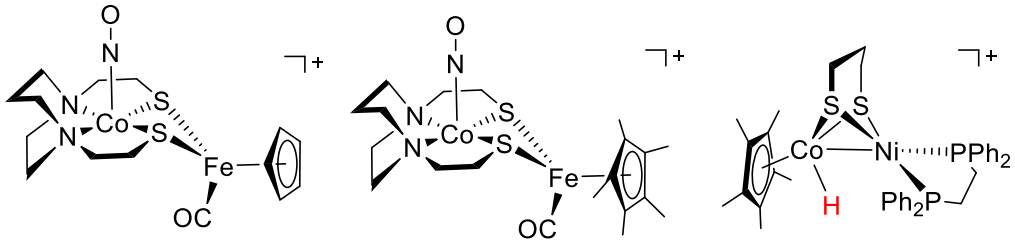

[28]$^+$ [29]$^+$ [30(μ-H)]$^+$

Figure 1.21 The structure of bio-inspired CoFe and CoNi complexes.

Finally, several approaches have been developed over the last decade to mimic the extraordinary reactivity of H_2ases in order to design efficient electrocatalysts for H_2 production. The design of bio-inspired molecular electrocatalysts based on the knowledge acquired, i.e. (i) dinuclear complexes in which both sites work in synergy allowing the stabilization of hydrides (e.g., phosphine-based ligands), (ii) a redox-active site to shuttle electron (such as bipyridine), (iii) a pendant amine or protonable ligands (thiolate with hemilability properties) to serve as proton relays, and (iv) the nature of the metal to tune the catalytic activity. The results obtained seem mixed since none of these systems is able to exhibit reactivity with near-enzyme performance. However, all of these researches have contributed to a detailed understanding of the mechanisms highlighting the key factors that allow optimal control of proton and electron transfer. Moreover, chemists are devoted to developing strategies to solve other challenges including their stability and working conditions (switching from organic solvents to aqueous solutions). Some effective strategies are currently being developed to address these issues, namely incorporation into metallopolymers,[79] confinement in porous materials[80] and immobilization on the surface of an electrode.[81] Therefore, the bio-inspired approach remains a promising strategy that should lead to a breakthrough in the development of high activity electrocatalysts for the production of H_2.

1.2 CO_2 reduction

CO_2 is one of the greenhouse gases that contribute to global warming. It also represents a potential feedstock for the synthesis of value-added fine chemicals and fuels because of its low cost and toxicity, high abundance and relative ease of transport.[82-85] Electrocatalytic CO_2 reduction is thus an attractive pathway to convert CO_2 into organic fuels and useful chemicals.[86, 87] CO_2 reduction involving multielectron processes (>=2e^-) can contribute to the control or even decrease of the

CO_2 concentration in the atmosphere by its chemical valorization, e.g. production C-based products like CO, HCOOH, CH_3OH, HCHO, CH_3CH_2OH, and CH_4, in line with the concepts of atom economy and green chemistry. [82, 85, 88] However, CO_2 has high thermodynamic stability and chemical inertness making it difficult to perform its chemical conversion. The development of efficient, selective, and stable catalysts for CO_2 reduction remains one of the key challenges in the energy conversion domain.[87, 88] A large number of molecular transition metal based electrocatalysts (metals = Fe, Ni, Cu, and Mn, etc.) have been used to catalyze the reduction of CO_2, the synthesis of which involving mainly three types of ligands, i.e., macrocycles, polypyridines, or phosphines.[84, 89-93]

There are also enzymes in nature that can catalyze the reduction of CO_2 to CO, namely the carbon monoxide dehydrogenases (CODHs).[82] In general, two kinds of CODHs can be distinguished due to the different metals present at their active sites. One is the O_2-sensitive NiFe CODH, which reversibly reduces CO_2 to CO close to the thermodynamic potential (E_{cat}= −0.52 V vs SHE at pH=7).[94-96] The second is the air-stable [MoSCu]-containing enzyme, namely MoCu CODH, that catalyzes CO oxidation.[82] In the content of my thesis, MoCu CODH will not be described. The following will discuss the structure of NiFe CODH, its proposed mechanism for CO_2 reduction, and its bio-inspired complexes.

1.2.1 The structure and function of NiFe CODH

The active site of the NiFe CODH contains a [$NiFe_4S_4$] cluster, which consists of a heterodinuclear $NiFe_1$ center bridged by an [Fe_3S_4] cluster that rigidly positions these two metal centers in close proximity (Figure **1.22**).[94, 95] Although the mechanism for CO_2 reduction in the NiFe CODH is still under debate, a two-electron process mechanism has been proposed based on structural, spectroscopic, and kinetic studies (Figure **1.22**).[82] CO_2 is activated by its coordination on the Ni site by the C atom to form a Ni−C bond assisted by a two-electron process. One of the carboxylate oxygen atoms (O_1) forms a hydrogen bond with the Histidine 93 (H_{93}). The resulting CO_2 adduct loses water from Fe_1 with the assistance of two protons, leading to the formation of the Int_3 species, in which O_1 is bound to Fe_1. The Int_3 species then cleaves C-O_1 and releases CO, and regenerates the initial complex with the addition of a water molecule. Regardless of the precise reaction sequence and electronic structure, hydrogen bonding to the protonated histidine residues is important for stabilizing the resulting CO_2 adduct during the catalytic process.

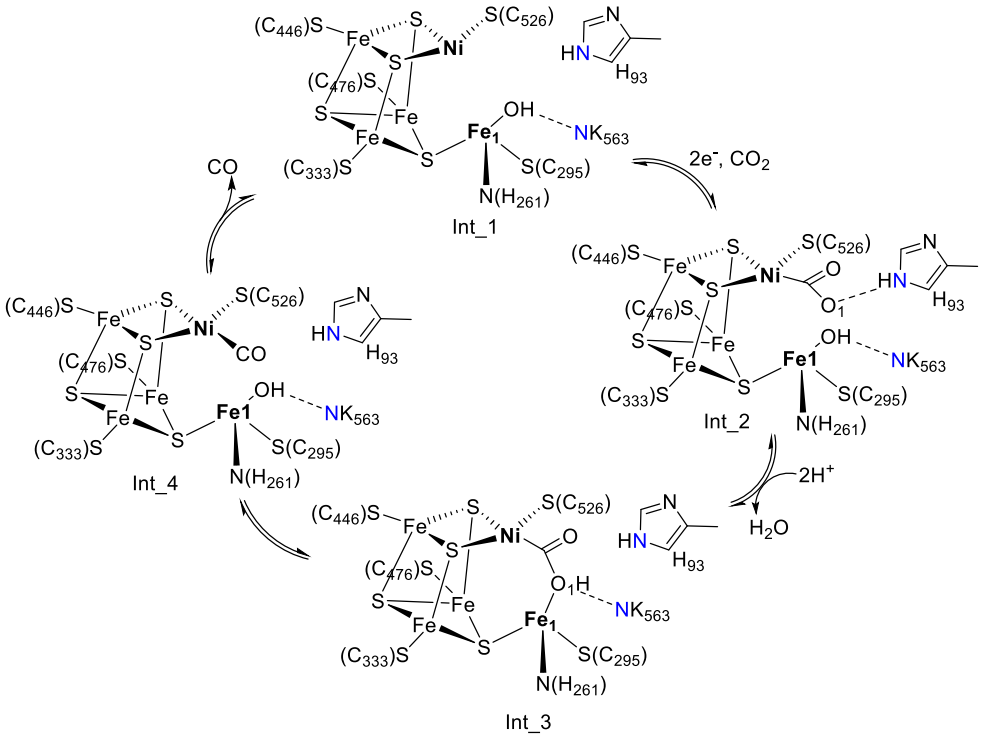

Figure 1.22 Proposed mechanism for the catalytic reduction of CO_2 to CO by the NiFe CODH.

1.2.2 Bio-inspired complexes of the NiFe CODH

Some of the structural and functional models of the NiFe CODH have been described and used to catalyze CO_2 reduction.[82, 96] However, most of the reported molecular catalysts for CO_2 reduction are mononuclear complexes, and only a few binuclear molecular catalysts have been employed so far.[97] For example, the design of the $[Co^{II}(dppe)PyS_2]$ [31] complex[98] is inspired by the active site of the NiFe CODH. The CO_2 activation step involves the protonation of one metal-bound thiolate accompanied by the oxidation of the Co^{I} center into a Co^{III}. CO_2 is selectively reduced into CO catalytically in the presence of two protons with a low overpotential (< 100 mV, FE > 93%, E_{cat}= −1.2 to −1.7 V vs $Fc^{+/0}$) (**Figure 1.23**). More precisely, CO_2 binds the Co^{I} site to afford a Co^{III}–COOH species. This Co^{III}–COOH intermediate undergoes protonation and C–OH cleavage to release H_2O and CO. In this case, in the presence of H_2O as a proton source, the complex [31] is selective for CO_2 reduction with only trace of generated H_2 (E_{cat} > −1.3 V, E_{cat} < −1.3 V without H_2). Interestingly, when TFE (2,2,2-Trifluroroethanol) is used as a proton source, H_2 production occurs but not CO_2 reduction. Under these experimental conditions, CO_2 does not bind the Co^{I} site, because it can coordinate only when the thiolate is protonated.

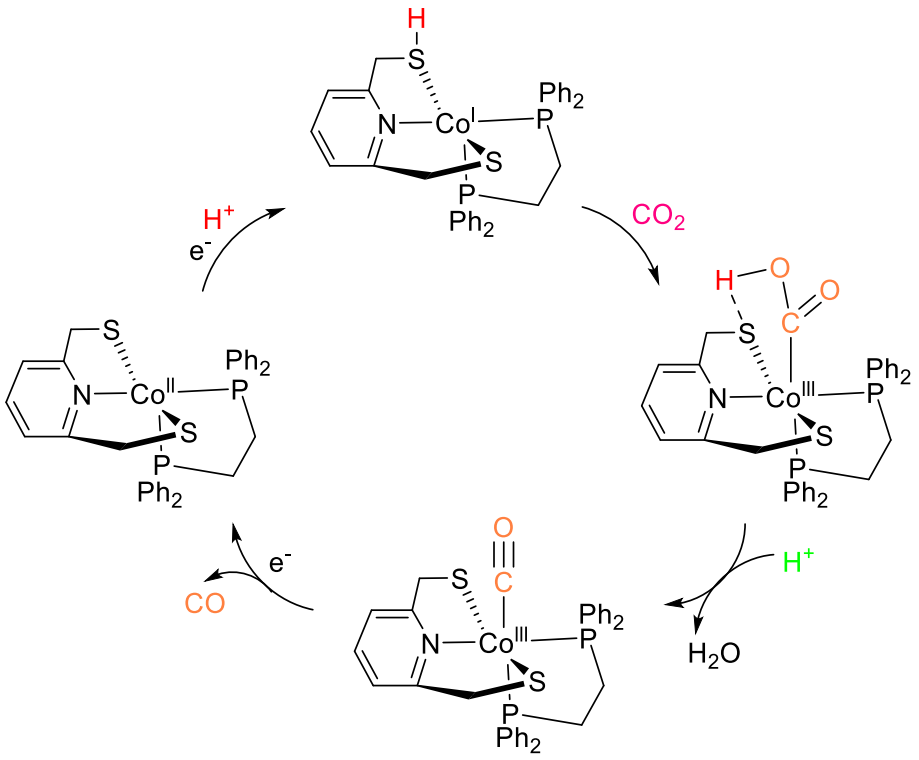

Figure 1.23 Catalytic cycle for CO_2 reduction with the complex [31].

As mentioned above, the catalytic process of both the NiFe CODH and H_2ases involves acid-base reactions and electron transfer processes. Moreover, the two enzymes, the NiFe CODH and H_2ase, display similar key structural features in their active sites: both contain a heterodinuclear FeNi unit with a thiolate-rich coordination sphere. It is reasonable to guess that catalysts inspired by the H_2ases could be capable of catalyzing CO_2 reduction. Both the reduction of CO_2 to CO and the reduction of protons to H_2 involve two-electron processes. It should be noted that NiFe CODH catalyzes CO_2 reduction to CO without the formation of hydride; while hydrides represent key intermediates during the catalytic cycle for H_2 production.

The bio-inspired [FeFe] H_2ase complexes [(μ-bdt)$Fe_2(CO)_6$] ([32]) and [(μ-edt)$Fe_2(CO)_6$] (edt = 1,2-ethanedithiolate) have been used to catalyze the CO_2 electroreduction into HCOOH and CO.[99] In detail, for [(μ-bdt)$Fe_2(CO)_6$], a faraday efficiency of 71% for formic acid, 10% for CO and 7% for H_2 has been measured at E_{cat}= −2.35 V in 0.1 M MeOH/MeCN under CO_2. The complex [(μ-edt)$Fe_2(CO)_6$] displays milder performance for CO_2 reduction under similar conditions (48% for formic acid, 22% for CO, and no H_2).

Based on density functional theory (DFT) calculations and experiments, it has been shown that the complex [32] is not the entry in the catalytic cycle but its two-electron reduced form ($[32]^{2-}$) (E_{pc}= −1.33 V vs $Fc^{+/0}$) (**Figure 1.24**). One of the thiols becomes coordinated to only one Fe site, resulting in a structural isomerization with one CO ligand becoming bridging in $[32]^{2-}$. In the presence of a proton source,

$[32]^{2-}$ then reacts with CO_2 to produce a CO_2 adduct $[32\text{-}CO_2]^-$, in which one of the O atoms of CO_2 binds to the neighboring Fe site, accompanied by the protonation of the terminally bound thiolate and the decoordination of one CO ligand. Subsequently, an intramolecular proton transfer from the thiolate to the uncoordinated O atom of OCO occurs. The $[32H\text{-}COOH]^-$ species is generated by a one-electron reduction step (E_{pc}= −1.8 V vs $Fc^{+/0}$) followed by a protonation step that leads to the cleavage of the Fe−O bond combined with the rearrangement of one CO ligand that becomes bridging. Finally, the reduction of this species leads to either, (i) the release of COOH and the regeneration of $[32]^{2-}$ with the addition of one CO, or (ii) the release of CO and H_2O with the direct regeneration of $[32]^{2-}$. During this catalytic cycle, the synergistic effect of the close diiron centers plays an important role in activating CO_2. Indeed, CO_2 is activated by its coordination through the C and O atoms at the two Fe sites, respectively, mimicking the CO_2 activation mode proposed in the [NiFe]-CODH enzymes.[95] This work enriches the versatility of the [FeFe] H_2ase models in catalytic aspects beyond proton reduction.

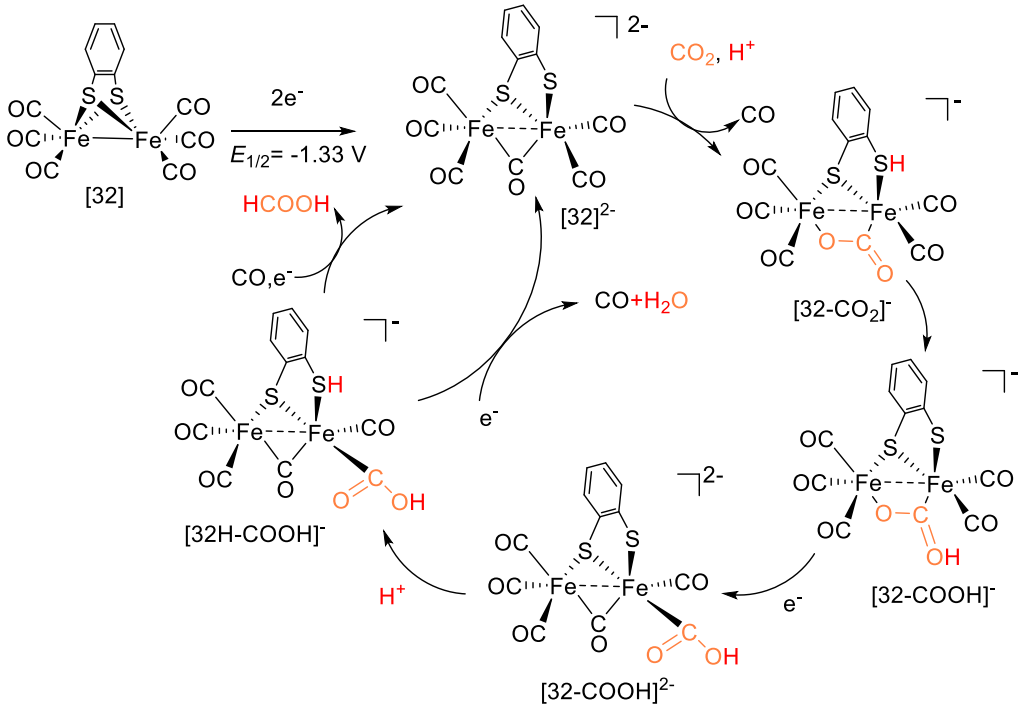

Figure 1.24 Proposed pathways for the electrochemical CO_2 reduction with the bio-inspired FeFe complex [32].

Interestingly, the bio-inspired complex $[5]^+$ is also a multifunctional catalyst that can not only catalyze H_2 production but also CO_2 reduction.[100] As already discussed above, $[5]^+$ can be immobilized on graphite (EPG) by physical adsorption to form a hybrid catalyst $Ni^{II}Fe^{II}Cp$/EPG. While, in pH 4 acidic aqueous solutions, the cathodic event is assigned to the HER under Ar, in the presence of CO_2, the catalytic wave displays a positive shift of 150 mV, which has been defined as the occurrence of an event process in relation with CO_2 reduction (**Figure 1.25**). After electrolysis at E_{cat}= −1.3 V vs SHE at pH 4 in phosphate buffer, it has been demonstrated that $Ni^{II}Fe^{II}Cp$/EPG

reduces CO_2 electrocatalytically into a mixture of CH_4 (FE = 12%), the unique C-based product identified and H_2 (FE = 62%). A proposed catalytic process for the production of CH_4 involves both the Ni and Fe sites: the Ni site to stabilize the hydride species, and the Fe site to activate CO_2. In other words, CO_2 is activated and converted at the Fe site, while the Ni site generates hydrides and transfers them to the Fe site until CH_4 is formed and released. Interestingly, it has been confirmed experimentally that the molecular structure of $[5]^+$ immobilizing on EPG is completely preserved after electrolysis.

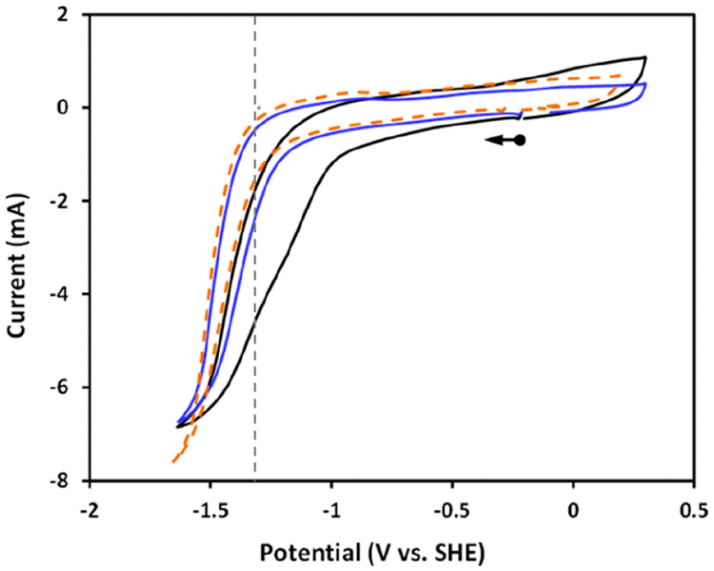

Figure 1.25 CVs of $Ni^{II}Fe^{II}Cp$/EPG under either Ar (blue line) or CO_2 (black line) and pristine EPG under CO_2 (dashed orange) in acid aqueous of 0.1 M KPF_6 at 50 mV/s. Conditions: Ag/AgCl (satd. KCl) as reference electrode and Pt as the counter electrode.

1.2.3 The role of pendant amine in CO_2 reduction

Even though many catalysts have been employed for CO_2 reduction with high activity, the catalytic performance of some complexes still needs to be developed compared to that of enzymes. Therefore, it is no doubt that for some catalysts, we hope to tune their electrocatalytic activity (lower overpotential and higher selectivity) for CO_2 reduction through some strategies, for example, the incorporation of pendant amine ligands. As for H_2 production, the presence of a pendant amine in the second coordination sphere can act as a proton relay to shuttle protons, and can also be responsible for adjusting the electronic structure of the metal center to modify the electrochemical performance of the complexes. It is therefore inferred that the presence of a pendant amine should also have the ability to tune the properties of CO_2 reduction electrocatalysts, as demonstrated by some examples reported in the literature.

An Fe porphyrin complex[101] bearing a pendant amine group ([33], **Figure 1.25**)

catalyzes CO_2 reduction to HCOOH at −1.55 V vs $Fc^{+/0}$ under saturated CO_2 conditions with 1 M H_2O in DMF (Faradaic yield = 97 ± 1%, η = 50 mV, TON = 5 × 10^5, TOF = 50 S^{-1}). The CV of [33] shows that the Fe^{I} oxidation state does not react with CO_2 in the absence of H_2O, but a positive shift of about 100 mV is observed when H_2O is added. It has been proposed that the amine group is protonated by H_2CO_3, and DFT calculations indicate that CO_2 binds to the Fe^{I} state to produce a CO_2 adduct only when the pendant amine is protonated. For complex [34] that does not contain the pendant amine group, CO_2 reduction does not occur under similar conditions demonstrating that protonation of the pendant amine is critical for CO_2 binding during the catalytic process.

In addition, the $NiL^{N2O2}NH_2$ complex ([35], **Figure 1.25**) has the ability to convert CO_2 into a mixture of products (faraday efficiency: 11.2% of HCOOH, 15.7% of CH_3OH, 35.5% of C_2H_5OH, 7.4% of CH_3CHO and 25.5% of H_2 in 20 min) at E_{cat} = −1.8 V vs Ag/AgCl in the CO_2 saturated of 0.5 M K_2CO_3 solution after its immobilization on graphite.[102] Interestingly, only H_2 is produced when the complex [36], which does not bear a pendant amine, is immobilized at the electrode under similar conditions. In this case, complex [36] lacks the catalytic activity towards CO_2 reduction (**Figure 1.25**). It can be seen that the -NH_2 group plays a crucial role in this catalytic process.

The above discussion confirms that a pendant amine has the ability to modify the catalytic activity of CO_2 reduction, and it thus may be a promising strategy in the design and synthesis of electrocatalysts for CO_2 reduction with optimized performance.

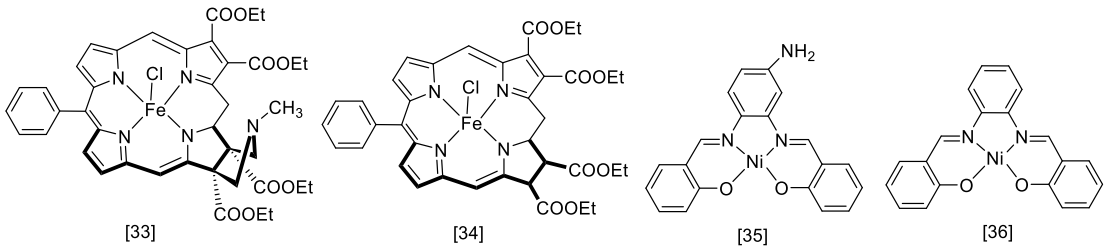

Figure 1.25 The molecular structures of mononuclear Fe and Ni complexes.

In this section, several methods have been described in order to design efficient electrocatalysts for CO_2 reduction, i.e. (i) a bio-inspired complex of NiFe CODH (e.g., a Co-based catalyst), (ii) bio-inspired dinuclear NiFe or FeFe complexes of H_2ases, and (iii) catalysts with a pendant amine. Based on these data, the bio-inspired approach is thus also considered as a promising strategy to develop high-activity electrocatalysts for CO_2 reduction.

1.3 Motivation and plan of thesis

To date, several methods (redox-active ligands, potential proton relay, and active hydride species) have been developed to mimic the extraordinary reactivity of H_2ases

to design efficient electrocatalysts for H_2 production. However, the performance of these models is still not comparable to those of [FeFe] and [NiFe] H_2ases. Fortunately, an understanding of the mechanisms has contributed to highlighting the key factors (electron and proton relays, and active hydrides) providing guidance for the further design of highly active electrocatalysts for H_2 production. By bringing together all this knowledge together, these bio-inspired electrocatalysts thus remain a promising strategy for H_2 production with high activity (for example, lower overpotential).

CO_2 reduction is considered an efficient approach to CO_2 utilization. CO_2 can be converted to CO or other C1 products (i.e. CH_4, HCOOH, and CH_3OH, etc.) by multi-electron and multi-proton processes. Many electrocatalysts have also been used to catalyze CO_2 reduction. The same problem with H_2 production is that no catalytic system can match the performance of the natural systems (NiFe CODH). The strategy of incorporating pendant amine in complexes has been developed to design efficient electrocatalysts for CO_2 reduction. In addition, it is noted that the active sites of two enzymes (NiFe CODH and H_2ases) display similar key structural features. Their catalytic processes both involve electron transfer and synergy between the Ni and Fe sites. Not surprisingly, bio-inspired complexes of H_2ases thus catalyze the reduction of CO_2 under electrocatalytic conditions. However, H_2 production is in competition with CO_2 reduction. Hydrogen can also be selectively produced during CO_2 reduction. This means that the selectivity of the electrocatalyst for CO_2 reduction is reduced.

In previous works, a family of electrocatalysts have been synthesized by modeling the structural features and function of active site functions of NiFe and FeFe H_2ases denoted as $[(L^{N2S2})Ni^{II}Fe^{II}Cp(CO)]^+$ ($Ni^{II}Fe^{II}Cp$), $[(L^{N2S2})(MeCN)Fe^{II}(CO)Fe^{II}Cp]^+$ ($Fe^{II}Fe^{II}Cp$), and $[(L^{N2S2})Ni^{II}Fe^{II}Cp^*(CO)]^+$ ($Ni^{II}Fe^{II}Cp^*$), (**see section 1.1.2.2**, **Figure 1.26**). They display similar catalytic performance for H_2 production under similar conditions. Especially, the $Ni^{II}Fe^{II}Cp$ complex can catalyze H_2 production and CO_2 reduction in an acidic aqueous solution after immobilizing on graphite electrodes.

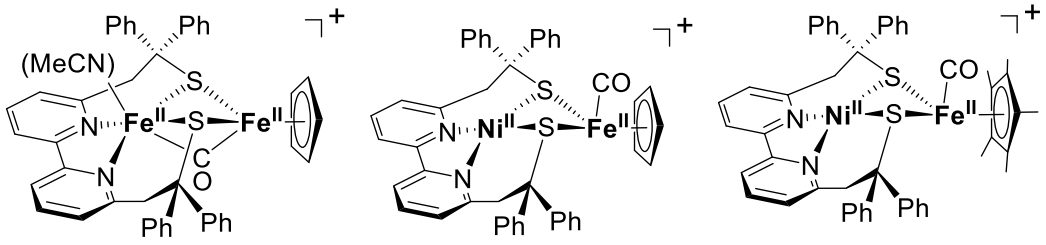

$[4]^+$, $Fe^{II}Fe^{II}Cp$ $[5]^+$, $Ni^{II}Fe^{II}Cp$ $[6]^+$, $Ni^{II}Fe^{II}Cp^*$

Figure 1.26 Structures of the different bio-inspired HER electrocatalysts.

Inspired by the above works, the aim of this thesis is to improve the electrocatalytic activity of these systems in particular by lowering the overpotential for H_2 production and CO_2 reduction. We mainly investigated the redox properties of compounds and their catalytic activities from two aspects, namely the impact of the metal and the design of ligands. The thesis has been divided into the following aspects.

It has been reported in the literature that Co-based complexes displayed good performance for H_2 production. For example, the complex $[28]^+$ displays a faradaic efficiency of 92 ± 1% for H_2 production. Additionally, both complexes $Ni^{II}Fe^{II}Cp$ and $Fe^{II}Fe^{II}Cp$ give good performance for H_2 production under similar conditions. Therefore, the Ni ion has been substituted by a Co ion to synthesize the corresponding CoFe complex, and its electrocatalytic activity for H_2 production is reported in Chapter 2.

The redox properties of the $M^{II}Fe^{II}Cp$ complexes and their electrocatalytic activities for HER (M= Ni and Fe) have been investigated in the literature. This series of complexes still displays higher overpotential with the respect to the enzymes. According to the previous reports (see **section 1.1.3**), the addition of a pendant anime that can act as a proton relay can improve the activity of the electrocatalyst for H_2 production by reducing the overpotential. Inspired by this result, in chapter 3, our aim is to modify the $Ni^{II}Fe^{II}Cp$ complex at the Fe site with the introduction of a potential proton relay in the second coordination sphere, by replacing the Fe-bound cyclopentadienyl (Cp) with the picolyl cyclopentadienyl (PyCp) and 2-(diethylamino)ethyl-cyclopentadienide (CpN), to investigate how this modification will affect the HER electrocatalytic performance of the resulting heterodinuclear MFe (M= Ni and Co) complexes. Considering that most of the isolated complexes suffer from limited stability or/and low solubility in water[35, 80] required for sustainable applications, immobilizing molecular catalysts on electrode surfaces to produce a heterogeneous catalyst is a promising strategy to overcome these drawbacks. This novel NiFe complex was thus immobilized on electrode surfaces to investigate the activity of H_2 production in acid aqueous solutions.

The $Ni^{II}Fe^{II}Cp$ complex can catalyze CO_2 reduction to yield a mixture of products (H_2 and CH_4) under heterogeneous conditions. Therefore, in chapter 4, the new MFe complexes containing a pendant amine have been used to investigate their activity toward CO_2 reduction under homogeneous and heterogeneous conditions.

Diphosphine ligands are electron-rich ligands that can effectively adjust the electronic structure of the active metal to improve the electrocatalytic activity. FeFe or NiFe complexes with diphosphine ligands have also been reported to be effective for electrocatalytic H_2 production. In chapter 5, we attempted to synthesize new dinuclear NiFe complexes by substituting Cp with diphosphine ligands.

Chapter 2 A bio-inspired heterodinuclear CoFe complex

2.1 Introduction

H_2ases are metalloenzymes present in certain organisms, bacteria or microalgae, which have the capacity to catalyze reversibly the oxidation of hydrogen from protons and electrons at a potential close to the thermodynamic potential.[12, 103-105] According to their active site, they have been divided into two main classes, i.e. the [NiFe] and [FeFe] H_2ases (**Figure 1.1**). The active site of the [NiFe] H_2ase consists in a heterodinuclear NiFe complex, with the two metal ions bridged by thiolate functions from cysteine residues of the polypeptide chain. In the case of the [FeFe] H_2ase, its active site is a dinuclear iron complex with the two Fe ions also connected by two thiolate functions arising from azadithiolate ligand. Besides, the active sites of both two [MFe] H_2ases (M = Ni or Fe) present carbon monoxide (CO) and cyanide (CN^-) linked by iron metals. Thus, mimicking the activity of these enzymes by bio-inspired complexes to develop new catalysts for H_2 production is an attractive strategy for chemists.[6, 106-108]

Recently, two dinuclear bio-inspired $M^{II}Fe^{II}$ (M = Fe or Ni) complexes have been synthesized with similar structures. Both $Ni^{II}Fe^{II}Cp$[81, 109] and $Fe^{II}Fe^{II}Cp$[110, 111] complexes display comparable electrocatalytic performance for H_2 production, following a common E[ECEC] catalytic mechanism (**Figure 1.26**). Experiments and DFT calculations confirm that the non-innocent redox activity of the bipyridine ligand dominates the catalytic process.[112] Since Co complexes have been shown high performance for H_2 production in the relevant literatures, [113-116] we have replaced the Ni ion in the parent $Ni^{II}Fe^{II}Cp$ complex into a Co ion to synthesize and characterize the analogue $[(L^{N2S2})Co^{II}Fe^{II}Cp(CO)]^+$ complex ($Co^{II}Fe^{II}Cp$). Its redox properties as well as its electrocatalytic activity for H_2 production have been investigated with the aim of comparing its reactivity with its analogous NiFe and FeFe complexes.

2.2 Results and Discussion

2.2.1 Synthesis and characterization of $Co^{II}Fe^{II}Cp$

The complex $Co^{II}Fe^{II}Cp$ has been obtained as a brown solid from the reaction between a stoichiometric amount of $[Co^{II}(L^{N2S2})]$ (CoL) and $[Fe^{II}(CO)(Cp)(CH_3CN)_2]BF_4$ (FeCp) in distilled CH_2Cl_2 at room temperature under argon, isolated in a 80% yield (**Figure 2.1**). The ultraviolet–visible (UV-vis) spectrum of a solution of $Co^{II}Fe^{II}$ in dimethylformamide (DMF) displays two transitions at 468 nm (ε = 4900 $M^{-1}cm^{-1}$) and

584 nm (ε = 3100 $M^{-1}cm^{-1}$), distinct from the spectra of the mononuclear complexes (**Figure 2.2**). In the electrospray ionization mass spectrum (ESI-MS), a peak at m/z = 786.04 (calc. 786.09) is observed, assigned to the expected $Co^{II}Fe^{II}Cp$ complex.

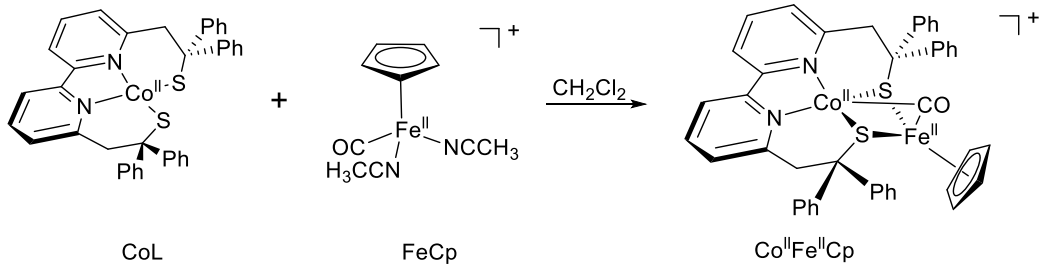

Figure 2.1 Synthesis of the complex $Co^{II}Fe^{II}Cp$.

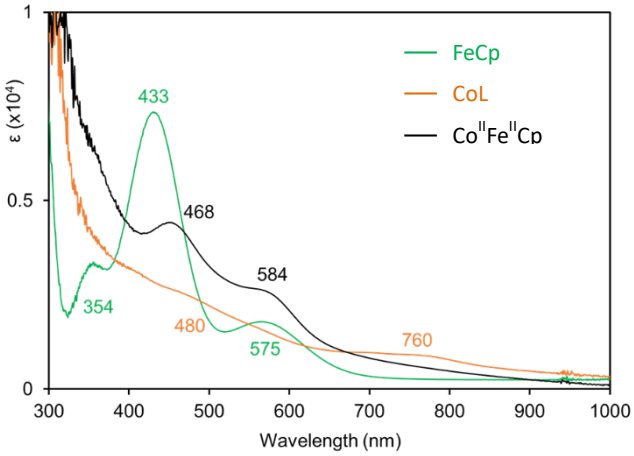

Figure 2.2 UV-visible spectra of $Co^{II}Fe^{II}Cp$ (black), CoL (orange), and FeCp (green). Complex concentration = 0.1 mM in DMF.

Attenuated total reflectance infrared (ATR-IR) spectroscopy is employed to monitor the binding mode of the CO ligand. In the solid-state IR spectrum of $Co^{II}Fe^{II}Cp$, the CO vibration is observed at 1856 cm^{-1} (**Figure 2.3**), which belongs to the range expected for metal-bridging CO moieties. Its energy is close to the bridged M-CO-M (M: metal) stretching vibration found in $Fe^{II}Fe^{II}Cp$[32] (1822 cm^{-1}), and significantly lower than the terminal M-CO vibration present in the FeCp complex[117] and the analogous $Ni^{II}Fe^{II}Cp$ complex[109] (1984 and 1929 cm^{-1}, respectively). Based on these data, it can be concluded that the CO bridges the Co^{II} and Fe^{II} ions in $Co^{II}Fe^{II}Cp$.

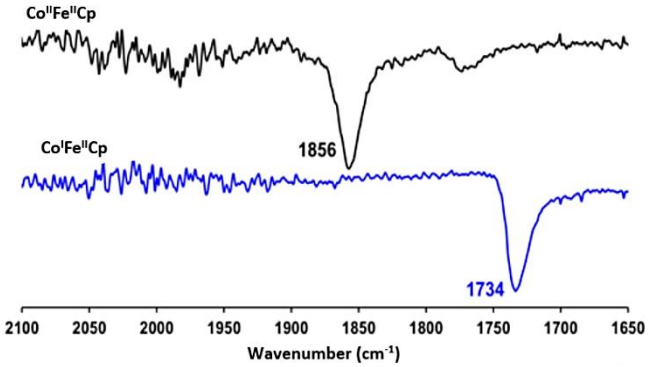

Figure 2.3 ATR-IR spectra of the $Co^{II}Fe^{II}Cp$ (black line) and $Co^{I}Fe^{II}Cp$ (blue line).

In order to gain insights into the electronic structure of $Co^{II}Fe^{II}Cp$, EPR (electron paramagnetic resonance) spectra have been recorded both as a powder sample and as a frozen DMF solution sample at 100 K (**Figure 2.4**). The solid-state sample shows a rhombic spectrum (g_x = 2.24; g_y = 2.09; g_z = 1.98) consistent with a low-spin d^7 Co^{II} species (**Figure 2.4**, left). In this case, the d^6 Fe^{II} centre does not contribute to the spectrum indicating that the single unpaired electron of the overall S = ½ complex is localized on the Co center. Hyperfine interaction (I = 7/2 for ^{59}Co) is resolved in the frozen DMF solution sample spectrum, supporting the Co^{II} assignment (**Figure 2.4**, right).

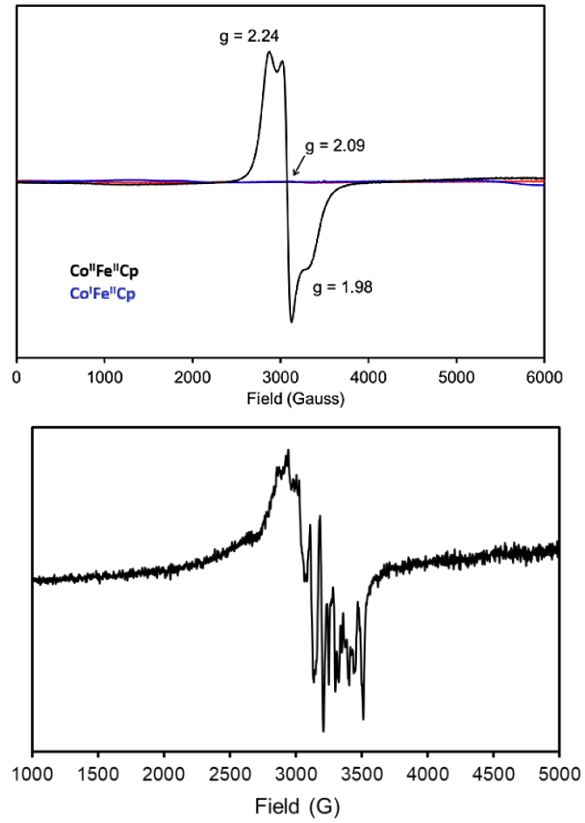

Figure 2.4 Solid-state EPR (left) spectra of $Co^{II}Fe^{II}Cp$ (black) and $Co^{I}Fe^{II}Cp$(blue) recorded at 100 K. EPR spectrum (right) of $Co^{II}Fe^{II}Cp$ in a DMF solution (5 mM) recorded at 100 K.

To further investigate the structural and spectroscopic properties of $Co^{II}Fe^{II}Cp$, its optimized structure have been predicted by DFT calculations. The Mulliken spin population of 1.1 on the Co ion is fully consistent with a localized S = ½ $Co^{II}Fe^{II}$ complex as proposed by the experimental EPR data (see **Figure 2.5** for the spin density). The calculated stretching vibration of CO is predicted at 1887 cm^{-1}, which is consistent with the experimental ones (1856 cm^{-1}). DFT calculations confirm that the overall spin state of the complex is a doublet (the quartet is predicted to be at a much higher energy, see **Table 2.1**).

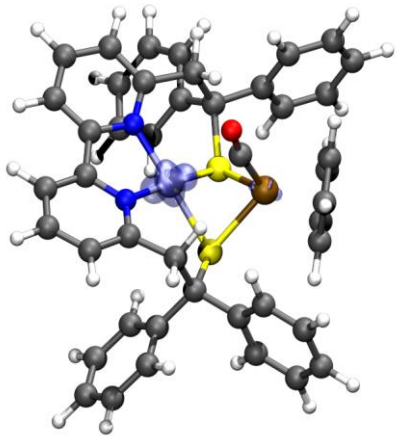

Figure 2.5 The DFT calculated structure of $Co^{II}Fe^{II}Cp$ (ball and stick manner representation), with the (positive) spin density in light transparent blue. Atoms: Carbon (grey), oxygen (red), nitrogen (blue), hydrogen (white), sulfur (yellow), iron (ochre), and cobalt (cyan).

Table 2.1 Energies of the quartet relative to the doublet for calculated $Co^{II}Fe^{II}Cp$ structure. Energies are expressed in kcal/mol.

	BP86	B3P86
Doublet	0	0
Quartet	21.71	13.18

2.2.2 Redox properties of $Co^{II}Fe^{II}Cp$

The cyclic voltammetry (CV) of $Co^{II}Fe^{II}Cp$ has been carried out in DMF due to its poor solubility in acetonitrile (MeCN). The CV displays two diffused-controlled (quasi-) reversible one-electron processes, centered at $E_{1/2}$ = −1.00 V ($\triangle E$ = 100 mV) and $E_{1/2}$ = −2.04 V ($\triangle E$ = 80 mV) versus $Fc^{+/0}$ (**Figure 2.6**). The first redox process at −1.00 V can be attributed to the $Co^{II/I}$ reduction, and the second one at −2.04 V, to the reduction of the redox-non-innocent bipyridine ligand. In addition, the $Co^{II/I}$ reduction potential is calculated to be −1.02 V vs $Fc^{+/0}$ via DFT calculations (**Table 2.2**), which is in agreement with the experimental one (−1.00 V).

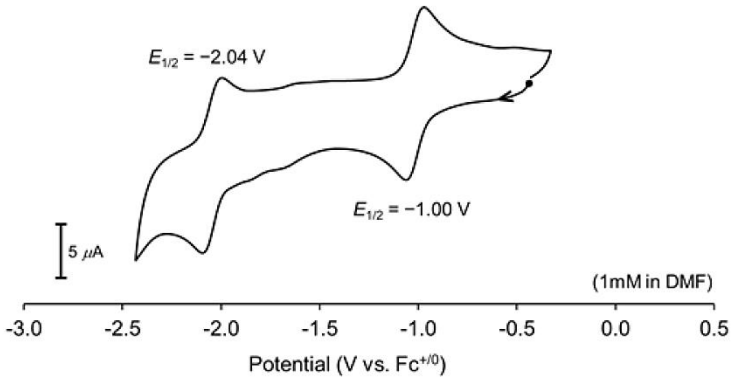

Figure 2.6 CV of a DMF solution of $Co^{II}Fe^{II}Cp$ (1 mM); electrolyte: 0.1 M $(Bu)_4NClO_4$; reference: $Ag/AgNO_3$; counter: Pt wire; scan rate: 100 mV/s.

Table 2.2 Calculated redox potential of the $[Co^{II}Fe^{II}Cp]^+/[Co^{I}Fe^{II}Cp]$ couple.

	Redox potential (V vs $Fc^{+/0}$)	
E_{calc}(MeCN)	BP86	B3P86
	−0.56	−1.02

For the analogue $Ni^{II}Fe^{II}Cp$,[33] the CV shows a first reversible redox process at −1.29 V vs $Fc^{+/0}$ in MeCN, attributed to the $Ni^{II/I}$ reduction process. The reduction of the Ni^{II} ion occurs at a significantly more positive potential shift of 530 mV than that of the mononuclear $[Ni^{II}(L^{N2S2})]$ (NiL) complex under the same conditions, highlighting the strong electronic effect of the Lewis acidic Fe component. However, the $Co^{II/I}$ reduction potential in $Co^{II}Fe^{II}Cp$ is shifted to an even greater extent by 700 mV as compared to the mononuclear CoL in DMF.[14] In the case of $Fe^{II}Fe^{II}Cp$,[32] the diiron analogue exists as a *mono*-CO bridging mode in MeCN, its first one-electron redox system occurs at −1.21 V vs $Fc^{+/0}$ resulting in the delocalized, mixed-valent $Fe^{1.5}Fe^{1.5}Cp$ species. Based on above discussions, $Co^{II}Fe^{II}Cp$ is the easiest to reduce in this series of $M^{II}Fe^{II}$ complexes.

In $Ni^{II}Fe^{II}Cp$ and $Fe^{II}Fe^{II}Cp$ complexes, their second one-electron reduction process in MeCN occurs at $E_{1/2}$ = −1.90 V and $E_{1/2}$ = −1.65 V vs $Fc^{+/0}$, respectively, attributed to the reduction of the redox active bipyridine ligand. In the case of $Co^{II}Fe^{II}Cp$, the redox system associated with the bipyridine ligand occurs at a less negative potential at $E_{1/2}$ = −2.04 V in DMF. The small difference with $Ni^{II}Fe^{II}Cp$ can be explained by the difference of the solvent (DMF vs MeCN), while that with $Fe^{II}Fe^{II}Cp$ can arise from differences in the structural and electronic properties of the one-electron reduced species (**see 2.2.3**).

2.2.3 Synthesis and characterization of the one-electron reduced $Co^{I}Fe^{II}Cp$ species

The $Co^{II}Fe^{II}Cp$ complex can be chemically reduced using one molar equivalent of cobaltocene ($CoCp_2$) in MeCN, to generate the one-electron reduced species with the yield of 85% (**Figure 2.7**). This product is characterized by EPR, IR and UV-vis spectra. The EPR spectrum of reduced species is silent (**Figure 2.4**, left), that confirms an overall S = 0 complex (Co^{I}, d^8; Fe^{II}, d^6). The IR spectrum displays a CO stretching vibration at 1734 cm^{-1} consistent with a bridging mode (**Figure 2.3**). Distinct changes in UV-vis spectra are observed upon reduction (**Figure 2.8**, left), including the growth of a broad at 950 nm. The transition at 950 nm is attributed to low-energy d-d transition feature by DFT calculations (**Figure 2.8**, right). According to experimental and electrochemical analysis, it can be concluded that the one electron reduction occurs at the cobalt center to form the $Co^{I}Fe^{II}Cp$ species. The CO vibration of $Co^{I}Fe^{II}Cp$ is at a notably weaker energy with respect to $Co^{II}Fe^{II}Cp$ (1856 cm^{-1}).

The structural and spectroscopic properties of $Co^{I}Fe^{II}Cp$ have been further investigated by DFT calculations. For the optimized structure ($Co^{I}Fe^{II}Cp°$), the predicted CO stretching vibration is predicted to be at 1779 cm^{-1}, consistently with the experimental one (1734 cm^{-1}). The overall spin state of the complex is confirmed to be a singlet in agreement with the EPR silent spectrum.

For the $Ni^{II}Fe^{II}Cp$ analogue, its one electron reduction occurs at the nickel center to form $Ni^{I}Fe^{II}Cp$ and its CO vibration is observed at 1770 cm^{-1} consistent with a bridging coordination mode. Its energy is close to the bridged M-CO-M vibration found in $Co^{I}Fe^{II}Cp$ (1734 cm^{-1}). On the other hand, in the case of the delocalized mixed-valence species ($Fe^{1.5}Fe^{1.5}Cp$) generated upon the one electron reduction of $Fe^{II}Fe^{II}Cp$, the CO vibration at 1896 cm^{-1} is consistent with a terminal mode. Therefore, the structure and electronic properties of the one-electron reducing form of $Ni^{II}Fe^{II}Cp$ and $Co^{II}Fe^{II}Cp$ differ from that of $Fe^{II}Fe^{II}Cp$, which can explain the difference in their redox properties regarding the second reduction process (**see 2.2.2**).

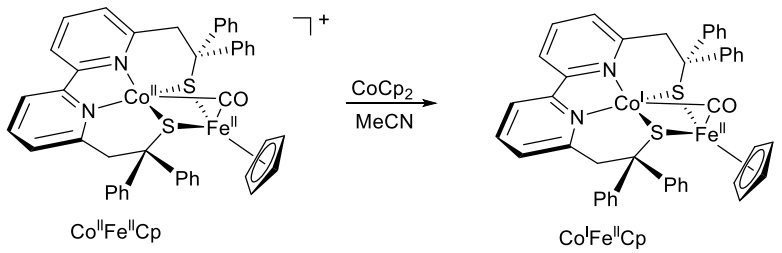

Figure 2.7 Synthesis of the complex $Co^{I}Fe^{II}Cp$.

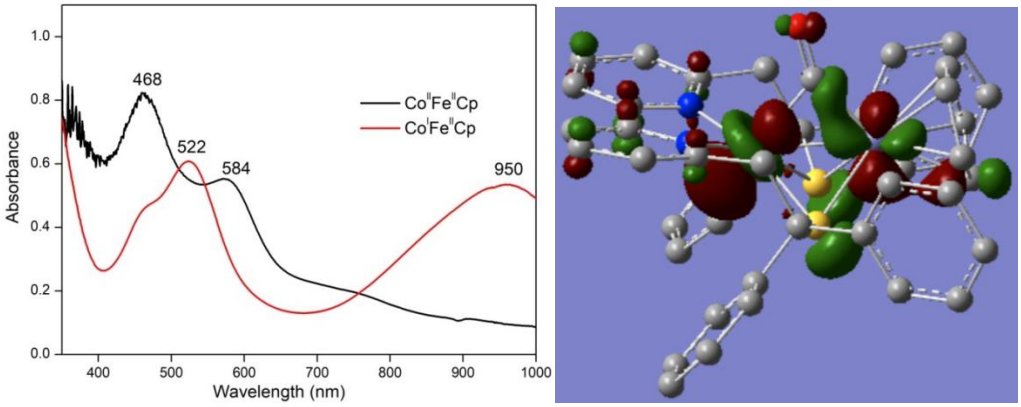

Figure 2.8 UV-vis spectra (left) of the $Co^{II}Fe^{II}Cp$ (black) and $Co^{I}Fe^{II}Cp$ (red) complexes in DMF (0.1 mM, 10 mm). The highest occupied molecular orbital (HOMO) of $Co^{I}Fe^{II}Cp$ (left).

2.2.4 Reactivity of $Co^{II}Fe^{II}Cp$ in the presence of proton

Following the addition of Et_3NH^+ as a proton source, a catalytic process (E_{cat} = −1.99 V versus $Fc^{+/0}$, measured at the middle wave at a concentration of 3.65 mM of Et_3NH^+) develops on top of the second wave of $Co^{II}Fe^{II}Cp$ complex (**Figure 2.9**). Nevertheless, when compared with the CVs recorded under the same conditions, but in absence of $Co^{II}Fe^{II}Cp$, a similar catalytic potential is observed, evidencing that the presence of $Co^{II}Fe^{II}Cp$ has a marginal impact for H_2 production. This means that this complex is not active for the electrochemical production of H_2. This behavior was completely unexpected, because both $Ni^{II}Fe^{II}Cp$ and $Fe^{II}Fe^{II}Cp$ have displayed good electrocatalytic activity for H_2 production. Their comparable activity was in favor to conclude that the nature of the metal coordinated in the L^{N2S2} ligand has no notable impact on their performance and that the bipyridine unit is the key factor in controlling their reactivity.

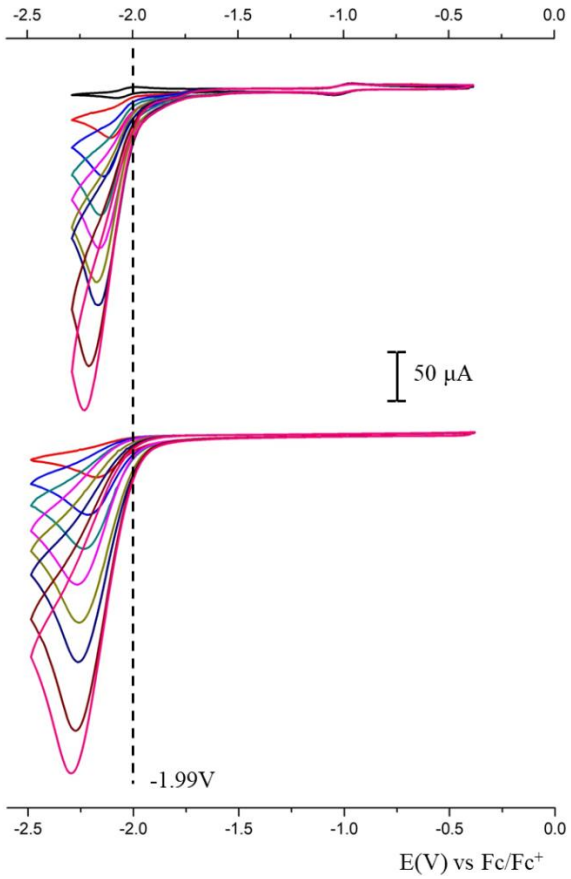

Figure 2.9 CVs of $Co^{II}Fe^{II}Cp$ (0.73 mM, top, black) in the absence or presence of various amounts of Et_3NH^+ in DMF solution, 0.1 M n-Bu_4NClO_4, on a glassy carbon electrode at 100 mV/s^{-1}. 5 equiv.(red); 10 equiv. (blue); 15 equiv. (cyan); 20 equiv. (pink); 25 equiv. (dark yellow); 30 equiv. (dark blue); 40 equiv. (deep red); 50 equiv. (magenta). The CVs of the corresponding blank samples (no catalyst) are also shown (bottom).

2.3 Conclusions

The target $Co^{II}Fe^{II}Cp$ complex has been synthesized and characterized by IR, ESI-MS and UV-vis spectra. The corresponding one-electron reduced species ($Co^{I}Fe^{II}Cp$) has been isolated and characterized. The redox properties of $Co^{II}Fe^{II}Cp$ have been investigated in DMF. $Co^{II}Fe^{II}Cp$ has a more positive reduction potential upon first one electron reduction, indicating that it is the easiest to reduce with respect to the two other MFe analogues (M = Ni and Fe). Unexpectedly, this Co-based complex is not active to electrocatalytically produce H_2. Because the analogous $Ni^{II}Fe^{II}Cp$ and $Fe^{II}Fe^{II}Cp$ complexes have the ability to catalyze the H_2 production in MeCN, we can hypothesize that the change in electrocatalytic conditions, the nature of the solvent (MeCN vs DMF), may limit the catalytic ability of $Co^{II}Fe^{II}Cp$ complex for H_2 production. DFT calculations are currently performed to explain this difference of reactivity.

Chapter 3 Modulation of the electrocatalytic activity for H_2 production with bio-inspired MFe (M = Ni and Co) complexes

3.1 Introduction

Hydrogen (H_2), as an energy carrier, is considered a promising alternative to fossil fuels to alleviate the pressure of energy shortages.[4] Most of H_2 production is currently supplied by fossil fuels, including natural gas, oil, and coal (non-renewable resources). Currently, water splitting is of interest as an appealing approach to produce high-purity H_2, owing to its clean and sustainable process. So far, precious-metal Pt-based materials display the most efficient catalytic activity for H_2 production, but their large-scale applications are unfortunately limited by the high price and scarcity.[118] Designing a non-noble metal-free catalytic system thus is needed under the premise of ensuring catalytic activity.

Nature provides sources of inspiration to design molecular electrocatalysts, i.e. the NiFe and FeFe H_2ases that catalyze reversibly the oxidation of dihydrogen from protons and electrons close to the thermodynamic potential (**Figure 1.1**),.[8] It has been proposed that proton-coupled electron transfer steps are involved during their catalytic cycle. For the proton transfer step, the sulfur from the Ni-bound cysteine residue in the NiFe H_2ase serves as a proton relay thanks to its hemilabile character when protonated.[119] In the case of the FeFe H_2ase, the pendant amine from the bridging azadithiolate ligand, in close vicinity to the diiron site, acts as a proton relay.[13] This pendant amine is considered to facilitate a low energetic pathway for the heterolytic formation of dihydrogen in the FeFe models as proposed based on DFT calculations.[120] Numerous works have confirmed that the proton relay is important for promoting the electrocatalytic activity, for example by lowering the overpotential in the case of H_2 production.[42, 44, 45] Most of currently synthesized bio-inspired bimetallic complexes bearing pendant amine are FeFe complexes, while NiFe models are still rare. This thus remains a challenge for the synthesis of NiFe complexes with a potential proton relay as a pendant amine group.

Recently, a series of complexes $M^{II}Fe^{II}Cp$ (M=Ni, Fe and Co) and $Ni^{II}Fe^{II}Cp^*$ have been designed and investigated based on the structural features and functions of the active sites of the NiFe and FeFe H_2ases (**Figure 1.26 and 2.1**). Both NiFe mimics either with Cp or Cp* for H_2 production display redox behaviors mainly centered on both the Ni site and the L^{N2S2} ligand. Their similar HER activity highlights the importance of the redox-active bipyridine ligand in MeCN in the presence of Et_3NH^+ (pK_a^{MeCN} = 18.6). Compared with the NiFe complexes, the $Fe^{II}Fe^{II}Cp$ parent also shows

similar catalytic performance under similar conditions, demonstrating that the efficiency of these systems seems to be more linked to the presence of the L^{N2S2} ligand instead of the metal. This further emphasizes that the redox-active bipyridine unit is one key factor in controlling their activity. In such context, it was completely unexpected, that no catalytic behavior is observed in DMF with $Co^{II}Fe^{II}Cp$.

Interestingly, the complexes $Ni^{II}Fe^{II}Cp$ and $Fe^{II}Fe^{II}Cp$ have been shown to display HER activity in acidic aqueous solutions after their physical adsorption onto carbon based electrodes[35, 36] ($[4]^+$: TON = 4.9(0.1)*10^5 in 9 hours, TOF = 15.3(0.3) s^{-1}, at -0.80 V vs SHE, pH 4; $[5]^+$: TON = 7.2*10^6 in 10 hours, TOF = 200 s^{-1}, at -0.85 V vs SHE, pH 3).

Based on the above discussion and in order to promote the electrocatalytic activity for H_2 production, our objective was to introduce an amine group into the MFe complexes to develop a new family of bio-inspired heterodinuclear electrocatalysts. We decided to focus on the Fe site by modifying the Cp ligand. We thus have replaced the Fe-bound cyclopentadienyl (Cp) by the picolyl cyclopentadienyl (PyCp) or the 2-(diethylamino)ethyl-cyclopentadienide (CpN) with the nickel site keeping unchanged (**Figure 3.1**).

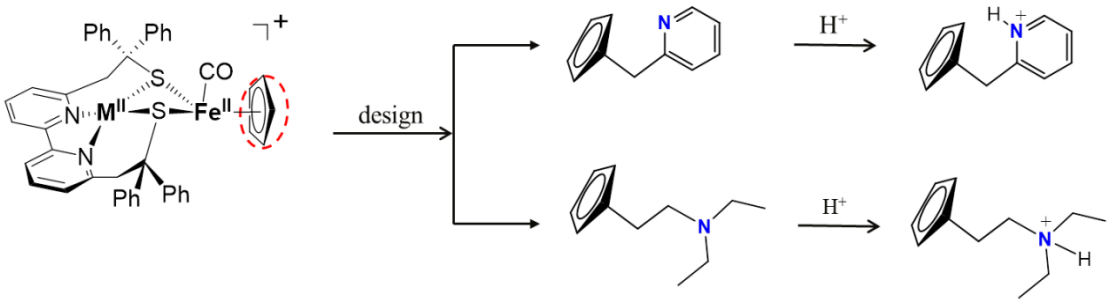

Figure 3.1 Ligand design at the Fe-Cp site.

3.2 Result and discussion

3.2.1 Synthesis and characterization of $[L^{N2S2}NiFe(CO)CpPy]BF_4$

In order to synthesize $[L^{N2S2}NiFe(CO)CpPy]BF_4$ (NiFeCpPy), the $[PyCpFe(CO)(MeCN)_2]BF_4$ (FeCpPy) complex should be synthesized first. The synthetic route of the FeCpPy complex is shown in **Figure 3.2**. The synthesis of the designed ligand starts with the deprotonation of the 2-picolyl chloride hydrochloride (1a) to yield the 2-picolyl chloride (1b, PyCl).[121] Then PyCl reacts with sodium cyclopentadienide to produce the (2-picolyl)-cyclopentadiene (1c).[121] After the addition of $Fe(CO)_5$, the resulting dinuclear Fe complex (1d) with four CO ligands is obtained. It is then oxidized with I_2 leading to a mononuclear Fe species (1e).[122] After removing the iodide ligand with $AgBF_4$, the mononuclear $[PyCpFe(CO)_2(THF)]BF_4$ (1f) complex is obtained. Finally, one CO ligand is removed from 1f to generate the FeCpPy (1g) complex. It should be noted that, for this last step, we developed

another protocol for the removal of the CO that uses the Me_3NO reagent, well-known to remove CO ligand from transition metal ion complexes. This process is faster and more quantitative compared to the photo-dissociation process which is slow and provides moderate yield.

All the complexes have been characterized by IR and ESI-MS techniques. For 1f, two CO vibrations are observed at 2066 cm^{-1} and 2021 cm^{-1} in the IR spectra recorded in MeCN, assigned to two terminally bound CO (**Figure 3.3**, pink line). After adding Me_3NO into a solution of 1f, there is only one CO vibration at 1993 cm^{-1} after 10 min of reaction (**Figure 3.3**, black line). However, no IR feature is any longer observed in the expected range for CO vibrations after about 3 h in the IR spectrum of a MeCN solution of FeCpPy, evidencing a loss of both CO ligands. Therefore, the FeCpPy complex needs to be used as soon as possible after its preparation.

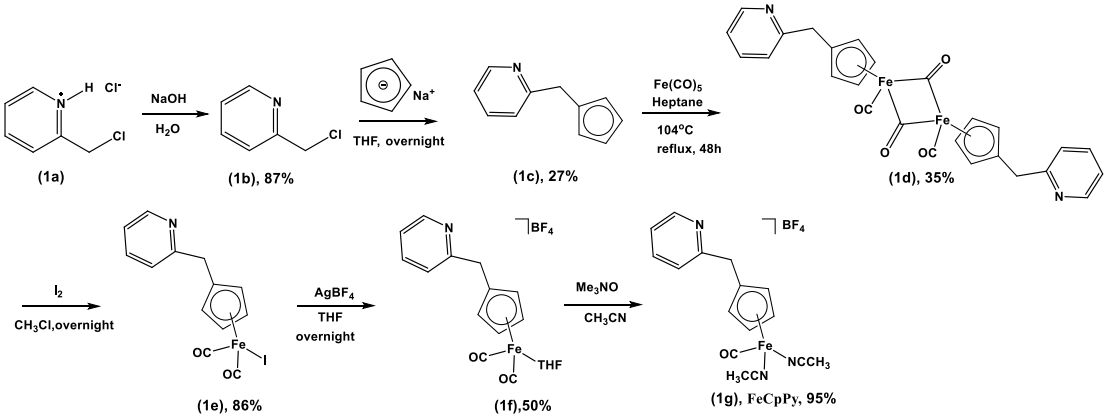

Figure 3.2 Synthetic route for the FeCpPy complex.

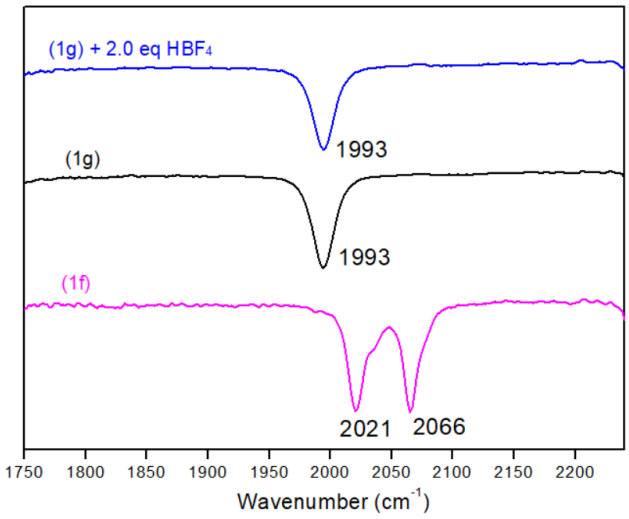

Figure 3.3 IR spectra of the (1f) (0.35 mM, pink line), (1g) (black line) and (1g) + 2.0 eq HBF_4 (blue line).

Next, a stoichiometric amount of NiL has been added to a solution of FeCpPy in distilled CH_2Cl_2 at room temperature to synthesize the NiFeCpPy complex (**Figure 3.4**). Unfortunately, the resulting solution displays no IR feature in the expected range for

CO vibrations, suggesting that the last CO ligand is released during the reaction. The possible reason is that the N atom of the pendant pyridine is more easily coordinated to the Fe ion under these conditions than the CO ligand, leading to the release of the CO ligand (**Figure 3.4**).[123] In the catalytic state of the [FeFe] H_2ase, the μ-CO bridging geometry induces minimal structural rearrangement of the active site throughout the catalytic process to achieve fast and efficient catalysis.[58] For the intermediate states of $Ni^{II}Fe^{II}Cp$, the CO vibration frequencies (energy) are fine-tuned to support the whole catalytic cycle of HER as demonstrated by DFT.[54, 124] Therefore, the CO ligand in bio-inspired models is a critical component of the catalysts for H_2 production.

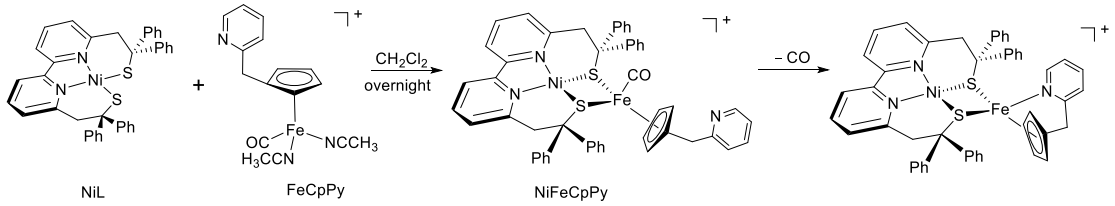

Figure 3.4 Synthesis of the NiFeCpPy complex.

In order to prevent the release of the CO ligand, the amine of FeCpPy has been protonated first before reacting with NiL (**Figure 3.5**). The strong acid HBF_4•Et_2O has been selected to protonate the pyridine moiety. After the addition of 1.0 equivalent (eq) of HBF_4•Et_2O to a MeCN solution of (1g) (**Figure 3.5**), no change is observed in either its IR or UV-vis spectra. We thus conclude that FeCpPy cannot be protonated under such conditions. Then, 2.0 eq of HBF_4•Et_2O is added to the MeCN solution of FeCpPy (1g). In the corresponding UV-vis spectrum, the growth of two transitions at 313 nm and 350 nm is observed (**Figure 3.6**). However, no change is observed in the IR spectrum, and the CO vibration is still observed at 1993 cm^{-1} (**Figure 3.3**, blue line). The possible reason is that the protonation site is too far to impact the CO vibration. Therefore, we conclude that the protonation of FeCpPy occurs on the N atom of the pyridine to yield the FeCpPyH complex.

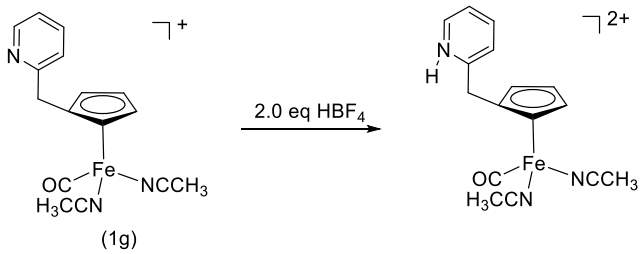

Figure 3.5 Synthesis of the FeCpPyH complex.

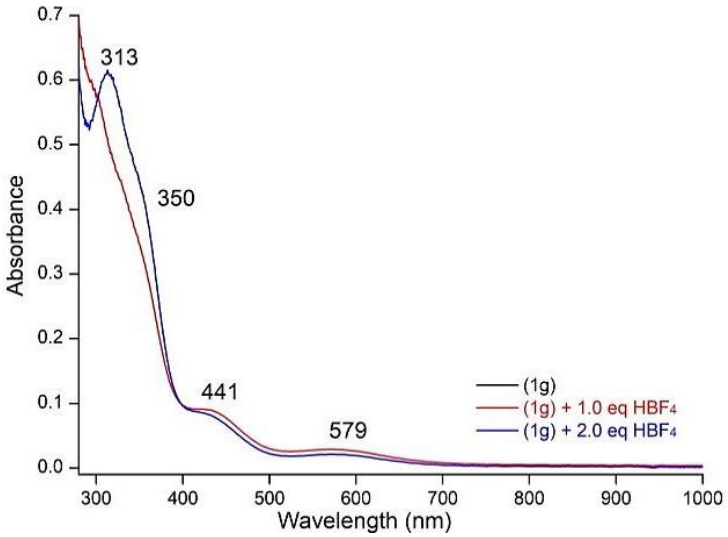

Figure 3.6 UV-vis spectra of (1g) (0.15 mM, l (cuvette) = 1 cm), black line), (1g) + 1.0 eq HBF_4 (red line) and (1g) + 2.0 eq HBF_4 (blue line).

NiL is then added to a CH_2Cl_2 solution of FeCpPyH to synthesize the corresponding NiFe complex (**Figure 3.7**). The UV-vis spectrum of the reaction solution displays two main transitions at 501 nm and 560 nm originating from the NiL complex (**Figure 3.8**). After overnight, these two transitions disappeared, and three new transitions appear at 391 nm, 497 nm, and 660 nm. The IR spectrum recorded in CH_2Cl_2 after the overnight shows that the CO vibration at 1999 cm^{-1} has been shifted to 1922 cm^{-1}, indicating the formation of a new complex. In the ESI-MS spectrum of the crude reaction solution, a peak at m/z = 876.19 is present, assigned to the expected $[L^{N2S2}NiFeCpPy(CO)]^+$ complex. Based on the above characterization, we concluded that $[L^{N2S2}NiFeCpPyH(CO)]^+$ is present in the solution. After the reaction work-up, pentane is added into the reaction solution to precipitate the NiFeCpPy complex. Unfortunately, the resulting solid displays no IR feature in the expected range for CO vibrations, suggesting that CO is released again in the resulting product (**Figure 3.7**). The possible reason is that, during the process of precipitation, the pyridine is deprotonated allowing pyridine to coordinate at the Fe site, followed by the release of the CO ligand.

To synthesize the heterodinuclear complex bearing an amine group with CO ligands, we thus decided to use another potential proton relay such as a tertiary amine, more precisely the 2-(diethylamino)ethyl-cyclopentadienide (CpN). Indeed, tertiary amines are more basic than the pyridine. It is thus expected that they are less prone to coordinate to the Fe ion allowing us to obtain the targeted NiFe complex with one CO ligand.

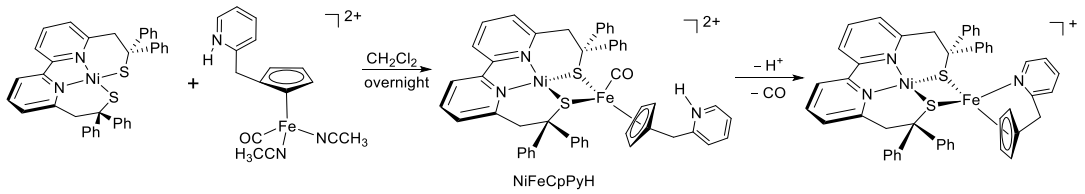

Figure 3.7 Synthetic route of NiFeCpPyH.

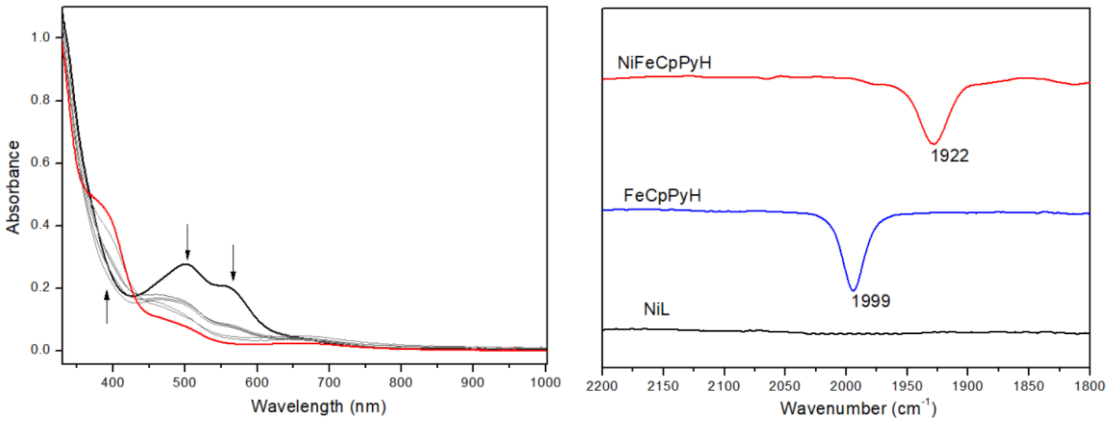

Figure 3.8 UV-vis spectra (left) of the reaction between FeCpPyH and NiL (0.12 mM, l (cuvette) = 1 cm, black: 0 h, red: after overnight). IR spectra (right) of the NiL (black line), FeCpPyH (blue line) and NiFeCpPyH (red line) complexes in CH_2Cl_2.

3.2.2 Synthesis and characterization of $[L^{N2S2}NiFe(CO)CpN]BF_4$

The synthetic route of the $[Fe(CO)_2(MeCN)CpN]BF_4$ (2f) complex is shown in **Figure 3.9**. Firstly, the 2-(diethylamino)ethyl chloride hydrochloride (2a) reacts with 2.0 eq of sodium cyclopentadienide to yield the 2-(diethylamino)ethyl-cyclopentadienide (CpN, 2b).[125] Then, $Fe(CO)_5$ is added to a heptane solution of (2b) to obtain the dinuclear Fe complex (2c) with four CO ligands. It is then oxidized with I_2 to produce the mononuclear Fe-I species (2d). After the removal of the iodide ligand with $AgBF_4$ in MeCN, the mononuclear Fe-MeCN derivative (2e) is isolated. Finally, one CO ligand is removed from (2e) using Me_3NO, to yield FeCpN (2f). All the complexes have been characterized by the IR and ESI-MS methods. For (2e), two CO vibrations are observed at 2035 cm^{-1} and 2079 cm^{-1} in the IR spectrum recorded in MeCN. They have been assigned to two terminally bound CO. In the ESI-MS spectrum of the reaction solution, the observed peak at m/z = 317.09 has been assigned to the expected $[Fe(CO)_2(MeCN)CpN]^+$ complex in CH_2Cl_2. For the FeCpN complex, one CO vibration is observed at 1980 cm^{-1} in MeCN. In CH_2Cl_2, it is slightly shifted to 1984 cm^{-1} (**Figure 3.11**). After about 6 h, the IR spectrum of the FeCpN complex displays no IR feature in the expected range for CO vibrations, evidencing a loss of the remaining CO ligand. Therefore, it is better to use the FeCpN complex as soon as possible for the next step.

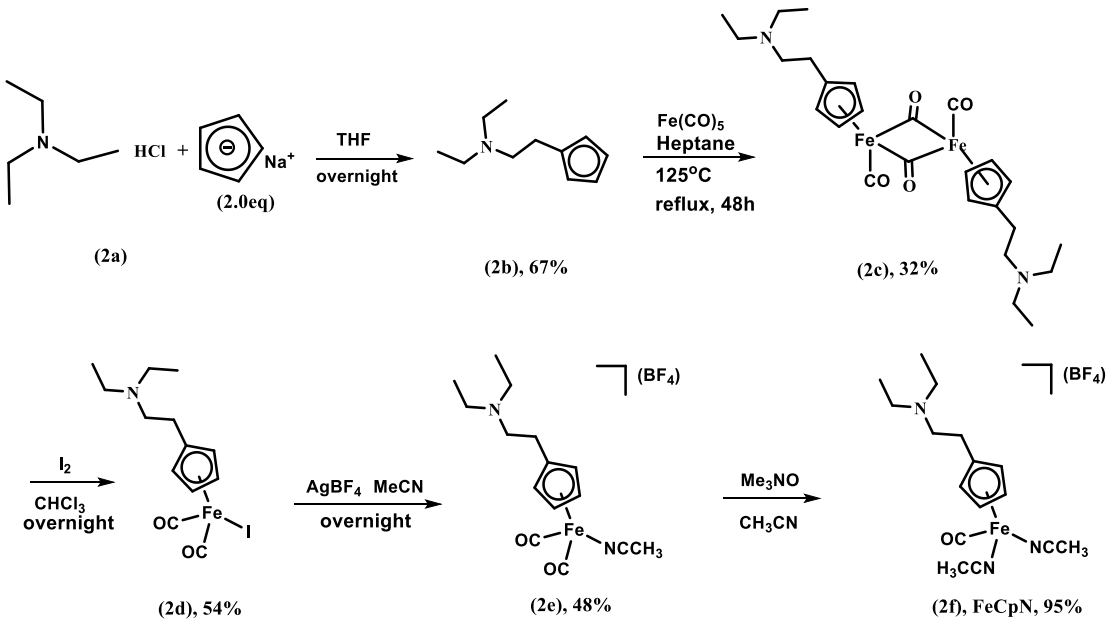

Figure 3.9 Synthetic route for the FeCpN complex.

The $[L^{N2S2}NiFe(CO)CpN]BF_4$ complex (NiFeCpN) is obtained as a brown powder from the reaction between a stoichiometric amount of NiL and FeCpN in distilled CH_2Cl_2 with 66% yield at room temperature under argon (**Figure 3.10**). In the ESI-MS spectrum of the crude reaction solution, a peak at m/z = 884.31 is observed, assigned to the expected $[NiFe(CO)CpN]^+$ complex. Pentane is added to the reaction solution to precipitate the NiFeCpN complex. In the IR spectrum, the CO vibration is observed at 1928 cm^{-1} in CH_2Cl_2 (**Figure 3.11**), while it is shifted to 1920 cm^{-1} in the solid state. This CO vibration has the same energy with respect to the terminal Fe-CO vibration found in solid-state IR spectra of $Ni^{II}Fe^{II}Cp$ (1926 cm^{-1}) and $Ni^{II}Fe^{II}Cp^*$(1929 cm^{-1}) indicating a similar environment of the Fe^{II} ion in the three complexes. The energy is higher than the bridged M-CO-M vibration present in the $Fe^{II}Fe^{II}Cp$ (1822 cm^{-1}) and $Co^{II}Fe^{II}Cp$ (1856 cm^{-1}) complexes. Based on these data, it can be concluded that the CO ligand is terminally bound to Fe ion in NiFeCpN.

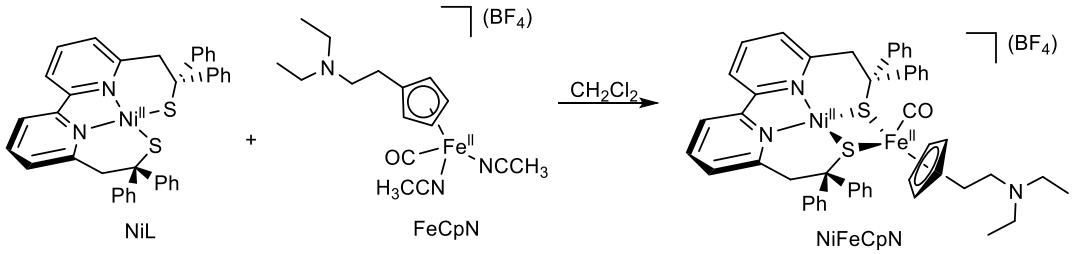

Figure 3.10 Synthesis of the NiFeCpN complex.

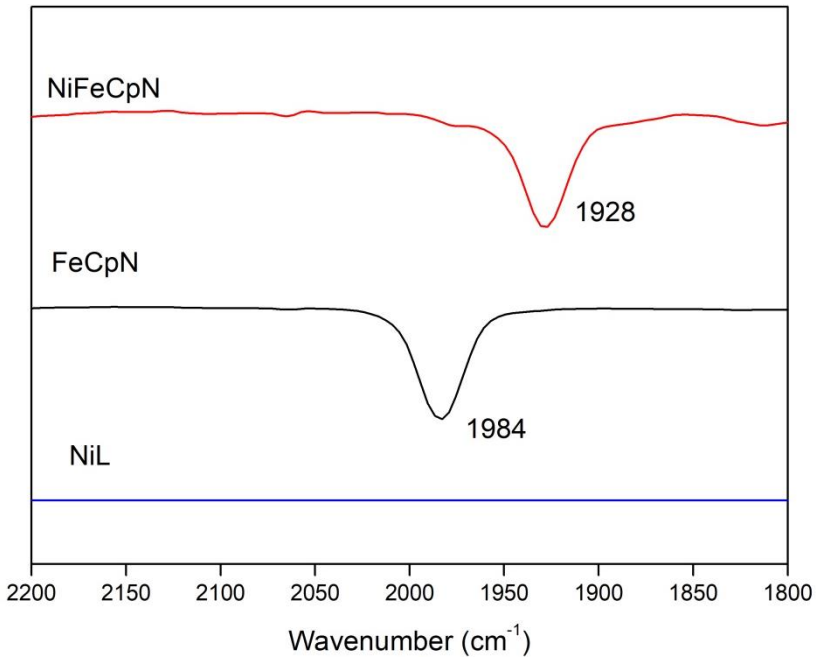

Figure 3.11 IR spectra of the FeCpN (black line) NiFeCpN (red line) and NiL (blue line) complexes recorded in CH_2Cl_2.

3.2.3 Redox properties of NiFeCpN

In order to explore the redox properties of NiFeCpN complex in CH_3CN, its stability is first evaluated. Its IR and UV-vis spectra indicate that NiFeCpN is stable in the MeCN for at least 16 h (**Figure 3.12**). The cyclic voltammetry (CV) is then recorded in MeCN.

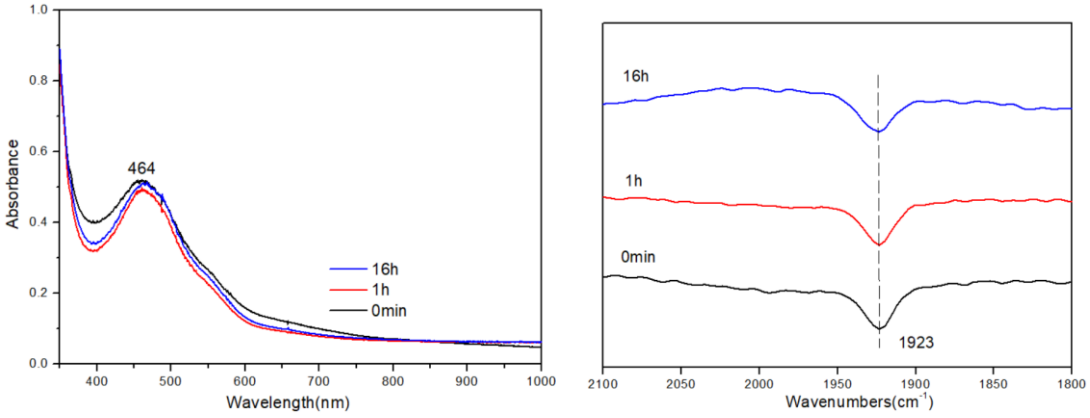

Figure 3.12 UV-vis (right) and IR (left) spectra of NiFeCpN (1.01 mM for UV-vis, l (cuvette) = 1 cm, 0.34 mM for IR) in MeCN on different timescale (black line: 0 min; red line: 1 h; blue line: 16 h).

The cyclic voltammogram (CV) of NiFeCpN recorded in MeCN displays three reduction waves at −1.35 V, −1.60 V, and −1.86 V vs $Fc^{+/0}$ (**Figure 3.13**). The first reduction of NiFeCpN (E_{pc} = −1.35 V) is associated with an oxidation peak at E_{pa} = −0.52 V, the second one at E_{pc} = −1.60 V with an oxidation peak at E_{pa} = −1.29 V, and the reduction wave at E_{pc} = −1.86 V with the third oxidation peak at E_{pa} = −1.77 V.

For the parent $Ni^{II}Fe^{II}Cp$ complex,[33] the CV displays two reversible and diffusion-controlled one-electron reduction waves at $E_{1/2}$ = −1.29 V and −1.90 V vs $Fc^{+/0}$ in MeCN. These two reduction waves have been assigned to the successive reductions of Ni^{II} to Ni^{I} and of the bipyridine moiety in $(L^{N2S2})^{2-}$. The reduction of the Ni^{II} ion into Ni^{I} in $Ni^{II}Fe^{II}Cp$ occurs at a significantly more positive potential than in the mononuclear NiL complex under the same conditions ($E_{1/2}$ = −1.82 V corresponding to a potential shift of 530 mV). Regarding the diiron analog $Fe^{II}Fe^{II}Cp$,[32] the CV exhibits two diffusion-controlled reversible one-electron reduction waves at $E_{1/2}$ = –1.21 V and $E_{1/2}$ = –1.65 V vs $Fc^{+/0}$, which is assigned to the reduction of $Fe^{II}Fe^{II}$ core into the mixed-valent $Fe^{1.5}Fe^{1.5}$ species and the reduction of bipyridine moiety of the L^{N2S2} ligand, respectively. For the analog $Ni^{II}Fe^{II}Cp^*$,[34] the CV displays two one-electron-reduction processes under similar conditions. An irreversible reduction wave at E_{pc} = −1.46 V is associated with an oxidation peak at E_{pa} = −1.04 V. According to experiments and theory calculations, this reduction wave has been assigned to Ni^{II} to Ni^{I} redox process. The oxidation wave at E_{pa} = −1.04 V has been assigned to the oxidation of the reduced form of the mononuclear $[Cp^*Fe^{II}(CO)(MeCN)_2]^+$ fragment, evidencing the breaking of the heterodinuclear complex into the mononuclear $[Cp^*Fe^{II}(CO)(MeCN)_2]^+$ and NiL complexes. Consistently, the reversible reduction process at $E_{1/2}$ = −1.83 V (ΔE_p = 60 mV) occurs at the bipyridine moiety of the mononuclear NiL. For the Co analogue $Co^{II}Fe^{II}Cp$**,** the CV reveals two diffused-controlled (quasi-)reversible one-electron processes, centered at $E_{1/2}$ = –1.00 V and $E_{1/2}$ = –2.04 V in DMF solution. The redox system at –1.00 V is attributed to the $Co^{II/I}$ reduction, and the second one to the reduction of the bipyridine ligand. The important data have been summarized in **Table 3.1**.

Table 3.1 The redox and catalytic properties potential of the $M^{II}Fe^{II}$ complexes measured in MeCN.

Complexes	E (V) vs $Fc^{+/0}$					
	E_{pc1}	E_{pc2}	E_{pc3}	E_{pc4}	$E_{cat/2}$	η
$Fe^{II}Fe^{II}Cp$	−1.21	−1.65	\	\	−1.90	0.73
$Ni^{II}Fe^{II}Cp$	−1.29	−1.90	\	\	−1.85	0.68
$Ni^{II}Fe^{II}Cp^*$	−1.46	−1.83	\	\	−1.86	0.69
$Co^{II}Fe^{II}Cp$	−1.00[a]	−2.04[a]	\	\	No activity	\
NiFeCpN	−1.35	−1.60	−1.86	\	−1.73	0.59
CoFeCpNH	−0.95	−1.62	−1.83	−2.03	−1.83	0.69

[a] in DMF.

By comparing the redox properties of the MFe (M= Ni, Fe and Co) analogs, the redox process of NiFeCpN complex has been assigned as follows. It is proposed that the reduction of NiFeCpN at E_{pc} = –1.35 V corresponds to the reduction of Ni^{II} to Ni^{I}, with a positive shift by 110 mV relative to $Ni^{II}Fe^{II}Cp^*$. The oxidation wave at E_{pa} = –0.52 V is

assigned to the oxidation of the reduced form of the mononuclear FeCpN fragment. In order to verify this hypothesis, the CV of FeCpN has been recorded in MeCN (**Figure 3.13**, right). In the cathodic direction, it displays an irreversible wave at E_{pc} = –1.72 V, which is associated with an oxidation wave at E_{pa}= –0.51 V. In addition, in the anodic direction, the CVs of the NiFeCpN and FeCpN exhibit no wave at around –0.5 V. These data confirm that the oxidation wave at E_{pa} = –0.52 V corresponds to the oxidation of the reduced form of the mononuclear FeCpN. The observation of the presence of the mononuclear FeCpN in the solution evidences that the heterodinuclear is decomposed into two mononuclear complexes after its one electron reduction. Accordingly, the reduction wave at E_{pc} = −1.86 V corresponds to the reduction of the bipyridine moiety in the mononuclear NiL.

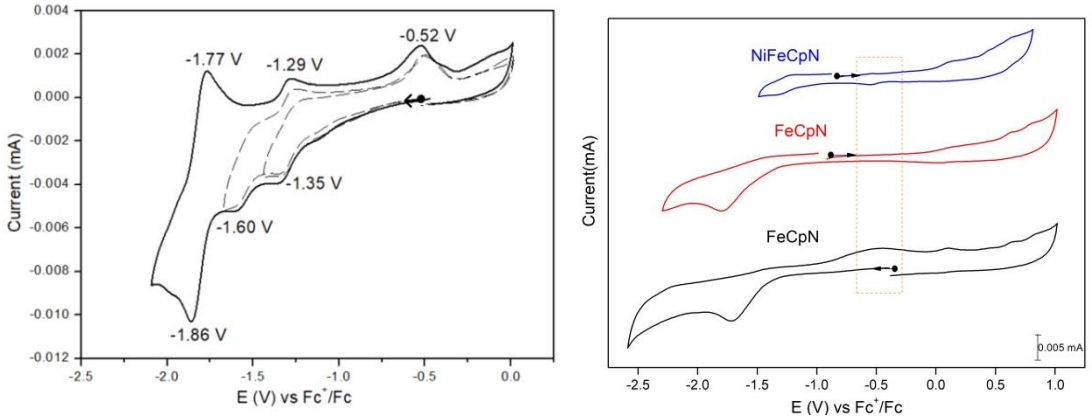

Figure 3.13 CVs (left) of a solution of NiFeCpN (0.42 mM) and (right) of solution of NiFeCpN (0.31 mM, blue line) and FeCpN (0.68 mM, red line and black line). Conditions: 0.1 M n-Bu_4NClO_4/MeCN, on a glassy carbon electrode at scan rate (v) = 100 mV/s.

Regarding the redox system at around −1.60 V, none has been observed in the MFe analogs. Therefore we could consider that the amino group can be protonated, at least partially, after the one-electron reduction of the complex by traces of water. That is, the reduction wave at E_{pc} = −1.60 V corresponds to the reduction of the reduced protonated form of NiFeCpN, {$LNi^{I}Fe^{II}NH$ or $LNi^{III}(H^{hyd})Fe^{II}N$} (**Figure 3.14**). In order to verify this hypothesis, 1eq and 2eq of Et_3N as a base source have been added to an electrolyte solution of NiFeCpN to prevent this protonation step. The CVs show the disappearance of the reduction wave at E_{pc} = −1.60 V (**Figure 3.15**) confirming our hypothesis. Consistently, upon the addition of 0.5 eq Et_3NH^+, an increase of the current is observed below −1.50 V, indicating the occurrence of a catalytic proton reduction event (see above for the rationalization of this wave). Additionally, in the case of the $Fe_2(adt)(CO)_{6-x}(L)_x$ complexes bearing a pendant amine, additional reduction processes have been also observed attributed to their N-protonation.[29, 126-128]

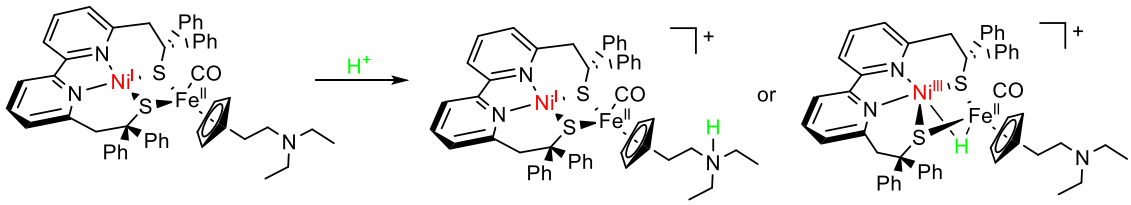

Figure 3.14 Protonation of the reduced NiFeCpN complex.

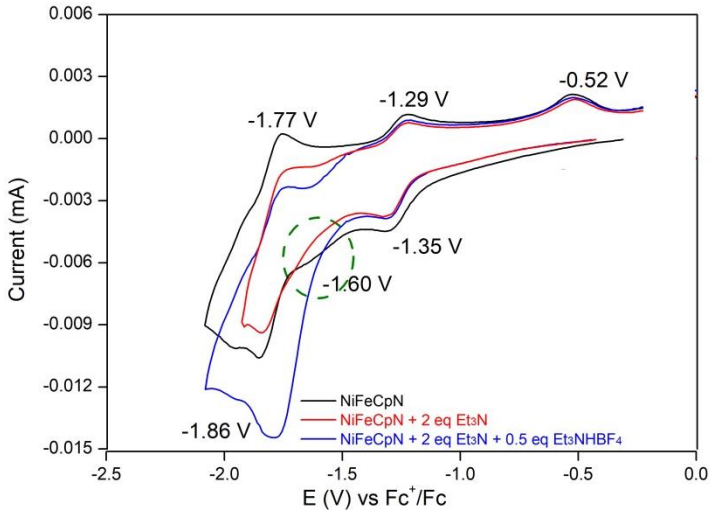

Figure 3.15 CVs of 0.31 mM of NiFeCpN (black line) with 2 eq Et_3N (red line) and 2 eq Et_3N + 0.5 eq Et_3NH^+ (blue line) in 0.1 M n-Bu_4NClO_4/MeCN, on a glassy carbon electrode at *v* = 100 mV/s.

3.2.4 Homogeneous catalytic activity of NiFeCpN for H_2 production

The electrocatalytic activity for H_2 production of NiFeCpN has been evaluated in the presence of Et_3NH^+ (pK_a^{MeCN}= 18.6) as a proton source. The catalytic potential for Et_3NH^+ is observed at about −1.87 V vs $Fc^{+/0}$ in the absence of NiFeCpN, a more negative potential than that in the presence of NiFeCpN, indicating the catalytic role of the complex (**Figure 3.16**, black line). For the mononuclear FeCpN complex, the observed catalytic current intensity is lower than that of NiFeCpN, demonstrating a better activity for the heterodinuclear complex (**Figure 3.16**, blue line).

In the presence of Et_3NH^+ and NiFeCpN, a catalytic process is observed at $E_{cat/2}$ = −1.73 V vs $Fc^{+/0}$ (measured at the half-wave) (**Figure 3.16 and 3.17**). The overpotential is calculated to be of 0.59 V according to the following equation (overpotential, η= $|E_{cat} - E^o_{HA}|$, E^o_{HA}= −1.14 vs $Fc^{+/0}$).[129] The current intensity of the catalytic wave continuously increases by increasing the amount of Et_3NH^+ (**Figure 3.17**, left). The plots of the catalytic current intensity versus the concentration of the addition of Et_3NH^+ give a linear correlation, indicating a diffusion-controlled regime for catalysis under these conditions (**Figure 3.17**, right).[32] Compared with $Ni^{II}Fe^{II}Cp$

($E_{cat/2}$= −1.85 V vs $Fc^{+/0}$, η = 0.68 V), $Ni^{II}Fe^{II}Cp^*$($E_{cat/2}$= −1.86 V vs $Fc^{+/0}$, η = 0.69V), $Fe^{II}Fe^{II}Cp$ ($E_{cat/2}$= −1.90 V vs $Fc^{+/0}$, η = 0.73 V) and $Co^{II}Fe^{II}Cp$ (no activity for H_2 production), $Ni^{II}Fe^{II}$CpN displays the more positive catalytic potential with a positive shift of about 130 mV and a lower overpotential (**Table 3.1**). This performance confirms that the presence of the pendant amine notably enhances the activity, i.e. by lowering overpotential. Such impact has been already reported in the literature. For example, the complex [9] (η = 0.64 V) that contains a pendant amine has a lower overpotential under similar conditions than the complex [2] (η = 1.06 V), which does not contain a potential proton relay, (**see section 1.1.3.1**).

The NiFeCpN complex has a much lower overpotential (0.59 V), compared to the analogs [($^{alkyl}N_2S_2$)NiFeCp*(CO)]$^+$ (η = 1.31 V) and [18]$^+$ (η = 0.942 V, **see 1.1.3.3 section**) that do not contain a pendant amine.[130] NiFeCpN also displays a lower overpotential with respect to the complex [14]$^+$ (η = 0.78 V), and a slightly higher one with respect to the complex [13]$^+$ (η = 0.54 V) (**see 1.1.3.3 section**). This further demonstrates that the strategy of adding a potential relay is positive on the reactivity of the HER electrocatalysts.

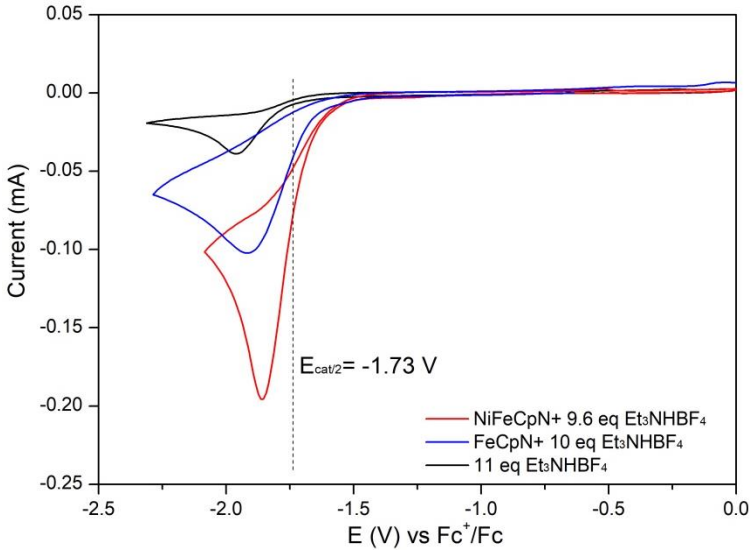

Figure 3.16 CVs of NiFeCpN (0.42 mM) + 9.6 eq Et_3NH^+ (red line), FeCpN (0.68 mM) + 10 eq Et_3NH^+ (blue line) and Et_3NH^+ (4.62 mM, black line) under similar conditions. Conditions: electrolyte: 0.1 M n-Bu_4NClO_4/MeCN, on a glassy carbon electrode at *v* = 100 mV/s.

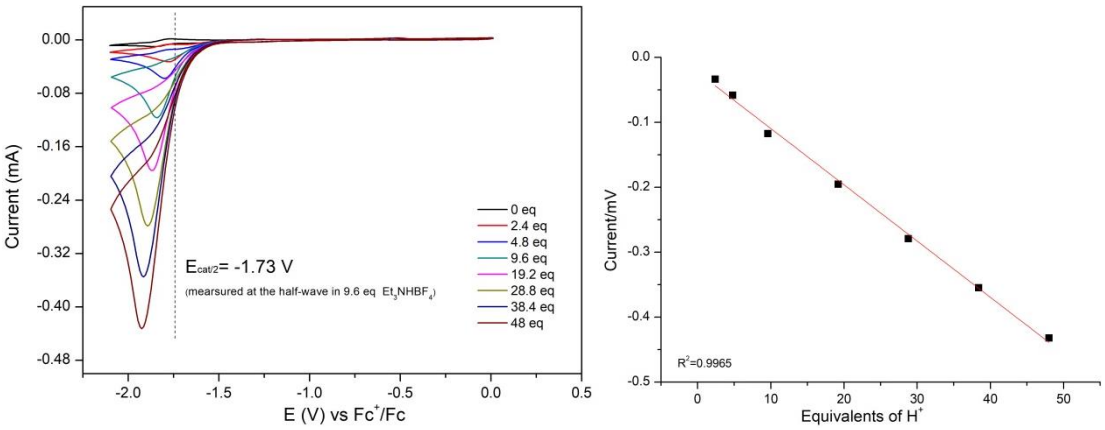

Figure 3.17 CVs (left) of NiFeCpN (0.42 mM) with various amounts of Et_3NH^+. The plots of the i_{cat} versus the concentration of the addition of Et_3NH^+ for a solution of 0.42 mM NiFeCpN (right). Conditions: electrolyte: 0.1 M n-Bu_4NClO_4/MeCN, on a glassy carbon electrode at *v* = 100 mV/s.

3.2.5 Mechanistic investigations for H_2 production with NiFeCpN

As described in the above experiments, we have demonstrated that NiFeCpN can catalyze H_2 production by adding acid, Et_3NH^+ as the proton source (**Figure 3.17 and Figure 3.18**). After the addition of acid, a shift of potential at E_{pc}= −1.35 V vs $Fc^{+/0}$, assigned to the reduction of Ni^{II} to Ni^{I}, is observed toward anodic potential (**Figure 3.18**). Moreover, no modifications in the shape and intensity of the wave at E_{pc}= −1.35 V is observed. This observation evidences a coupled chemical reaction, here a protonation, consistently with the observation of the reduction wave at E_{pc} = −1.60 V in the CV of the complex (**Figure 3.15**).[131]

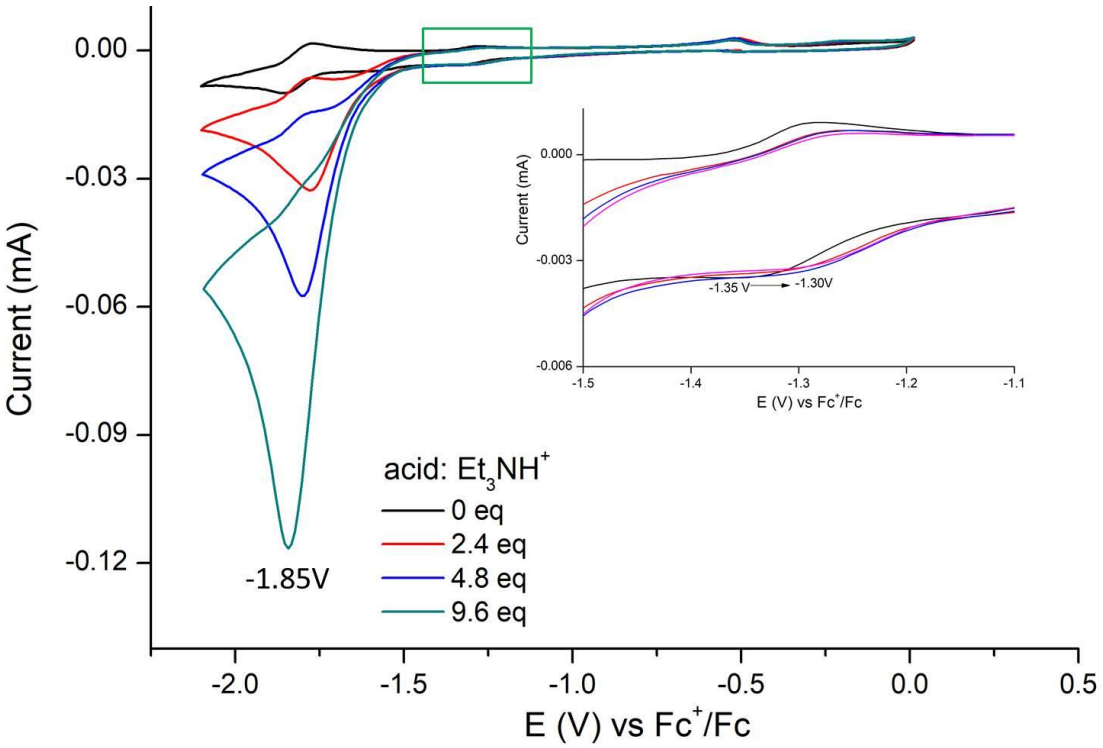

Figure 3.18 CVs of 0.42 mM NiFeCpN in the absence (blank line) or in the presence of Et_3NH^+: 2.4 eq (red line), 4.8 eq (blue line), and 9.6 eq (pink line). The bottom figure is a zoomed-in view in the green box of the top figure.

A similar shift has been observed with the complex $[Co(bapbpy)Cl]^+$ (bapbpy=6,6'-bis(2-aminopyridyl)-2,2'bipyridine) which possesses a protonable amine, in the presence of Et_3NH^+ (**Figure 3.19**).[131] Based on experimental data and DFT calculations, a [ECEC] mechanism has been proposed using Et_3NH^+ as a proton source. Complex $[Co^{II}(bapbpy)Cl]^+$ is reduced to $[Co^{I}(bapbpy)Cl]$, which is then protonated at one amino group of the bapbpy ligand to form the $[Co^{I}(bapbpyH)Cl]^+$ species. The following reduction occurs at the bipyridine ligand. This reduced form $[Co^{I}(bapbpyH)^{o}Cl]$ is further protonated to form the ammonium hydride $[Co^{II}H^{hyd}(bapbpyH)Cl]^+$ species, which releases H_2 and regenerates complex $[Co^{II}(bapbpy)Cl]^+$ (**Figure 3.19**).

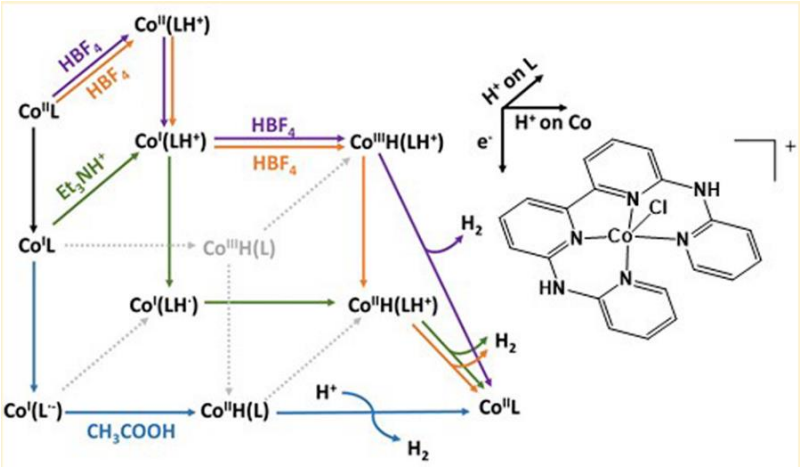

Figure 3.19 Proposed catalytic pathways followed by complex $[Co(bapbpy)Cl]^+$ for H_2 production in the presence of acids of various strengths.

In the UV-vis spectrum of a solution of NiFeCpN in an electrolyte MeCN solution, the transition at 460 nm is not changed after the addition of acid (**Figure 3.22,** left), indicating that NiFeCpN is not protonated under these conditions. Based on the experiments and reported literature,[124, 131] we thus proposed that the first catalytic steps are assigned to a one-electron reduction followed by a protonation process on the amino group to generate the $LNi^{I}Fe^{II}NH$ species that could also evolve in the hydride $LNi^{III}(H^{hyd})Fe^{II}N$ species. Based on the current experimental results, we can proposed that this protonated form is further reduced at −1.60 V and then protonated to release H_2 and regerated the $LNi^{II}Fe^{II}$ state with a [ECEC] mechanism (**Figure 3.20**). It can be concluded that $LNi^{II}Fe^{II}$ state is the entry of the catalytic cycle, not the reduced $LNi^{I}Fe^{II}$ species, which is contrarily to $Ni^{II}Fe^{II}Cp$ and $Ni^{II}Fe^{II}Cp^*$ with the reduced $Ni^{I}Fe^{II}$ being the entry of the catalytic cycle in the presence of Et_3NH^+.

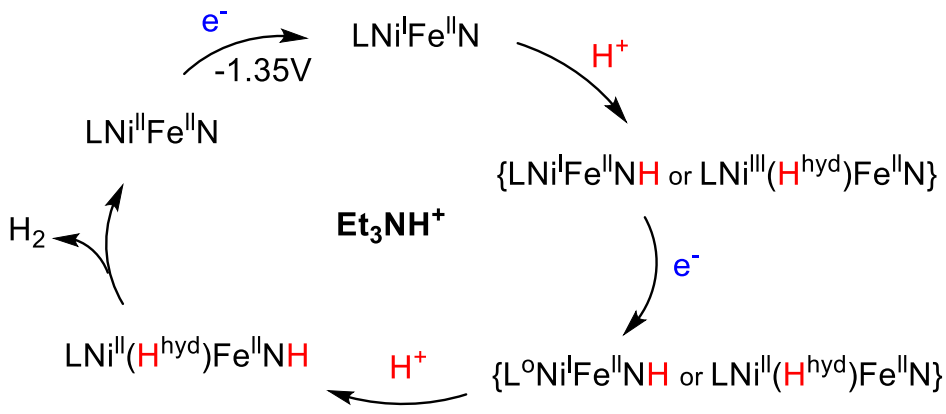

Figure 3.20 Proposed intermediate states during the catalytic cycle with the complex NiFeCpN in the presence of Et_3NH^+.

As described in **section 1.1.3**, the strength of the proton source can lead to different catalytic routes. A stronger acid, HBF_4 (pK_a^{MeCN}= 0.1), has been used as the proton source to further investigate the mechanism of NiFeCpN (**Figure 3.21**). As the acid concentration increases ($[HBF_4] \leq 4eq$), the reduction wave is shifted towards the anodic potential and lost its reversible character. An increasing current is observed at −1.60 V and −1.86 V vs $Fc^{+/0}$, indicating a few catalytic events. In the UV-vis spectrum of NiFeCpN recorded in an electrolyte MeCN solution, a slight blue shift of 9 nm and a decrease in intensity is observed after the addition of HBF_4 (**Figure 3.20,** right), indicating that NiFeCpN is protonated in the presence of HBF_4. We thus proposed that the NiFeCpN complex is first protonated on the amino group to form the $LNi^{II}Fe^{II}NH$ species, which is then reduced at −1.24 V to generate the $LNi^{I}Fe^{II}NH$ or $LNi^{III}(H^{hyd})Fe^{II}N$ species. This species further undergoes reduction and protonation processes to release H_2.

With a higher concentration of acid (> 4eq), in the UV-vis spectrum, a blue shift and a decrease in intensity are also observed after adding HBF_4 (**Figure 3.22,** right).

Therefore, we infer that this NiFe complex gradually decomposes under these catalytic conditions.

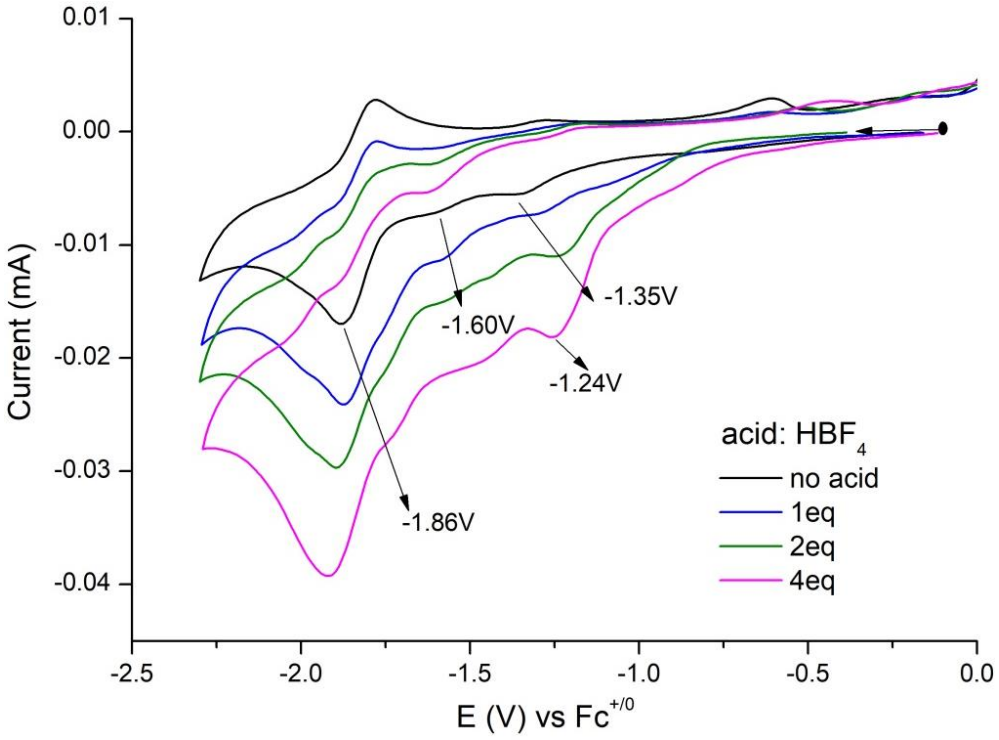

Figure 3.21 CVs of 0.45 mM of NiFeCpN in MeCN in the absence (blank line) or in the presence of HBF_4: 1 eq (blue line), 2 eq (green line) and 4 eq (pink line). Conditions: electrolyte: 0.1 M n-Bu_4NClO_4/MeCN, on a glassy carbon electrode at *v* = 100 mV/s.

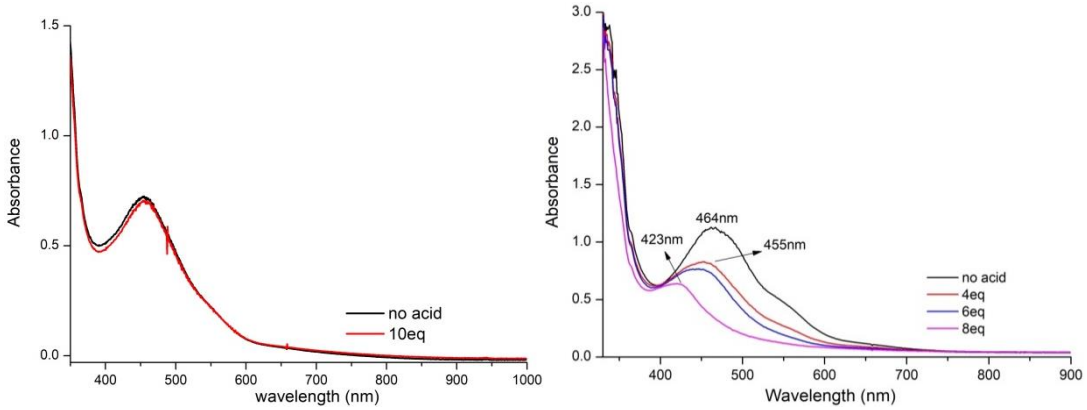

Figure 3.22 (left) UV-vis spectrum of 0.40 mM of NiFeCpN in electrolyte in the absence (blank line) or in the presence of Et_3NH^+ (10 eq, red line). (right) UV-vis spectrum of 0.45 mM of NiFeCpN in electrolyte in the absence (blank line) or in the presence of HBF_4: 4 eq (red line), 6 eq (blue line), and 8 eq (pink line). l (cuvette) = 1 cm.

For complex $[Co(bapbpy)Cl]^+$, in the presence of HBF_4, the Co^{II}/Co^{I} process becomes irreversible, and its potential shifts to more positive potentials. In addition, a new reduction process at −1.65 V vs $Fc^{+/0}$ has been observed and identified as the reduction of $Co^{III/II}$-hydride-ammonium form.[131] More precisely, $[Co^{II}(bapbpy)Cl]^+$ is

first protonated at one amino group instead of being reduced. Then the protonated species is reduced and further protonated to form the ammonium hydride $[Co^{III}(H^{hyd})(bapbpyH)Cl]^{2+}$ species. This species releases H_2 directly or undergoes further reduction to release H_2 (**Figure 3.19**).

According to the experiments and reported literature,[124, 131] we proposed that when $[HBF_4] \leq 4eq$, the $LNi^{I}Fe^{II}NH$ or $LNi^{III}(H^{hyd})Fe^{II}N$ species is first protonated and then reduced to generate $LNi^{II}(H^{hyd})Fe^{II}NH$ species. On the other hand, the $LNi^{I}Fe^{II}NH$ or $LNi^{III}(H^{hyd})Fe^{II}N$ species can be first reduced, and then protonated to yield $LNi^{II}(H^{hyd})Fe^{II}NH$. Finally, the $LNi^{II}(H^{hyd})Fe^{II}NH$ release H_2 and restore initial state $LNi^{II}Fe^{II}N$ with [CECE] or [CEEC] mechanisms (**Figure 3.23**).

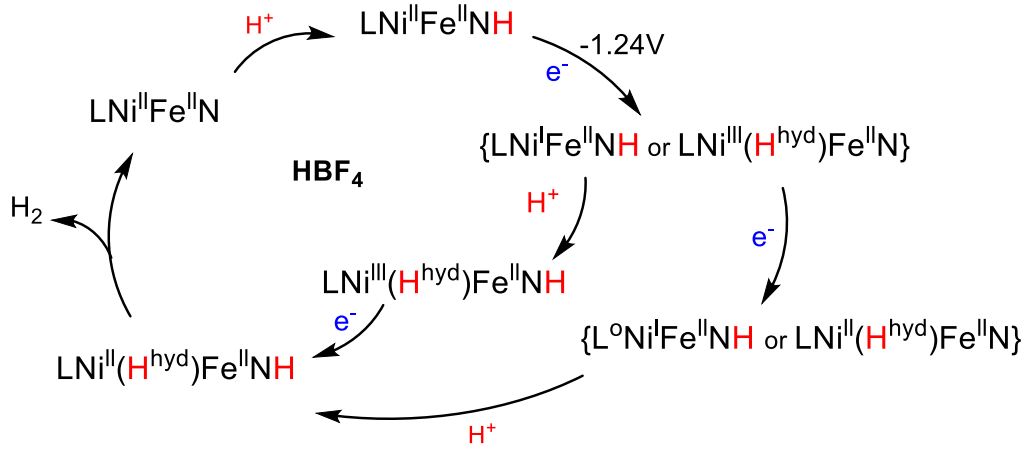

Figure 3.23 Proposed intermediate states during the catalytic cycle with the complex NiFeCpN in the presence of HBF_4.

3.2.6 Heterogeneous catalytic activity of NiFeCpN for H_2 production

Currently, a large number of bio-inspired FeFe or NiFe electrocatalysts have been reported for the activity of H_2 production in homogeneous organic solutions.[9, 132] However, they suffer from low stability under homogeneous conditions required for sustainable applications. Additionally, their use in aqueous solutions is limited due to their low solubility in such media. In order to overcome these drawbacks, the immobilization of electrocatalysts on electrode surfaces is one of the most promising strategies. Both $Ni^{II}Fe^{II}Cp$ and $Fe^{II}Fe^{II}Cp$ display good rates ($Fe^{II}Fe^{II}Cp$: TON = $4.9(0.1)*10^5$ in 9 hours, TOF = 15.3(0.3) s^{-1}, at −0.80 V vs SHE, pH 4; $Ni^{II}Fe^{II}Cp$: TON = $7.2*10^6$ in 10 hours, TOF = 200 s^{-1}, at −0.85 V vs SHE, pH 3) for H_2 evolution in acidic aqueous solution after their heterogenization by physical absorption on edge-plane graphite (EPG) electrodes.

In this context, the NiFeCpN complex has been immobilized on EPG electrodes by physical absorption to form a hybrid electrocatalyst NiFeCpN/EPG. Linear sweep

voltammetry (LSV) has been carried out in phosphate buffer aqueous solution at different pH values. A clear catalytic behavior is observed for H_2 production when the pH is at 6.90, 5.28 and 4.05 (**Figure 3.23**). The current intensity of this wave continues to increase with decreasing pH values. Interestingly, comparing to the raw graphite without catalyst, a significant increase at current intensity (current difference, △I= 670 μA at −1.0 V vs Ag/AgCl) is observed at pH 4.05 when NiFeCpN/EPG is used, indicating the catalytic role of the complex. This result confirms that the hybrid electrocatalyst NiFeCpN/EPG possesses catalytic properties for H_2 production under heterogeneous conditions. The overpotential of the NiFeCpN/EPG is calculated to be about 130 mV at the onset of the catalytic wave at pH 4.05. In addition, the current differences of $Ni^{II}Fe^{II}Cp$/EPG and $Fe^{II}Fe^{II}Cp$/EPG are 200 μA at −1.0 V vs SHE at pH 3 and 280 μA at −0.9 V vs SHE at pH=3, respectively. Their overpotential is calculated to be about 460 mV at the onset of the catalytic wave. The NiFeCpN/EPG displays a larger current difference and a lower overpotential relative to $Ni^{II}Fe^{II}Cp$/EPG and $Fe^{II}Fe^{II}Cp$/EPG. These data demonstrate that NiFeCpN/EPG has a better activity for H_2 production in acidic aqueous solution than the $M^{II}Fe^{II}Cp$/EPG (M= Ni and Fe). This result once again confirms that the presence of the pendant amine enhances the electrocatalytic activity for H_2 production, which can act as a proton relay.

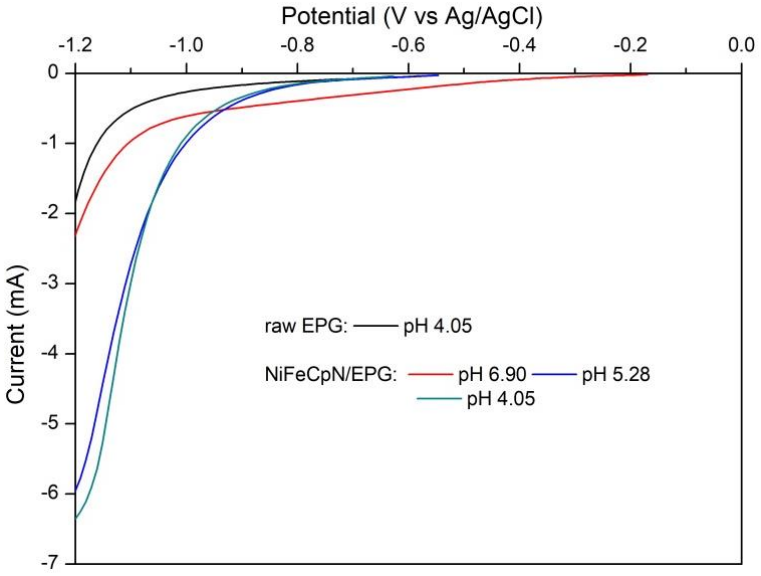

Figure 3.23 LSVs of NiFeCpN/EPG (13 mm diameter) recorded at different pHs (red line: 6.90, blue line: 5.28 and cyan line: 4.05). LSV of the raw EPG electrode at pH 4.05 phosphate buffer (black line). Conditions: 0.1 M phosphate buffer aqueous electrolyte at *v* = 100 mV/s under Ar, Ag/AgCl (3.5M KCl) reference and Pt counter electrodes.

3.2.7 Synthesis and characterization of $[L^{N2S2}Co(CO)FeCpNH]BF_4$

As described above, the amine-modified NiFeCpN complex has been synthesized and characterized. The experiments confirm that it has a better activity for H_2 production than the $M^{II}Fe^{II}Cp$ analogs. Some cobalt-based electrocatalysts have been reported for H_2 production in recent years.[133, 134] In this context, the $[L^{N2S2}Co(CO)FeCpNH]BF_4$ (CoFeCpNH) complex bearing a pendant amine has been synthesized by substituting Ni with Co and its redox properties and electrocatalytic activity for H_2 production have been investigated.

The FeCpN complex reacts with CoL in dry CH_2Cl_2 to produce the expected dinuclear CoFe complex (**Figure 3.24**). In the IR spectrum of recorded from the CH_2Cl_2 solution, a CO vibration at 1984 cm^{-1}, assigned to the FeCpN is observed but faded away with time and no other feature is observed in the expected range for CO vibrations. In the ESI-MS spectrum of the CH_2Cl_2 solution, a peak at m/z = 637.15 is observed, assigned to the CoL complex. No expected peaks for the heterodinuclear CoFe complex are observed in the ESI-MS spectrum. It can thus be concluded that the expected dinuclear CoFe complex is not synthesized in CH_2Cl_2.

Considering that the solvent may have an effect on the synthesis, MeCN has been employed as the solvent instead of CH_2Cl_2 (**Figure 3.24**). FeCpN complex reacts with CoL in dry MeCN. After overnight, no the expected CO vibrations are observed in the IR spectrum of the reaction solution. In the ESI-MS spectrum recorded from the MeCN solution, no expected peak is observed. The heterodinuclear CoFe complex is also not formed in MeCN.

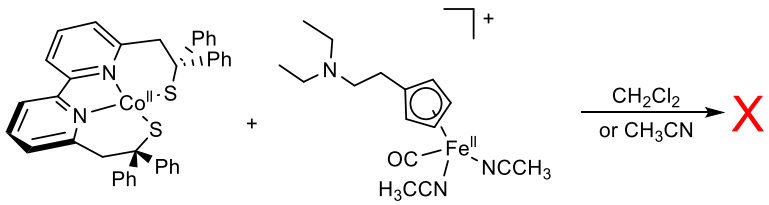

Figure 3.24 Reactions of CoL and FeCpN complexes.

It has been reported in the literature, the $[FeCp(CO)_2(THF)]BF_4$ complex reacts with Ni complex to produce dinuclear $[Ni(xbsms)FeCp(CO)_2](BF_4)$ (H_2xbsms = 1,2-bis(4-mercapto3,3-dimethyl-2-thiabutyl)benzene) complex with two CO ligands. One CO ligand can be removed from this NiFe complex through daylight.[135] Therefore, the complex $[FeCpN(CO)_2(MeCN)]BF_4$ (2e, **Figure 3.9**) has been used to react with CoL in dry CH_2Cl_2 to produce the CoFe complex (**Figure 3.25**). Unfortunately, in the IR spectrum, the CO vibrations at 2037 cm^{-1} and 2079 cm^{-1} assigned to the $[FeCpN(CO)_2(MeCN)]BF_4$ complex, decrease with time and no other features are observed in the expected range for CO vibrations. Thus, the expected heterodinuclear CoFe complex is also not obtained under these conditions.

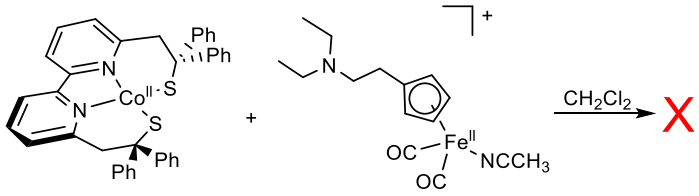

Figure 3.25 Reaction between the CoL and $[FeCpN(CO)_2(MeCN)]BF_4$ complexes.

Reactions between $[FeCp(CO)_2(I)]$ and a Ni complex have been reported in the literature.[136] Then, the $[FeCpN(CO)_2(I)]$ (2d, **Figure 3.9**) has also been used as starting Fe brick. It has been added to a CH_2Cl_2 solution of CoL to produce the CoFe complex (**Figure 3.26**). In the IR spectrum, the two CO vibrations observed at 1998 cm^{-1} and 2042 cm^{-1} corresponding to the $[FeCpN(CO)_2(I)]$ complex shift to 1990 cm^{-1} and 2036 cm^{-1}. In the ESI-MS spectrum of the CH_2Cl_2 solution, a peak at m/z = 885.17 is observed, assigned to the dinuclear $[L^{N2S2}Co(CO)FeCpN]^+$ complex. These data indicate that the heterodinuclear CoFe complex can be formed under these conditions. Then, we have tried to remove one CO ligand by using Me_3NO. Unfortunately, in the final IR spectrum the two CO vibrations have disappeared and no other CO vibrations are observed. The CoFe complex with only one CO ligand cannot be obtained.

We thus decided to investigate the redox properties of this CoFe complex with two CO ligands in MeCN. Its CV displays many redox processes, which are difficult to analyze, and also indicate that the isolated powder may be a mixture of complexes rather than the pure CoFe complex with two CO ligands.

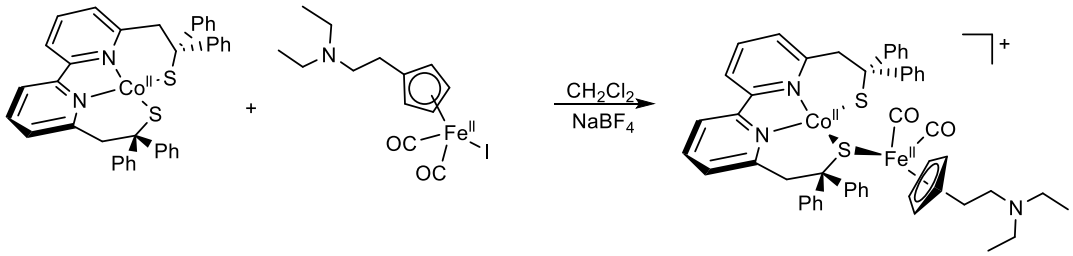

Figure 3.26 Reaction between the CoL and $[FeCpN(CO)_2(I)]$ complexes.

We have shown that the protonated FeCpPyH complex can react with NiL to form the corresponding NiFe complex (**Figure 3.7**). In order to obtain pure CoFe complex with the amine group, we have used the protonated form of FeCpN to react with CoL. Since the $[FeCpN(CO)_2(I)]$ (2d) complex is stable in air for a long time, we used it in our first trial. It was protonated using HCl to produce $2d^{H1}$ with a yield of 95% (**Figure 3.27**). Then we exchanged the counterion in $2d^{H2}$ with PF_6^-. The iodide has been removed by addition of $AgBF_4$ to generate the mononuclear Fe-THF complex with two CO ligands. Finally, one CO ligand has been removed from $2e^H$ by irradiation (20 h) to give the desired product FeCpNH.

The CO vibrations of both 2d and $2d^{H1}$ complexes are observed at 1981 cm^{-1} and 2027 cm^{-1} in solid state IR spectra. In ^1H NMR spectrum, a broad peak is observed at

8.35 ppm, which is assigned to –NH. These data confirm that the amine group is protonated. The CO vibrations of $2d^{H2}$ are observed at 1985 cm^{-1} and 2032 cm^{-1}. The CO vibrations of $2e^{H}$ are observed at 2078 cm^{-1} and 2029 cm^{-1}. For the FeCpNH complex, its CO vibration is observed at 1980 cm^{-1} in MeCN, which is similar to the CO vibration of the FeCpN complex.

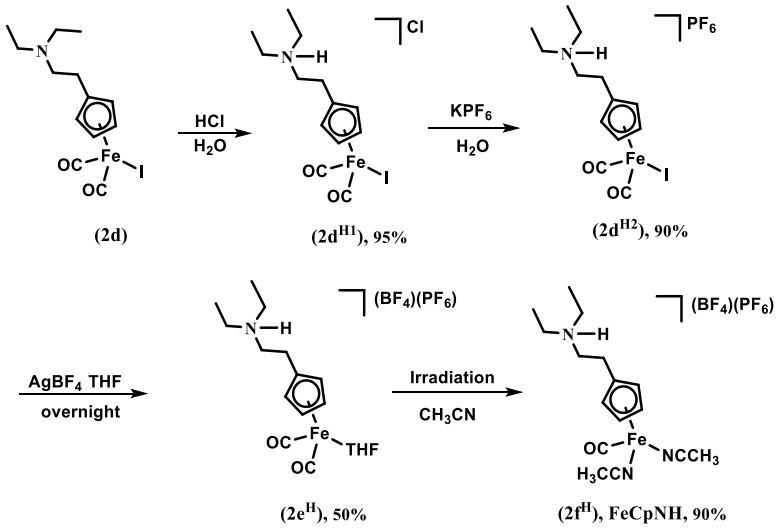

Figure 3.27 Synthetic route for the synthesis of FeCpNH complex.

CoL was then added to a CH_2Cl_2 solution of FeCpNH. The CO vibration of the reaction solution at 1985 cm^{-1} disappears gradually by IR monitoring and no other CO vibration appears in the expected range of CO vibrations. Thus, the targeted CoFe complex cannot be obtained under these conditions. MeCN has been also tested as the solvent instead of CH_2Cl_2 (**Figure 3.28**). After the reaction work-up, pentane is added into the reaction solution to precipitate a black-brown solid with a yield of 62%.

In the ESI-MS spectrum of the CH_2Cl_2 solution, a peak at m/z = 885.24 is observed, assigned to the expected $[CoFe(CO)CpN]^+$ complex. In the solid-state IR spectrum, one CO stretching vibration is observed at 1896 cm^{-1} (**Figure 3.29**). Its energy is close to the terminal Fe-CO vibration found in $Ni^{II}Fe^{II}Cp$ (1926 cm^{-1}), $Ni^{II}Fe^{II}Cp^*$(1929 cm^{-1}) and NiFeCpN (1920 cm^{-1}), and differs significantly from the bridged M-CO-M vibration found in $Fe^{II}Fe^{II}Cp$ (1822 cm^{-1}) and $Co^{II}Fe^{II}Cp$ (1856 cm^{-1}). Therefore, it is proposed that the CO ligand is terminally bound to Fe site in the CoFeCpNH complex.

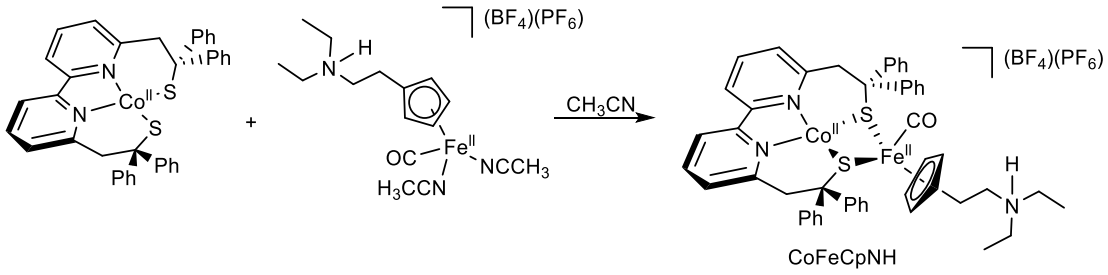

Figure 3.28 Synthesis of the CoFeCpNH complex.

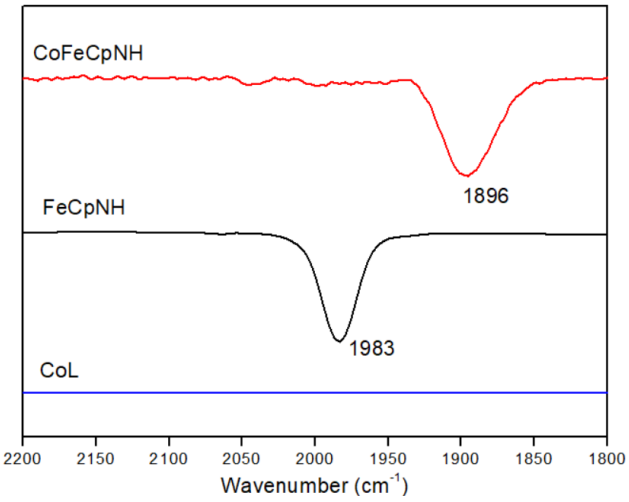

Figure 3.29 IR spectra of the FeCpNH (black line) CoFeCpNH (red line) and CoL (blue line) complexes in CH_2Cl_2.

3.2.8 Redox properties of CoFeCpNH

The CV of the CoFeCpNH complex has been recorded in MeCN. It displays two reversible redox events at $E_{1/2}$= −0.95 V ($\triangle E$ = 54 mV) and $E_{1/2}$= −2.03 V ($\triangle E$ = 67 mV) vs $Fc^{+/0}$, and two irreversible systems, at E_{pc}= −1.62 V and E_{pc}= −1.81 V vs $Fc^{+/0}$ (**Figure 3.30**). In order to investigate the effect of the solvent on its redox properties, the CV of CoFeCpNH has been recorded in a DMF solution. The potential of all reduction events shifts to a more negative potential by about 50-70 mV in DMF with respect to that in MeCN, indicating that the CoFeCpNH complex is easier to reduce in MeCN.

Based on the comparison of its redox properties to those of the analogous $Co^{II}Fe^{II}Cp$, $Ni^{II}Fe^{II}Cp$, $Fe^{II}Fe^{II}Cp$ and NiFeCpN complexes (**see section 3.2.3, table 3.1**), we proposed the following assignments. The redox system at $E_{1/2}$= −0.95 V in the CV of CoFeCpNH can be attributed to the $Co^{II/I}$ reduction in MeCN ($E_{1/2}$= −1.04 V in DMF). Plots of the peak current (i_{pc}) versus the square root of the scan rate (v) are linear in MeCN, indicating that this redox process is diffusion-controlled (**Figure 3.30**). This potential is shifted to an even greater extent (660 mV) as compared to the mononuclear CoL, which displays a quasi-reversible $Co^{II/I}$ wave at $E_{1/2}$= −1.70 V in DMF. In addition, compared with the $Ni^{II/I}$ reduction and the $Fe^{II}Fe^{II}/Fe^{1.5}Fe^{1.5}$ reduction in $M^{II}Fe^{II}$ analogs, the CoFeCpNH is the easiest to reduce in MeCN.

For NiFeCpN, the reduction wave at −1.86 V corresponds to the reduction of the bipyridine moiety from mononuclear NiL, due to its decomposition into NiL and FeCpN. Based on this observation, it is proposed that the redox system at $E_{1/2}$= −2.03 V is assigned to the reduction of the bipyridine moiety from the mononuclear CoL complex, evidencing the decomposition of CoFeCpNH into CoL and FeCpN.

Two irreversible redox behaviors also occur in MeCN at E_{pc}= −1.62 V and E_{pc}= −1.81 V. In the case of NiFeCpN, the reduction wave at E_{pc} = −1.60 V is assigned to the

reduction of the protonated form of the one-electron reduced NiFeCpN. For CoFeCpNH, we propose that at E_{pc}= −1.62 V also corresponds to protonated species of the reduced species, while that at E_{pc}= −1.81 V of the reduction of the double protonated form. In order to verify this hypothesis, Et_3N as a base source has been added to an electrolyte solution of the CoFeCpNH.

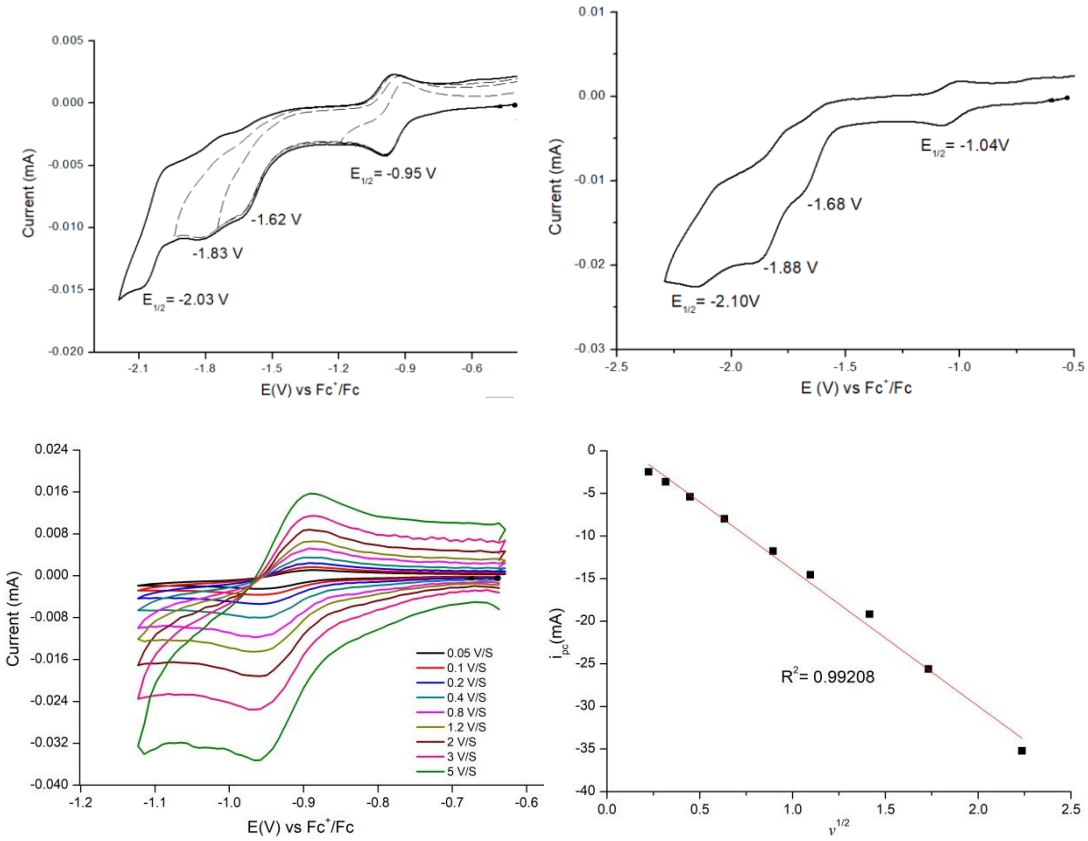

Figure 3.30 CVs of 0.32 mM of CoFeCpNH in MeCN (top, left) or 0.43 mM of in DMF (top, right) in 0.1 M n-Bu_4NClO_4 on a glassy carbon electrode at *v* = 100 mV/s. Cathodic peak current (i_{pc}) dependence vs the square root of the scan rate ($\nu^{1/2}$) for the redox systems observed at $E_{1/2}$ = −0.95 V vs $Fc^{+/0}$ in the CVs of CoFeCpNH (bottom, left). The linear fits of these data are displayed together with the corresponding R^2 value (bottom, right).

Upon the addition of 1 eq Et_3N, two reduction waves at E_{pc} = −0.99 V and −1.83 V are shifted by 40 mV to more negative potentials (**Figure 3.32**, left). Simultaneously, the reduction wave at E_{pc} = −1.62 V disappears. In UV-vis spectra, a slight change is observed with the shift of the transition from 563 nm to 576 nm (**Figure 3.32**, right). After the addition of another 1 eq base, the CV and UV-vis spectrum do not change. It can be concluded that the CoFeCpNH complex is deprotonated under these conditions (**Figure 3.31**). Upon the addition of 0.5 eq Et_3NH^+, an increase in the current is observed at about −1.62 V and E_{pc} = −1.83 V, indicating the formation of additional species and catalytic events.

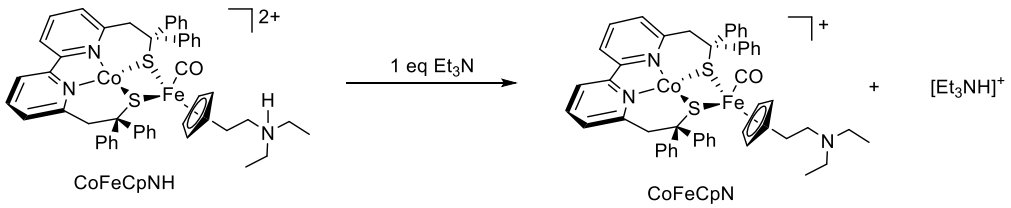

Figure 3.31 Deprotonation of the CoFeCpNH complex.

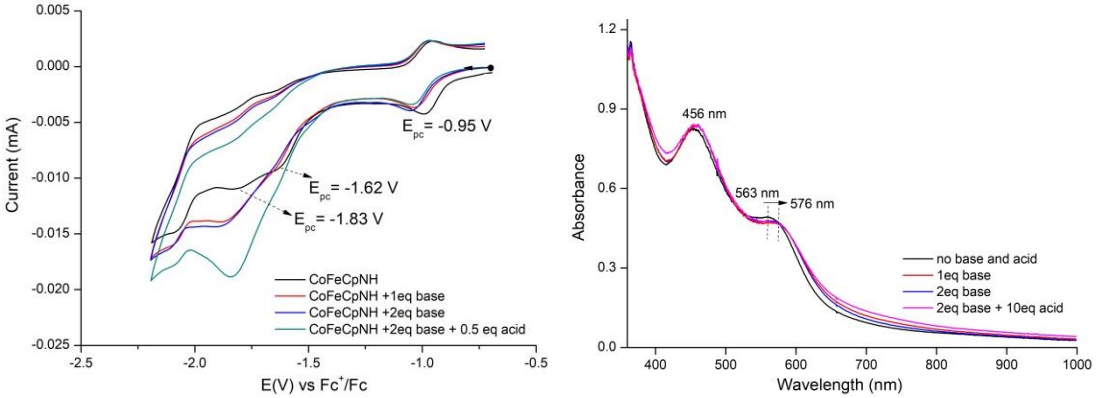

Figure 3.32 CVs (left) of the CoFeCpNH (0.32 mM, black line) with Et_3N (1 eq for red line, 2 eq for blue line) and 2 eq Et_3N + 0.5 eq Et_3NH^+ (cyan line) in 0.1 M n-Bu_4NClO_4/MeCN, on a glassy carbon electrode at *v* = 100 mV/s. The UV-vis spectrum (right) of the CoFeCpNH (0.32 mM, red line) with 2 eq Et_3N (cyan line) and 2 eq Et_3N + 10 eq Et_3NH^+ (blue line) in electrolyte.

3.2.9 Homogeneous catalytic activity of CoFeCpN for H_2 production

The CoFeCpNH has been deprotonated by the base before adding the Et_3NH^+ to form CoFeCpN (see **Figure 3.31**). The electrocatalytic activity for H_2 production of CoFeCpN has been evaluated in the presence of Et_3NH^+ as a proton source. The catalytic potential for Et_3NH^+ is observed at more negative potential in the absence of CoFeCpN, indicating the catalytic role of the complex (**Figure 3.32**, black line). For the mononuclear FeCpNH, the observed catalytic current intensity is lower than that of NiFeCpN, demonstrating a better activity for the heterodinuclear CoFe complex (**Figure 3.31**, red line). In the presence of Et_3NH^+ and CoFeCpN, a catalytic process is observed at $E_{cat/2}$ = −1.83 V vs $Fc^{+/0}$ (measured at the half-wave) (**Figure 3.33 and 3.34**). The overpotential is calculated to be 0.69 V.

Compared to the analogs $Ni^{II}Fe^{II}Cp$ (η = 0.68 V), $Ni^{II}Fe^{II}Cp^*$ (η = 0.69 V), and $Fe^{II}Fe^{II}Cp$ (η = 0.73 V), CoFeCpN has a similar overpotential under similar conditions (**Table 3.1**). CoFeCpN has a more negative catalytic potential with respect to NiFeCpN ($E_{cat/2}$ = −1.73 V) indicating that the presence of the Ni ion leads to a better activity for H_2 production with a Co ion. Interestingly, $Co^{II}Fe^{II}Cp$ has no activity for H_2 production under similar conditions. These data confirm that the presence of the pendant amine

group enables this CoFe complex to catalyze H_2 production, evidencing its notable impact under catalytic process. The CoFeCpN complex catalyzes the H_2 production with a much lower overpotential compared to analogs $[28]^+$ (η = 1.06 V) and $[29]^+$ (η = 1.27 V, **see 1.1.5 section**).[130] This also further enhances the effect of the pendant amine for H_2 production.

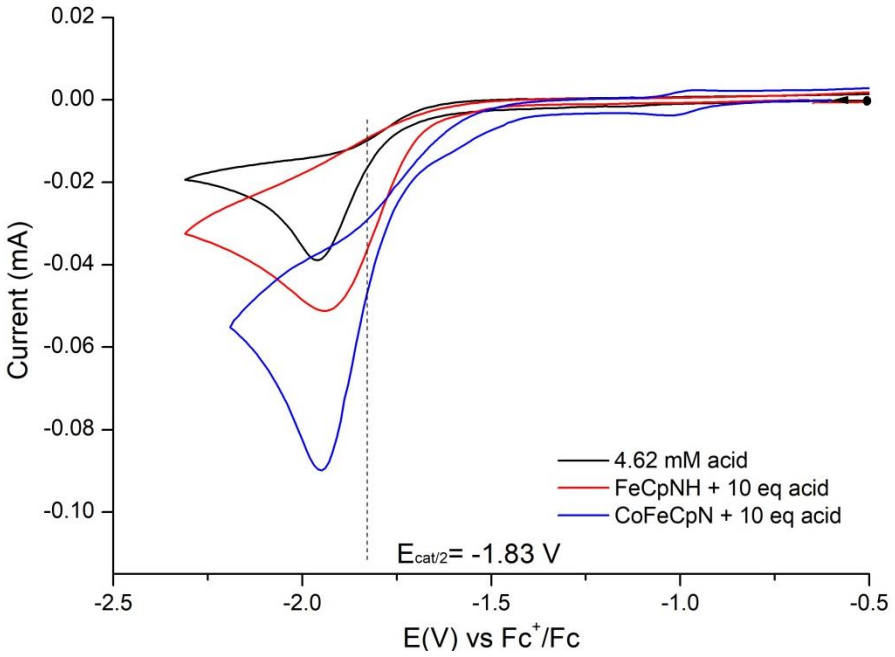

Figure 3.33 CVs of CoFeCpN (0.32 mM) + 10 eq Et_3NH^+ (blue line), FeCpNH (0.34 mM) + 10 eq Et_3NH^+ (red line) and Et_3NH^+ (4.62 mM, black line) under similar conditions. Conditions: electrolyte: 0.1 M n-Bu_4NClO_4/MeCN, on a glassy carbon electrode at *v* = 100 mV/s.

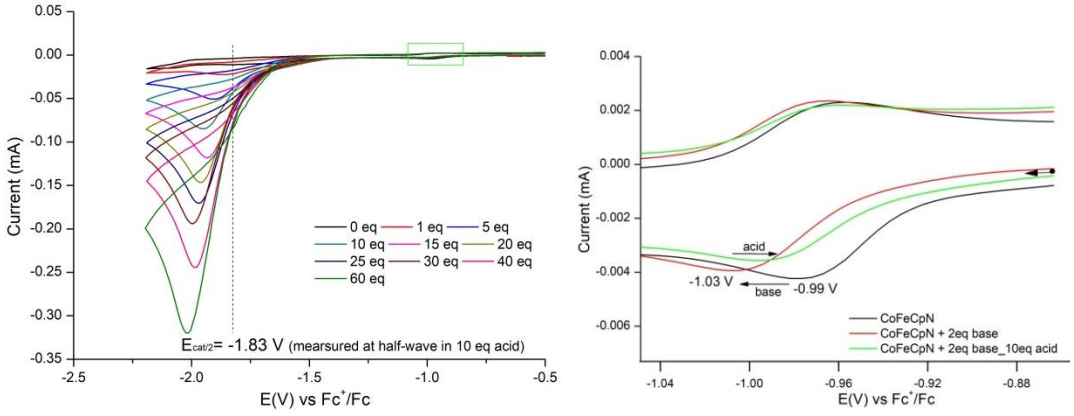

Figure 3.34 CVs of 0.32 mM of CoFeCpN with various amounts of Et_3NH^+. The figure at the right is a zoomed-in view in the green box. Conditions: electrolyte: 0.1 M n-Bu_4NClO_4/MeCN, on a glassy carbon electrode at *v* = 100 mV/s.

3.2.10 Mechanistic investigations for H_2 production with CoFeCpNH

According to the above experiments, we also have demonstrated that CoFeCpN catalyzes H_2 production by adding Et_3NH^+ as the proton source (**Figure 3.33 and Figure 3.34**). When additional equivalents of Et_3NH^+ have been added, the redox event at E_{pc} = −1.03 V vs $Fc^{+/0}$ assigned to the reduction of Co^{II} to Co^{I}, continues to shift toward anodic potential (**Figure 3.32, left**). Moreover, no new reduction peaks are observed on the CV timescale. In the UV-vis spectrum of CoFeCpN in the electrolyte MeCN solution, the observed two transitions are not changed after the addition of acid (**Figure 3.32, right**), as observed with NiFeCpN under similar conditions. This result indicates that the CoFeCpN is not protonated in the presence of Et_3NH^+. We can therefore propose a catalytic cycle similar to that with NiFeCpN for the deprotonated from $LCo^{II}Fe^{II}N$ using Et_3NH^+. A more detailed description is that $LCo^{II}Fe^{II}N$ is reduced first at −1.03 V to form $LCo^{I}Fe^{II}N$, which is then protonated to generate $LCo^{I}Fe^{II}NH$ or $LCo^{III}(H^{hyd})Fe^{II}N$ species. This species is further reduced at −1.62 V and its protonation to yield $LCo^{II}(H^{hyd})Fe^{II}NH$ species. This resulting species is reduced at −1.83 V, and then leads to the release of H_2 and generate $LCo^{I}Fe^{II}N$ state with an E[CECE] mechanism (**Figure 3.35**). Therefore, the $Co^{I}Fe^{II}$ is the entry of the catalytic cycle in the presence of Et_3NH^+, not $Co^{II}Fe^{II}$.

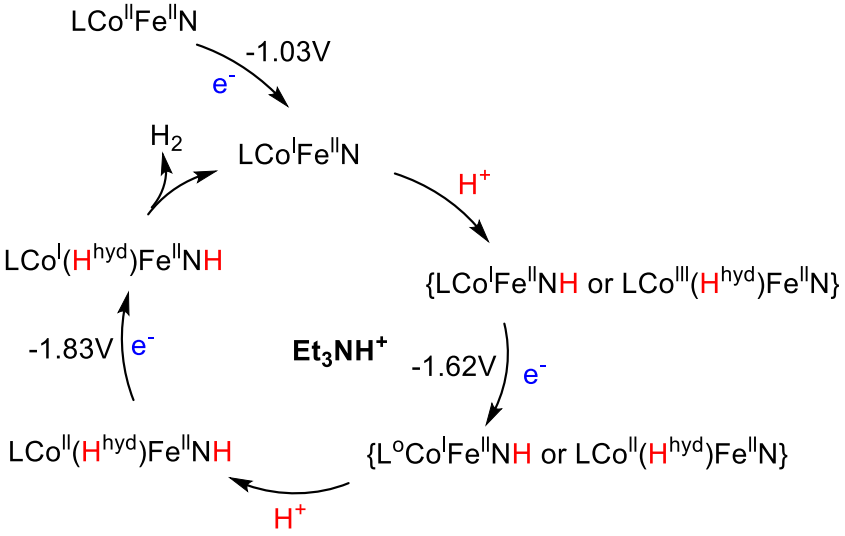

Figure 3.35 Proposed intermediate states with complex CoFeCpN under the catalytic cycle in the presence of Et_3NH^+.

In order to further investigate the mechanism, the stronger acid HBF_4 also been also used as the proton source. As the acid concentration increases, for protonated form CoFeCpNH, the reduction wave at E_{pc} = −0.99 V vs $Fc^{+/0}$, corresponding to the reduction of Co^{II} to Co^{I}, is shifted towards the anodic potential, and becomes irreversible (**Figure 3.36**). In addition, a similar change has been observed in

$[Co(bapbpy)Cl]^+$ in the presence of HBF_4 (see section 3.2.5).[131] Moreover, a new reduction process appears at −1.11 V vs $Fc^{+/0}$, and the current intensity increases with increasing acid concentration **(Figure 3.36)**, indicating a catalytic behavior. For more negative reduction waves below about −1.5 V, we will not discuss in this section due to lack of experimental support.

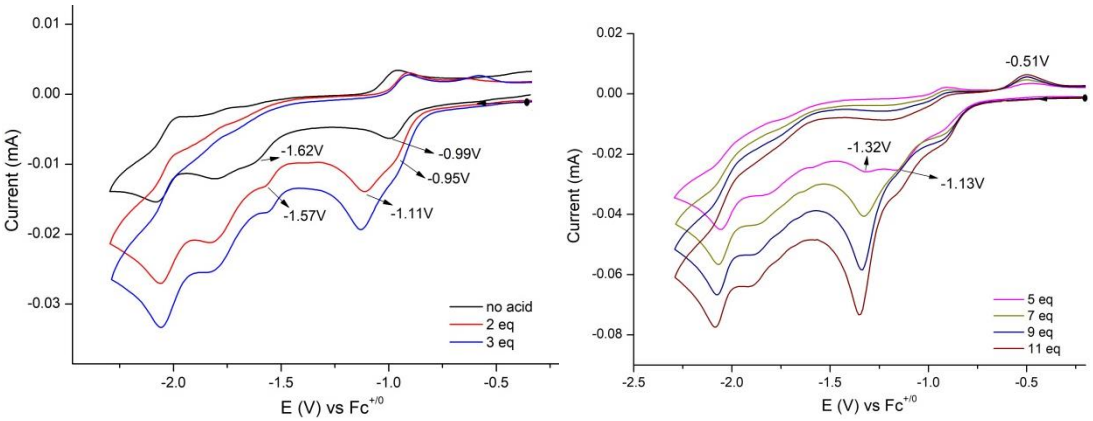

Figure 3.36 CVs of 0.38 mM of CoFeCpNH in MeCN in the absence (blank line) or in the presence of HBF_4: 2 eq (red line), 3 eq (blue line), 5 eq (pink line), 9 eq (deep blue line), and 11 eq (red-brown line). Conditions: electrolyte: 0.1 M n-Bu_4NClO_4/MeCN, on a glassy carbon electrode at *v* = 100 mV/s.

In the UV-vis spectrum of CoFeCpNH in an electrolyte MeCN solution, after the addition of 2 eq of HBF_4, the transition at 456 nm is almost unchanged while the intensity of that at 563 nm is reduced (**Figure 3.37**). After the addition of 11 eq of HBF_4, the transition at 456 nm shifts to 438 nm, and the intensity of that at 563 nm continues to decrease (**Figure 3.37**). These results indicate that CoFeCpNH and HBF_4 react together. It is also noted that an anodic wave at −0.51 vs $Fc^{+/0}$ appears, whose intensity gradually increases with increasing acid concentration, corresponding to the oxidation of the reduced form of the mononuclear FeCpN fragment (**Figure 3.13**). This demonstrates that in the presence of a large excess of HBF_4, CoFeCpNH decomposes gradually.

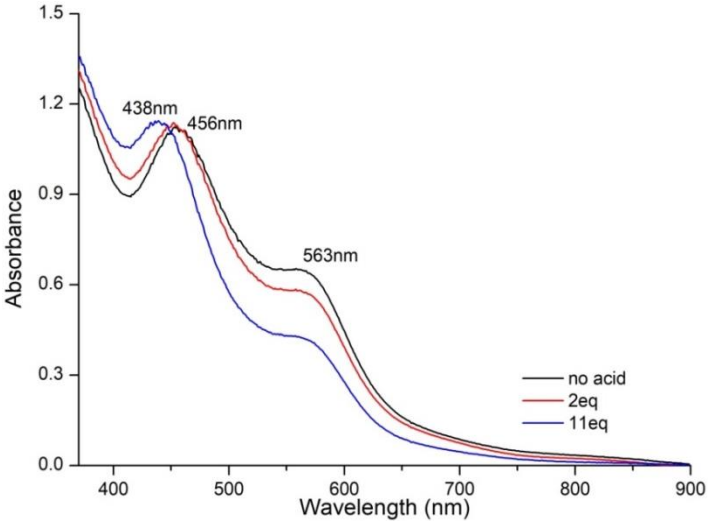

Figure 3.37 UV-vis spectrum of 0.38 mM of CoFeCpNH in electrolyte in the absence (blank line) or in the presence of HBF_4: 2 eq (red line) and 11 eq (blue line). l (cuvette) = 1 cm.

Based on these experiments, we can propose that $LCo^{II}Fe^{II}NH$ is reduced at −0.95 V to form $LCo^{I}Fe^{II}NH$ or $LCo^{III}(H^{hyd})Fe^{II}N$ species. This species further is protonated to generate an ammonium hydride species $LCo^{III}(H^{hyd})Fe^{II}NH$. In addition, the reduction wave at −1.11 V has been proposed to assign to the reduction of the ammonium hydride species. It then directly releases H_2 with a [ECEC] mechanism (**Figure 3.38**).

For the NiFeCpN and CoFeCpNH, we can see that the proposed catalytic cycles all involve hydride-ammonium species. Such species have been observed in $[Co(bapbpy)Cl]^{+}$[131], Dubois' Ni complexes[137] and bio-inspired FeFe complex.[42, 47, 138] Generally, the proximity between the ammonium proton and the Fe-H hydride promoted the formation and release of H_2 in the hydride-ammonium species of the catalytic cycle, as discussed in **section 1.1.3**. It can be concluded that hydride-ammonium species may be a key intermediate during the catalytic process.

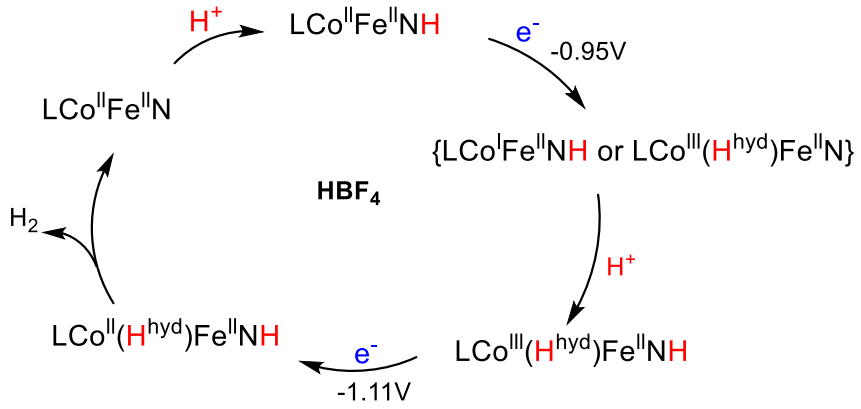

Figure 3.38 Proposed intermediate states with complex CoFeCpNH under the catalytic cycle in the presence of HBF_4.

3.3 Conclusions

Three new complexes, NiFeCpPy, NiFeCpN and CoFeCpNH, bearing a pendant amine have been synthesized and characterized by IR and UV-vis spectroscopy and ESI-MS spectrometry.

NiFeCpN is more stable than NiFeCpPy, since NiFeCpPy easily loses one CO ligand. Both NiFeCpN and CoFeCpNH complexes display electrocatalytic activity for H_2 production in MeCN in the presence of Et_3NH^{+}.

NiFeCpN displays a lower overpotential (η = 0.59 V) with a shift of 100 mV with respect to the analogs MFe for H_2 production.

The amino-modified CoFe complex has the ability to catalyze H_2 production contrary

to its analog $Co^{II}Fe^{II}Cp$.

The choice of acid leads to different mechanisms, specifically in the sequence of the two protonation and reduction processes.

In addition, after their physical adsorption on graphite, the modified electrode with NiFeCpN displays a better electrocatalytic activity than that with $Ni^{II}Fe^{II}Cp$ in acidic aqueous solution (pH=4).

Therefore, this overall data confirm that the pendant amine group has a strong impact on the performance of the electrocatalysts for H_2 production. In future work, we will try to analyze the obtained product by electrolysis to further investigate the catalytic mechanism of the NiFeCpN and CoFeCpNH complexes for H_2 production, and to understand the role of the amine groups.

Chapter 4 Bio-inspired MFe (Co and Ni) complexes for CO_2 reduction

4.1 Introduction

CO_2 represents a potential feedstock for the synthesis of value-added fine chemicals and fuels because of its low cost and toxicity, high abundance, and relative ease of transport.[82-85] Electrocatalytic CO_2 reduction is an attractive pathway to convert CO_2 into organic fuels and useful chemicals.[87] In nature, the active site of the NiFe carbon monoxide dehydrogenase (NiFe CODH) consists of a Ni center and a Fe center bridged by an $[Fe_3S_4]$ cluster that rigidly positions these two metal centers in close proximity to each other. This enzyme reversibly reduces CO_2 to CO via the synergistic function of both the Ni and Fe centers during the catalytic process.[82, 139-141] It should be noted that the active sites of NiFe CODH and [NiFe] H_2ase display similar key structures; both contain Ni and Fe metal ions and a sulfur-rich coordination sphere. The catalytic process for both CO_2 reduction and H_2 production involves protonation reactions and electron transfer processes. It is reasonable to infer that bio-inspired models of H_2ase are capable of catalyzing the reduction of CO_2. Bio-inspired FeFe models for CO_2 reduction have been reported in the literature. The bio-inspired $[(\mu\text{-bdt})Fe_2(CO)_6]$ ([32], **Figure 1.24**) and $[(\mu\text{-edt})Fe_2(CO)_6]$ complexes have the ability to catalyze the reduction of CO_2 to a mixture product (HCOOH, CO and H_2) at E_{cat}= −2.35 V in the presence of CH_3OH as a proton source.[99] However, the proton reduction is a highly competitive reaction with CO_2 reduction. Therefore, it is essential to develop proper catalysts with enhanced activity and selectivity for CO_2 reduction.[142] In addition, a related bio-inspired Co-based complex of the NiFe CODH has been extensively employed as an electrocatalyst for CO_2 reduction with notable performance (complex [31], $\eta < 100$ mV, FE > 93%).[98]

Interestingly, the addition of a pendant amine in the second coordination sphere has been used to tune the catalytic activity and selectivity of several electrocatalysts for CO_2 reduction.[143] For example, the Fe porphyrin [33], complex[101] bearing a pendant amine group (**Figure 1.25**) catalyzes CO_2 reduction into HCOOH at −1.55 V vs $Fc^{+/0}$ in the presence of H_2O in DMF. The experiments and DFT calculations indicate that the protonation of the amine group is an essential step during the catalytic process since CO_2 binds to the Fe^{I} state only when it is protonated. Accordingly, the complex [34] that not bears an amine group does not show activity for CO_2 reduction in the presence of H_2O. These data clearly demonstrate that the pendant amine can have a critical role in CO_2 reduction.

As mentioned in the previous sections, $Ni^{II}Fe^{II}Cp$ displays good performance for H_2 production. Moreover, our group has shown that $Ni^{II}Fe^{II}Cp$ is a multifunctional catalyst. It can catalyze the reduction of CO_2 to produce a mixture of CH_4 and H_2 at

E_{cat}= –1.3 V vs SHE after its immobilization on a graphite electrode by physical adsorption in a pH 4 acidic aqueous solution.[100] In addition, the new bio-inspired amino-modified MFe (Ni and Co) complexes have been described in chapter 3. Inspired by the above discussions, the NiFeCpN and CoFeCpNH complexes have been investigated for CO_2 reduction in the present chapter.

4.2 Result and discussion

4.2.1 Homogenous catalytic activity of NiFeCpN for CO_2 reduction

In initial studies, CVs experiments for the NiFeCpN have been carried out in MeCN under Ar and saturated CO_2 atmospheres (**Figure 4.1**). When the solution is saturated with CO_2, an increased current is observed at E_{pc}= –1.86 V (**Figure 4.1**, red line), showing an interaction between NiFeCpN and CO_2. When the solution of the NiFeCpN is filled with Ar again, the initial CV is recovered (**Figure 4.1**, blue line). This data indicates that the structure of NiFeCpN is remained intact under a CO_2 atmosphere.

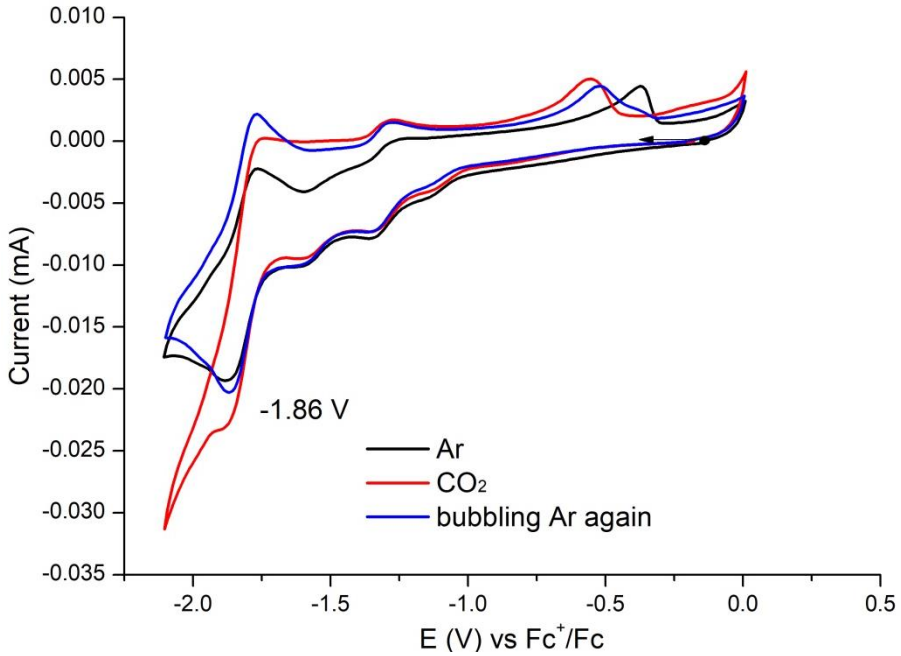

Figure 4.1 CVs of NiFeCpN (0.57 mM) under Ar (black line), CO_2 (red line) and bubbling Ar again (blue line) in MeCN, 0.1 M n-Bu_4NClO_4, on a glassy carbon electrode at v = 100 mV/s.

Since CO_2 reduction requires protonation steps, TFE (CF_3CH_2OH) has been chosen as the proton source in this content. In the presence of TFE under Ar, the CVs of NiFeCpN show that a reduction wave at E_{pc}= –1.60 V is shifted to –1.70 V and an

increased current is observed below –1.70 V (**Figure 4.2**, blue line). This is the indication of a proton reduction catalytic event. The electrochemical behavior of TFE in the absence of NiFeCpN is investigated as a control experiment (**Figure 4.2**, red line). The CV displays a catalytic current at a much more negative potential than that of NiFeCpN, indicating that the complex has a catalytic role in H_2 production.

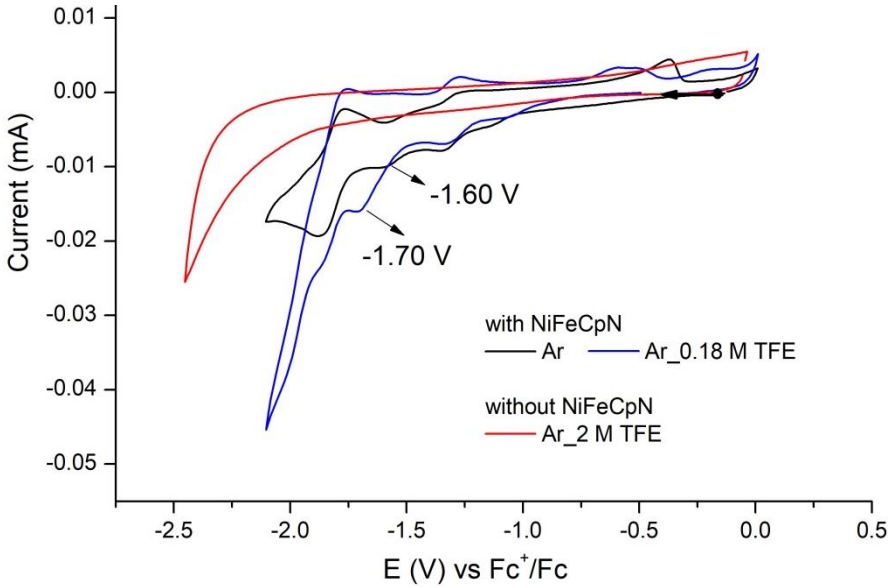

Figure 4.2 CVs of NiFeCpN (0.57 mM) under Ar (black line), Ar with TFE (blue line), and of TFE without NiFeCpN under Ar (red line) in MeCN, 0.1 M n-Bu_4NClO_4, on a glassy carbon electrode at v = 100 mV/s.

Interestingly, in the presence of TFE under CO_2 atmosphere, a larger increase of the current is observed at E_{pc}= –1.86 V (**Figure 4.3**), indicating a CO_2 reduction catalytic event. Compared with the mononuclear FeCpNH complex, the dinuclear NiFe complex offers a larger current intensity at a more positive catalytic potential (**Figure 4.3**), indicating a better activity of the dinuclear complex. Therefore, the combined data indicate that the electrocatalyst NiFeCpN has the ability to catalyze the reduction of CO_2.

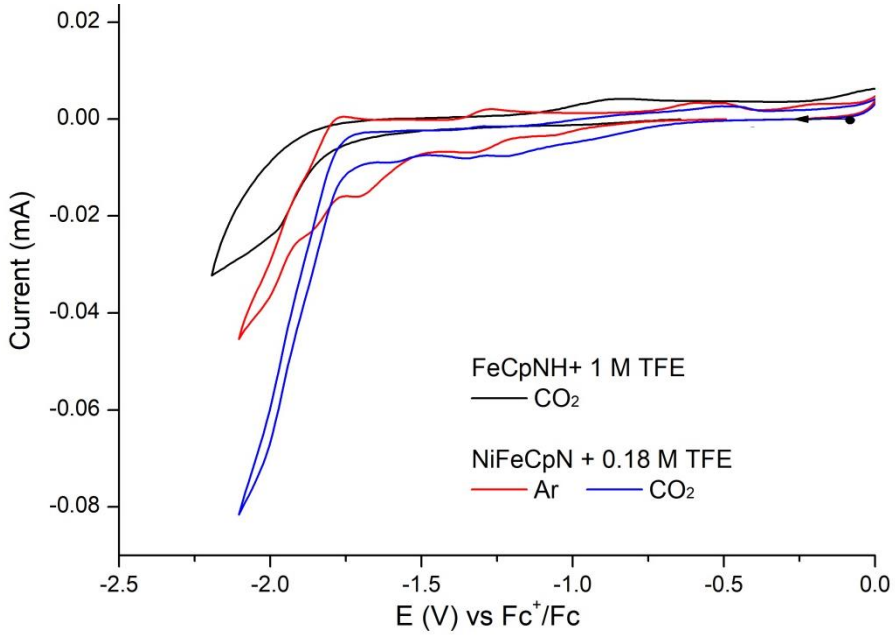

Figure 4.3 CVs of NiFeCpN (0.57 mM) + TFE under Ar (red line) and CO_2 (blue line). CV of FeCpNH (0.68 mM) + TFE under CO_2 atmosphere (black line). Conditions: 0.1 M n-Bu_4NClO_4 in MeCN, on a glassy carbon electrode at v = 100 mV/s.

For the NiFeCpN complex, the onset catalytic potential is observed at E_{cat} = −1.73 V vs $Fc^{+/0}$ in the presence of TFE **(Figure 4.4)**. The current intensity of the catalytic wave continuously increases by increasing the amount of TFE **(Figure 4.4)**. An electrolysis experiment has been carried out at −1.70 V vs $Fc^{+/0}$, a purple precipitate is formed after a few seconds. This purple precipitate corresponds to the formation of the mononuclear NiL complex, which is insoluble in MeCN, demonstrating that NiFeCpN decomposes into the mononuclear NiL species and Fe-based complexes during the catalytic process. Therefore, this NiFe complex is not stable under these conditions.

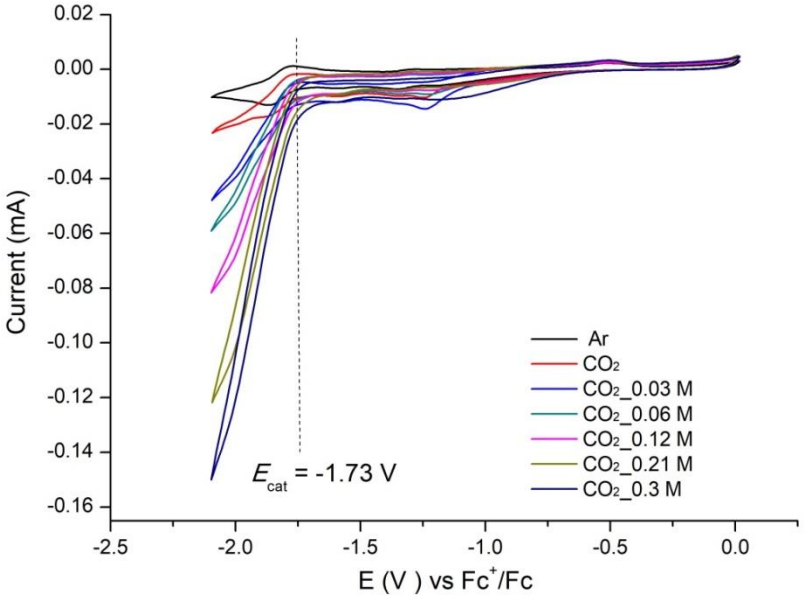

Figure 4.4 CVs of TFE at different concentrations with NiFeCpN (0.57 mM) and without NiFeCpN (bottom) in MeCN solution with CO_2 or Ar, 0.1 M n-Bu_4NClO_4, on a glassy carbon electrode at *v* = 100 mV/s.

4.2.2 Heterogeneous catalytic activity of NiFeCpN for CO_2 reduction

It is worth noting that some homogeneous catalysts have provided good catalytic performance but they lack stability under electrocatalytic conditions.[144, 145] A promising strategy developed by several groups relies on surface immobilization. It has demonstrated that considerable improvement in the stability of the electrocatalysts in heterogeneous catalysis can be reached.[146] As mentioned above, the NiFeCpN complex is not stable under homogeneous catalytic conditions. In this context, the NiFeCpN complex has been immobilized on EPG electrodes by physical absorption to form a hybrid electrocatalyst NiFeCpN/EPG.

The CVs of the NiFeCpN/EPG have been carried out in phosphate buffer aqueous solutions at pH 4.05 (**Figure 4.5**). Both graphite and NiFeCpN/EPG display a reduction process around at −1.12 V vs Ag/AgCl under Ar atmosphere, corresponding to a proton reduction catalytic event. After CO_2 bubbling into the electrolyte solution, the CV of NiFeCpN/EPG exhibits a positive shift from −1.18 V to −1.14 V vs Ag/AgCl (measured at half-wave), indicating that an electrocatalytic process occurs under these conditions.

Controlled potential electrolysis (CPE) experiments have been carried out at −1.3 V at pH 4.05 to identify the generated products. The headspace gas of the CPE cell is then analyzed by gas chromatography (GC). Two gas products, H_2 and CH_4 are observed with a large excess of H_2 (FE = 66%) and a small amount of CH_4 (FE = 1.3%). No other products have been detected in the electrolyte solution by liquid chromatography. As previously mentioned (**see section 1.2**), proton reduction is a competitive reaction to CO_2 reduction, and hydrogen can also be produced during CO_2 reduction. For this hybrid catalyst, these acidic conditions can also favor H_2 production with respect to CO_2 reduction.

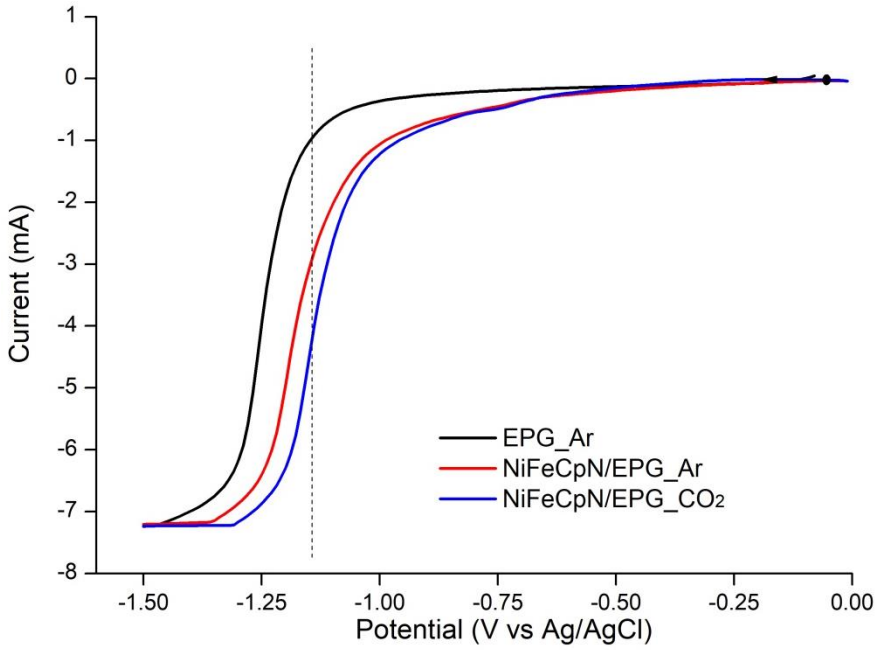

Figure 4.5 CVs of a NiFeCpN/EPG (13 mm diameter, red line under Ar, blue line under CO_2) and a pristine EPG recorded at pH 4 at *v* = 100 mV/s in 0.1 M phosphate buffer aqueous electrolyte under Ar with Ag/AgCl (3.5M KCl) reference and Pt counter electrodes.

4.2.3 Homogeneous catalytic activity of CoFeCpNH for CO_2 reduction

As mentioned above, the NiFeCpN complex has the ability to catalyze CO_2 reduction under homogeneous and heterogeneous conditions. The CoFeCpNH analog has also been tested to catalyze CO_2 reduction. The CVs of CoFeCpNH have been recorded in DMF solutions. In the presence of TFE, it is observed that the current intensity displays a slightly increasing below −1.80 V vs $Fc^{+/0}$ under Ar gas (**Figure 4.6**). After CO_2 bubbling into the electrolyte solution, the CV of CoFeCpNH exhibits a larger current intensity below −1.80 V, indicating that an electrocatalytic process occurs under these conditions. The onset catalytic potential is observed below −1.60 V vs $Fc^{+/0}$. Interestingly, the anodic process is observed at −1.00 V, and shifts to −0.88 V after bubbling CO_2. It is possible that new species are generated during the catalytic process.[147] Moreover, the current intensity of the catalytic wave continuously increases by increasing the amount of TFE (**Figure 4.7**).

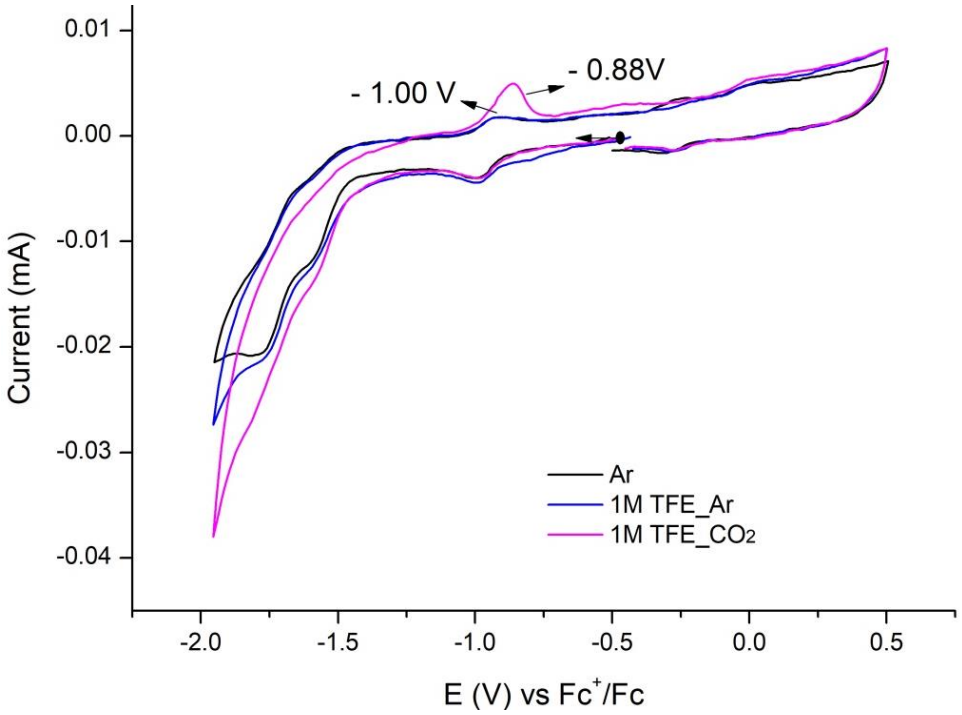

Figure 4.6 CVs of CoFeCpNH (0.43 mM) under Ar (black line) and in the presence of 1 M of TFE under Ar (blue line) and CO_2 (pink line). Conditions: 0.1 M n-Bu_4NClO_4 in DMF, on a glassy carbon electrode at *v* = 100 mV/s.

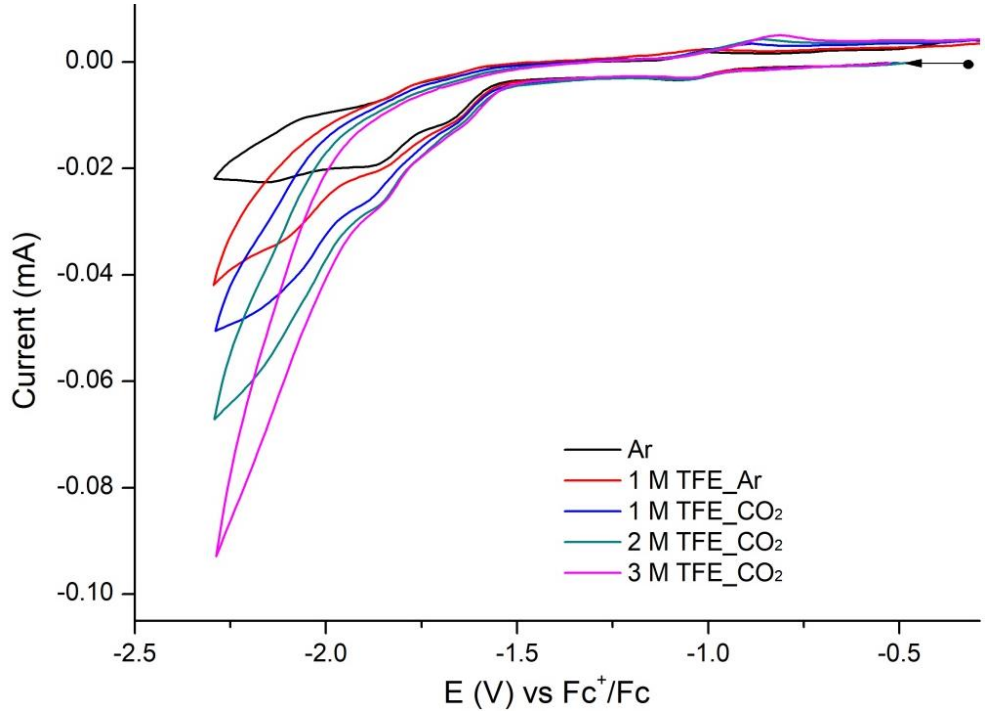

Figure 4.7 CVs of various amounts of TFE with CoFeCpNH (0.43 mM) in a DMF solution under CO_2 or Ar, 0.1 M n-Bu_4NClO_4, on a glassy carbon electrode at *v* = 100 mV/s.

In the presence of CoFeCpNH, a more positive catalytic potential and a larger current intensity with respect to mononuclear FeCpNH are observed indicating better activity

of the dinuclear complex (**Figure 4.8**). Compared to $Co^{II}Fe^{II}Cp$, CoFeCpNH also displays a more positive catalytic potential, indicating that the amine group promotes the activity for CO_2 reduction and plays an important role during the catalytic process. In the case of NiFeCpN, its onset catalytic potential (−1.73 V) is more negative than for CoFeCpNH (−1.60 V), indicating that the presence of Co is more favorable for CO_2 reduction.

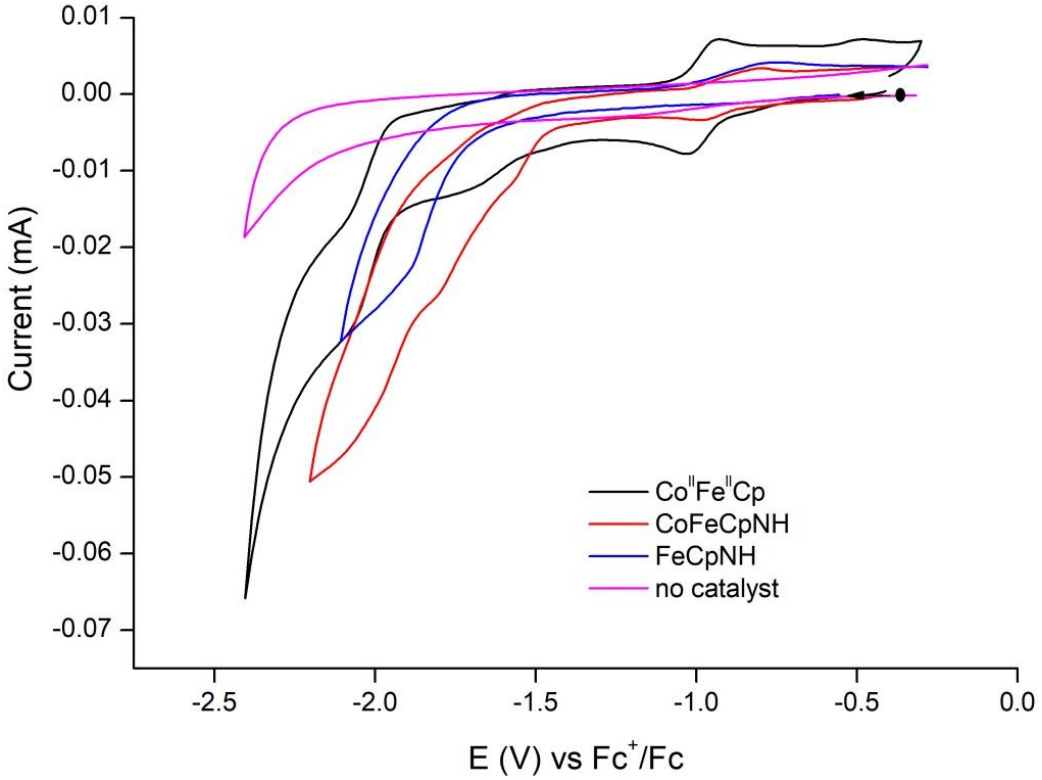

Figure 4.8 CVs of 1 M TFE under statured CO_2 without catalyst (pink line), in the presence of $Co^{II}Fe^{II}Cp$ (1 mM, black line), CoFeCpNH (0.43 mM, red line) and FeCpNH (0.68 mM, blue line) in DMF solution, 0.1 M n-Bu_4NClO_4, on a glassy carbon electrode at v = 100 mV/s.

4.3 Conclusion

The NiFeCpN and CoFeCpNH complexes have the ability to catalyze CO_2 reduction under homogeneous conditions.

CoFeCpNH (E_{cat} = −1.61 V) displays a more positive onset catalytic potential than NiFeCpN (E_{cat} = −1.73 V), indicating that the presence of a Co ion favors CO_2 reduction under these conditions.

CoFeCpNH has a better activity for CO_2 reduction than $Co^{II}Fe^{II}Cp$, indicating the role of the pendant amine during the catalytic process.

The NiFeCpN complex also has the ability to catalyze CO_2 reduction under

heterogeneous conditions, after its immobilization on graphite. Only two products, H_2 (FE = 66%) and CH_4 (FE = 1.3%), are produced at pH = 4.05. However, these acidic conditions favor the competitive H_2 production reaction over CO_2 reduction.

The presence of the pendant amine is beneficial for promoting electrocatalytic activity for CO_2 reduction. However, it is necessary to understand the catalytic mechanism to tune the structure of the catalyst in a rational manner for better catalytic selectivity.

Chapter 5 Modulation of the electrocatalytic activity for H_2 production with bio-inspired NiFe complexes containing P-based ligands

5.1 Introduction

Recently, molecular H_2 has been considered an ideal energy carrier to replace fossil fuels in order to alleviate the current energy shortage.[148] In nature, [NiFe] H_2ase is a class of biological enzymes that catalyze the reversible interconversion of H_2 with protons and electrons[8]. The active site of the [NiFe] H_2ase has a {Ni(cysteinate)$_4$} center, which is linked via two of its cysteine ligands to a {$Fe^{II}(CN)_2(CO)$} unit.[15, 16] Structural and functional models of [NiFe] H_2ase have been prepared for H_2 production.

Based on the active site of the [NiFe] H_2ase, dithiolate [ML^{N2S2}] (M= Ni and Fe) complexes have been used as a metal-organic backbone for the design of dinuclear bio-inspired complexes in which two S atoms are bridging a second metal, i.e. Fe, to form complexes with a M(μ-S)$_2$Fe core.[32-34, 76, 149-152] Generally, the Fe moiety is composed by $[CpFe(CO)]^+$ or $[Cp^*Fe(CO)]^+$ (**Figure 5.1**). In addition, these bio-inspired complexes have revealed an efficient electrocatalytic activity for H_2 production.

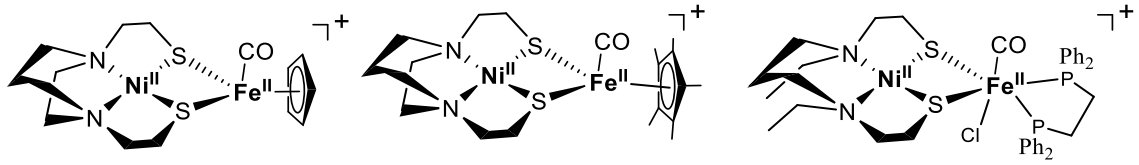

Figure 5.1 Structures of the different bio-inspired electrocatalysts.

As previously described, the $Ni^{II}Fe^{II}Cp$[33] and $Ni^{II}Fe^{II}Cp^*$[34] complexes display similar activity for H_2 production under electrocatalytic conditions. Experiments and DFT calculations have confirmed that the H_2 production activity is dominated by the presence of the non-innocent bipyridine ligand coordinated to the Ni ion and that the Cp or Cp* ligand of the Fe site does not contribute notably. On the other hand, diphosphine ligands can act as donor ligands and have been employed to synthesize bio-inspired NiFe complexes displaying good electrocatalytic activity for H_2 production (**Figure 5.1**).[7, 74, 153]

Inspired by these results, this chapter focuses on the synthesis of a targeted NiFe complex, in which the Fe is coordinated to a diphosphine ligand. Our objective is to replace the Cp ligand in the $Ni^{II}Fe^{II}Cp$ complex with a diphosphine ligand (i.e., 1,2-bis(diphenyl phosphino)ethylene: dppv and 1,2-bis(diphenylphosphino)ethane:

dppe) with the nickel site keeping unchanged.

5.2 Result and discussion

5.2.1 Synthesis and characterization of $[L^{N2S2}NiFe(CO)(dppv)](BF_4)_2$

In order to synthesize the $[L^{N2S2}NiFe(CO)(dppv)](BF_4)_2$ [NiFe(dppv)] complex, $[FeCl_2(CO)_2dppv]$ should be synthesized first. The synthetic route to obtain $[FeCl_2(CO)_2dppv]$ is shown in **Figure 5.2**.[154] CO gas is bubbled into an acetone solution of $FeCl_2$ for about 20 min. Then a THF solution of dppv ligand is added to give an orange solution. CO gas is then bubbled into the reaction solution for about 5 h and an orange powder is recovered. The IR spectrum of the product displays features at 1966 cm^{-1} and 1996 cm^{-1} in CH_2Cl_2. In the ESI-MS spectrum of the product in CH_2Cl_2, a peak at m/z = 911.26 is observed, assigned to the $[Fe^{II}Cl(CO)(dppv)_2]^+$ complex (**Figure 5.3**). Therefore, the $[FeCl_2(CO)_2dppv]$ complex is not obtained under these experimental conditions.

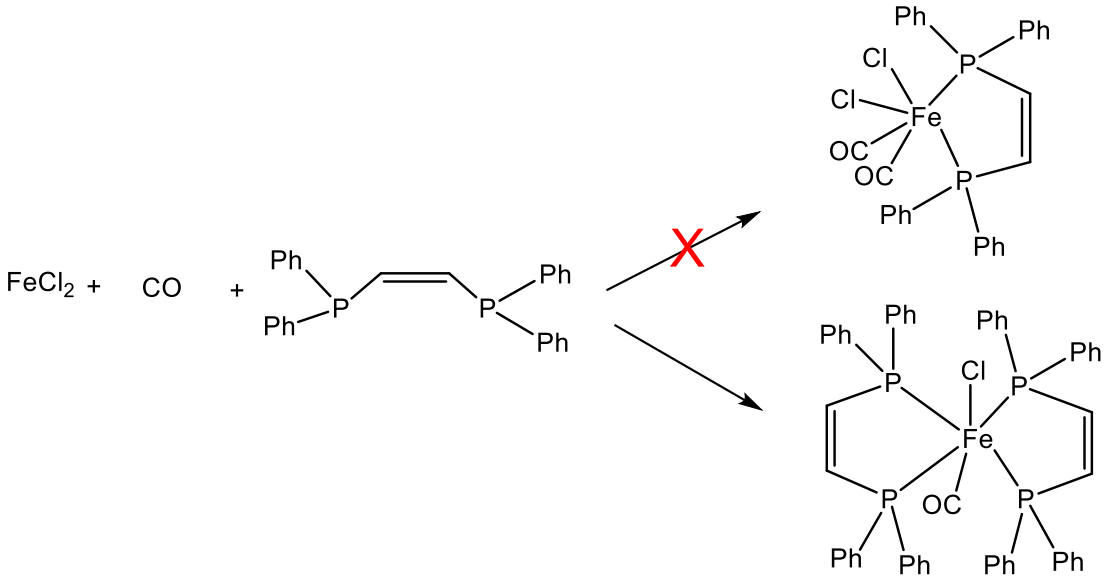

Figure 5.2 Reaction between $FeCl_2$ and dppv under CO atmosphere.

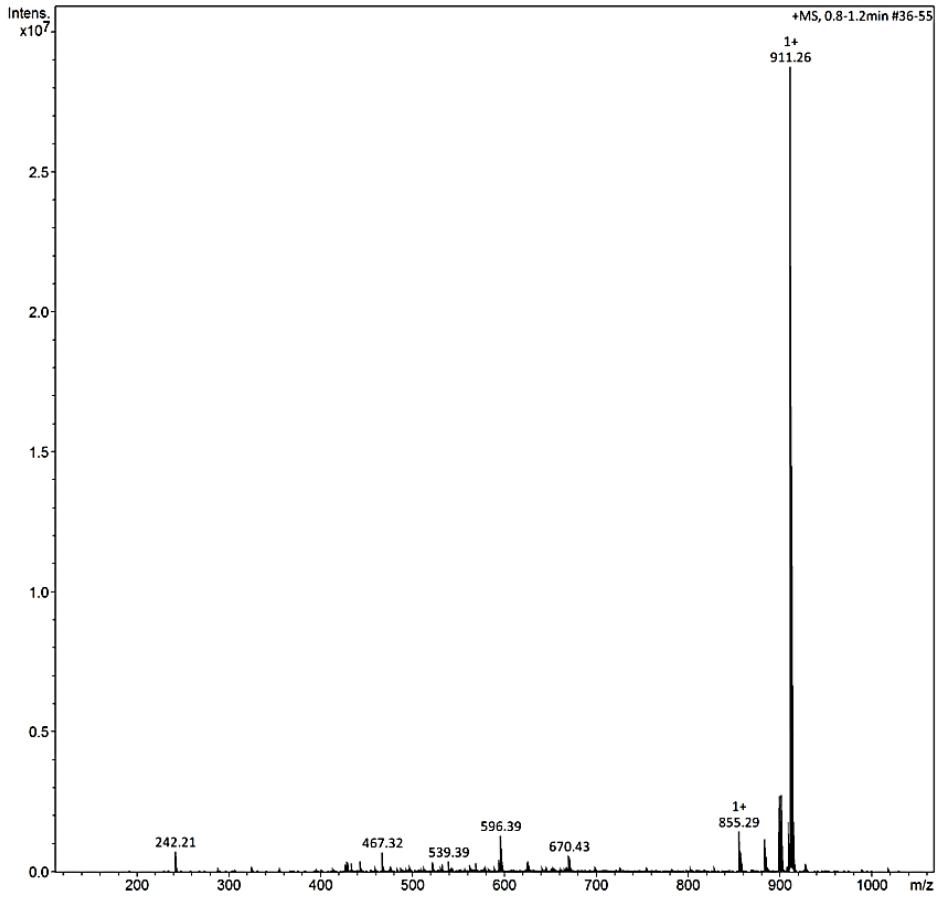

Figure 5.3 ESI-MS of the $[Fe^{II}Cl(CO)(dppv)_2]^+$ complex in CH_2Cl_2.

Given that the flow rate of CO gas may affect the synthesis, the same reaction is then attempted a second time with an increase in the flow rate of CO gas (**Figure 5.2**). The IR spectrum of the corresponding product displays two vibrations at 2019 cm^{-1} and 2053 cm^{-1} in CH_2Cl_2. The ESI-MS spectrum of the product in CH_2Cl_2 displays a peak at m/z = 911.24, assigned to the $[Fe^{II}Cl(CO)(dppv)_2]^+$ complex, but no peak corresponding to the $[FeCl_2(CO)_2dppv]$ complex is observed. $[FeCl_2(CO)_2dppv]$ could not be obtained under these conditions.

We thus hypothesized that the time of CO bubbling into the reaction solution may be too short, which may be unfavorable for the production of the dichloride Fe complex. Therefore, on the basis of the previous experiments, CO gas is bubbled into an acetone solution of $FeCl_2$ for about 90 min. The IR spectrum of the product is observed at 2015 cm^{-1} and 2052 cm^{-1} in CH_2Cl_2. In the ESI-MS spectrum, a peak is still observed at m/z = 911.26, but none corresponding to the $[FeCl_2(CO)_2dppv]$ is seen. Therefore, the $[FeCl_2(CO)_2dppv]$ could not be formed under these experimental conditions.

Then, we tried to use the anhydrous $FeBr_2$ salt instead of the $FeCl_2$ one to synthesize the $[FeBr_2(CO)_2dppv]$ in a THF solution (**Figure 5.4**).[155] $FeBr_2$ reacts with the dppv ligand in THF under CO atmosphere to form the $[FeBr_2(CO)_2dppv]$ complex. In the ESI-MS spectrum of the crude product in CH_2Cl_2, a peak is observed at m/z = 670.19,

assigned to the [$FeBr_2(CO)_2$dppv - $2Br^-$ + $2H^+$]. The crude product is purified by silica gel column chromatography using CH_2Cl_2 as an eluent. The IR spectrum of the purified complex shows that features assigned to CO vibrations are at 2019 cm^{-1} and 2053 cm^{-1} in CH_2Cl_2 (**Figure 5.5**). These data confirm that the [$FeBr_2(CO)_2$dppv] can be formed under these conditions.

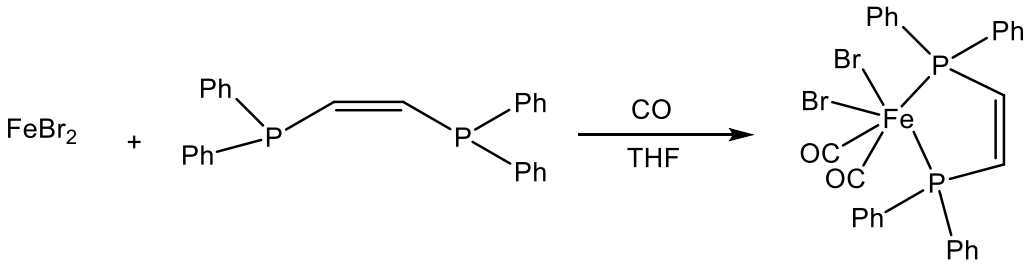

Figure 5.4 Synthetic route for $FeBr_2(CO)_2$dppv complex.

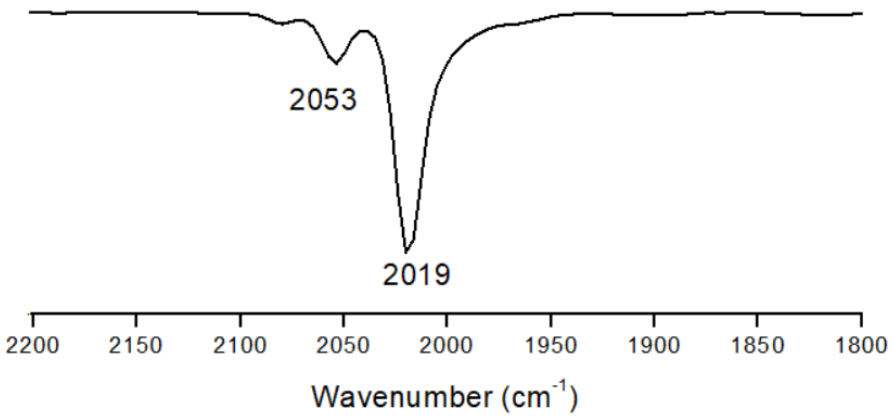

Figure 5.5 IR spectrum for the [$FeBr_2(CO)_2$dppv] complex.

NiL is then added to a CH_2Cl_2 solution of [$FeBr_2(CO)_2$dppv] in the presence of $NaBF_4$. After overnight, the unique two CO vibrations observed in the IR spectrum, are those of the mononuclear [$FeBr_2(CO)_2$dppv] complex. Besides, the UV-vis spectrum displays two transitions at 501 nm and 560 nm, which belong to NiL. Therefore, no reaction occurs between the Fe and Ni units under these conditions (**Figure 5.6**).

The halides may have an impact on the synthesis of the dinuclear complex. Then, $AgBF_4$ is added to the above solution to remove Br^-. The IR spectrum of the resulting solution displays many CO vibrations at 1812 cm^{-1}, 1890 cm^{-1}, 1966 cm^{-1}, 2004 cm^{-1} and 2054 cm^{-1}. In the ESI-MS spectrum of the crude product in CH_2Cl_2 (**Figure 5.7**), two main peaks are observed at m/z = 901.24 and 1381.33, assigned to [$Ag(dppv)_2$ + H^+][156] and $[Ag(NiL)_2]^+$, respectively. Therefore, the desired NiFe complex could not be obtained with this procedure. However, we can observe that the addition of an Ag salt has a strong impact on the reaction with the synthesis of several complexes.

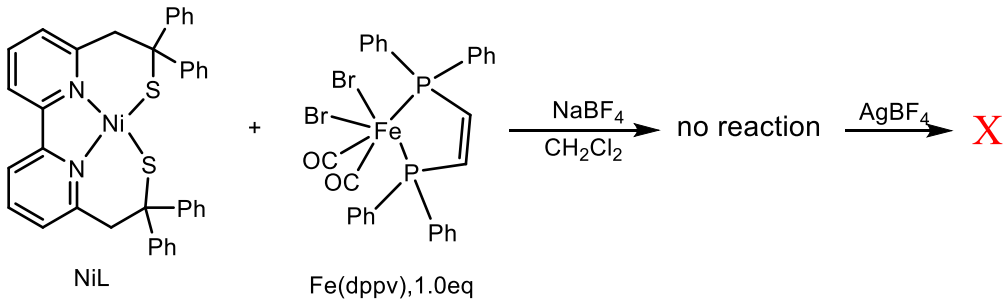

Figure 5.6 Reaction of the NiL and $[FeBr_2(CO)_2dppv]$ in MeCN.

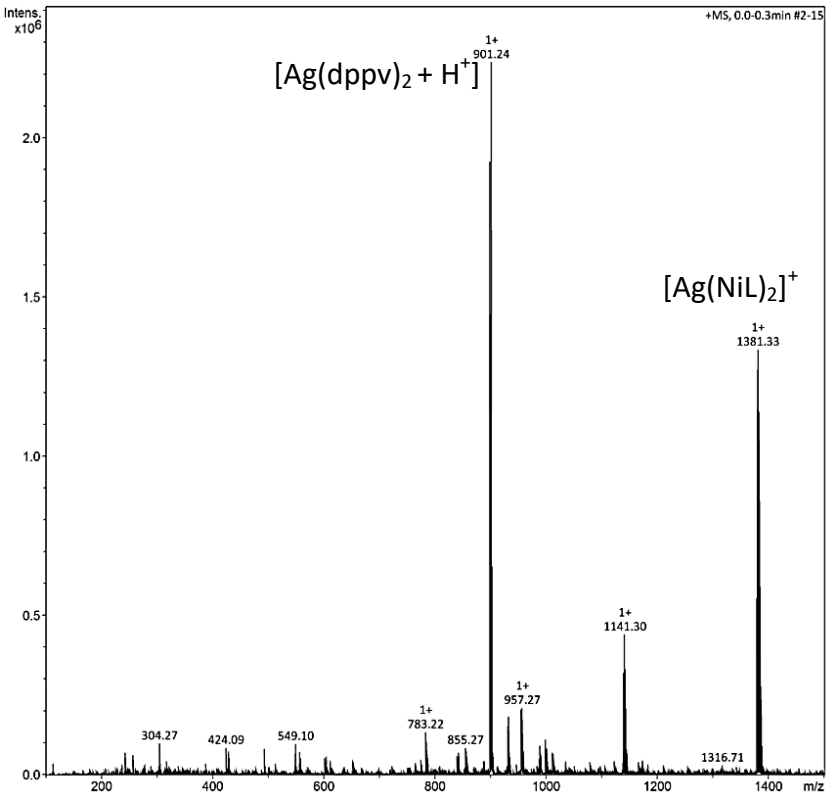

Figure 5.7 ESI-MS of the $[Ag(dppv)_2 + H^+]$ and $[Ag(NiL)_2]^+$ complexes in CH_2Cl_2.

In a next step, we tested to remove Br^- of $[FeBr_2(CO)_2dppv]$ by adding $AgBF_4$ prior to the reaction with NiL (**Figure 5.8**). $AgBF_4$ is added to a CH_2Cl_2 solution of $[FeBr_2(CO)_2dppv]$ and a precipitate appears that can be removed. In the IR spectrum of the corresponding solution, the two observed CO vibrations shift from 2019 cm^{-1} and 2053 cm^{-1} to 2033 cm^{-1} and 2075 cm^{-1}. It strongly suggests that Br^- has been removed from $[FeBr_2(CO)_2dppv]$. Then NiL is added to a CH_2Cl_2 solution of $[Fe(CO)_2dppv]^{2+}$, resulting in a dark brown solution. The IR spectrum of the resulting solution displays many CO vibrations at 1812cm^{-1}, 1890 cm^{-1}, 1966 cm^{-1}, 2004 cm^{-1} and 2054 cm^{-1}. In the ESI-MS spectrum of the crude product in CH_2Cl_2, a peak is observed at m/z = 901.24, assigned to $[Ag(dppv)_2 + H^+]$ (**Figure 5.9**), while the observed peak at m/z = 901.24 is assigned to an unknown complex. The expected peak corresponding to the targeted complex cannot be observed, evidencing that the

desired NiFe complex cannot be generated under these conditions.

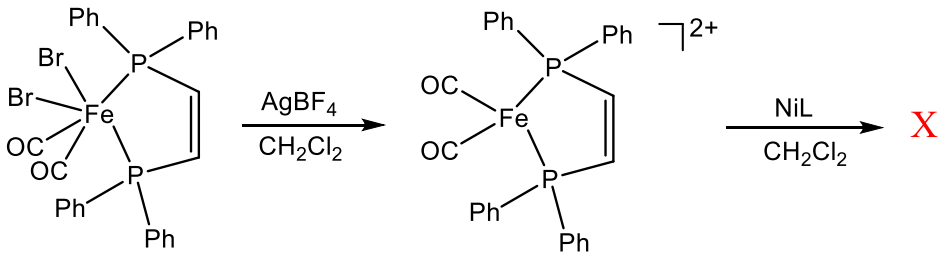

Figure 5.8 Synthetic route for the [NiFe(dppv)] complex.

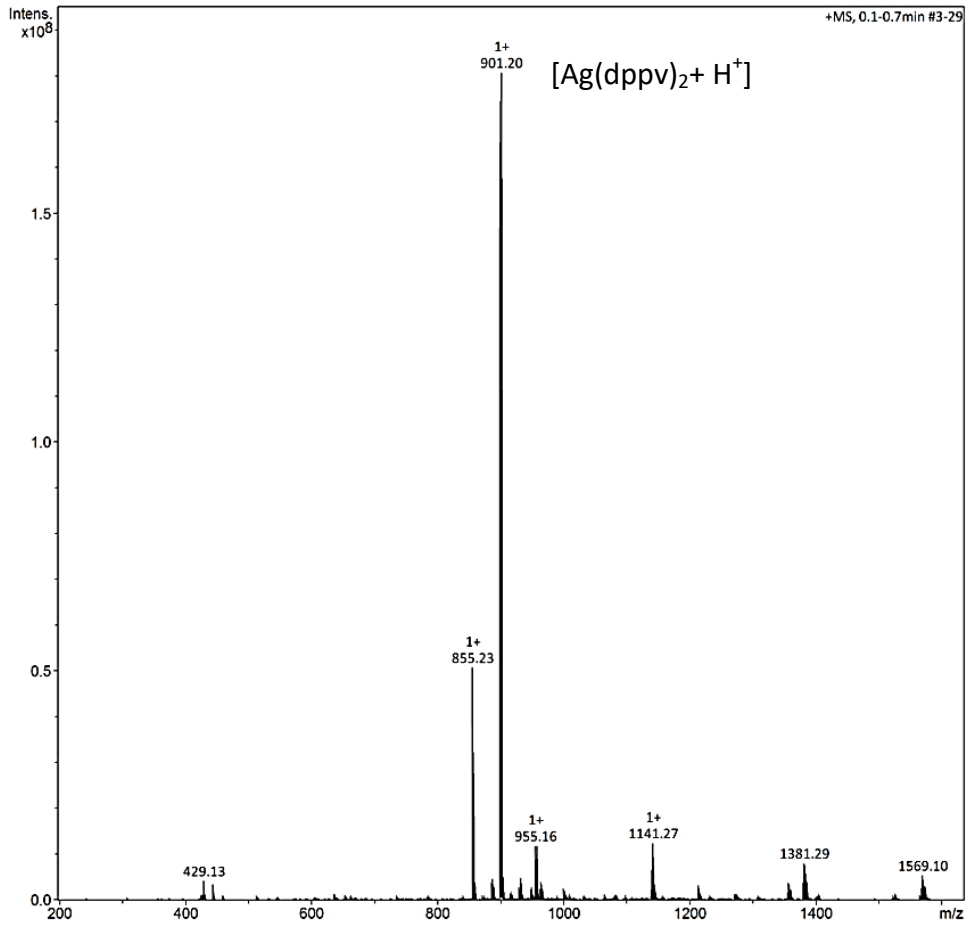

Figure 5.9 ESI-MS of the $[Ag(dppv)_2 + H^+]$ complex in CH_2Cl_2.

Due to the possible influence of the solvents on the synthesis, we tried to remove Br^- from the $[FeBr_2(CO)_2dppv]$ complex by adding $AgBF_4$ in MeCN instead of CH_2Cl_2 (**Figure 5.10**). The main CO vibration shifts from 2014 cm^{-1} to 2005 cm^{-1} in the IR spectrum. However, the peak at m/z = 901.23, assigned to $[Ag(dppv)_2 + H^+]$, is still observed in ESI-MS spectrum. Therefore, Ag still has an influence during the synthesis process.

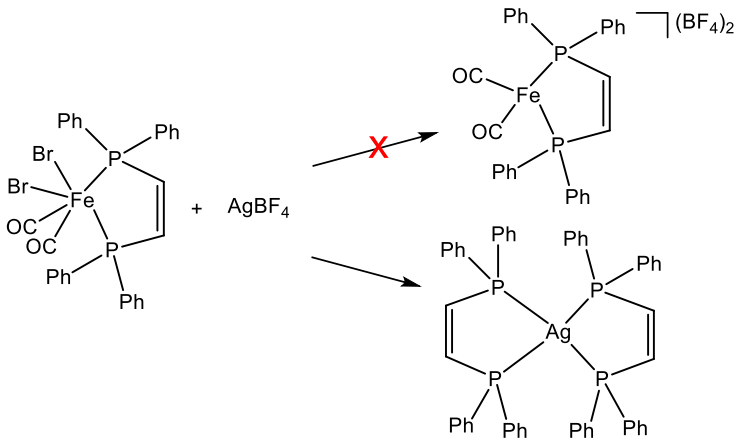

Figure 5.10 Reaction between $[FeBr_2(CO)_2dppv]$ and $AgBF_4$ in MeCN.

Another reaction procedure has been applied, i.e. NiL reacts with the P-based Fe complex under CO atmosphere.[152] In this context, the $[FeCl_2dppe]$ complex is first synthesize (**Figure 5.11**).[157] In the APCI-MS (APCI: atmospheric pressure chemical ionization) spectrum of the crude solution in MeCN, two peaks have been observed at m/z = 431.21 and 556.09, assigned to $[dppe+O_2+H^+]$ and $[FeCl_2dppe+O_2+H^+]$, respectively (**Figure 5.12**). This data confirms that the $[FeCl_2dppe]$ can be formed under these conditions.

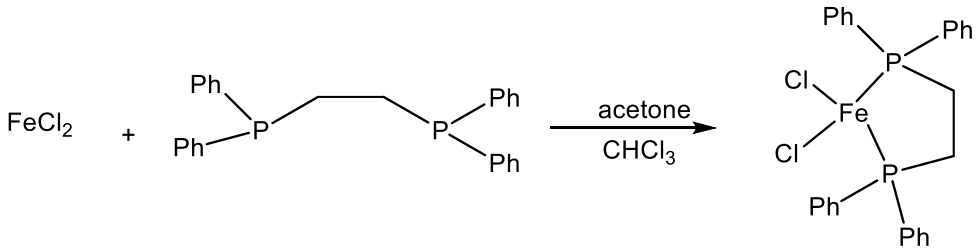

Figure 5.11 Synthesis of the $[FeCl_2dppe]$ complex.

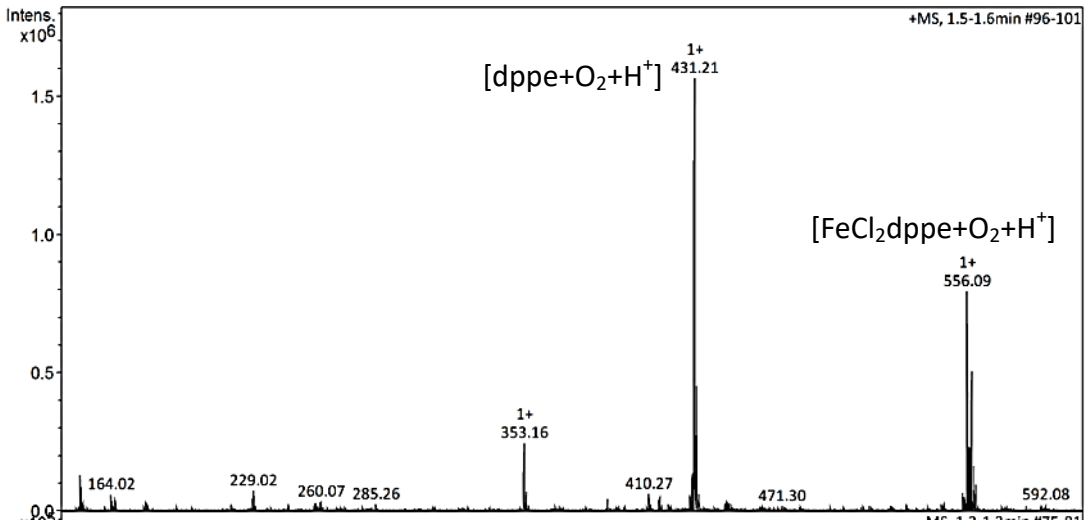

Figure 5.12 APCI-MS spectrum of the $[FeCl_2dppe]$ complex in MeCN.

NiL then reacts with $[FeCl_2dppe]$ in CH_2Cl_2 solution under CO atmosphere (**Figure**

5.13). After the reaction, no CO vibrations are observed in the expected range in the IR spectrum recorded on the reaction solution. The ESI-MS spectrum of the reaction solution does not display the expected feature for the targeted NiFe complex (**Figure 5.14**).

DMF has also been tested as a solvent instead of CH_2Cl_2 (**Figure 5.13**). After one day, no changes are observed in the UV-vis spectrum and two transitions are observed at 501 nm and 563 nm, attributed to the NiL complex. Besides, no CO vibrations are observed in the expected range in the IR spectrum of the reaction solution. No reaction occurs under these synthetic conditions.

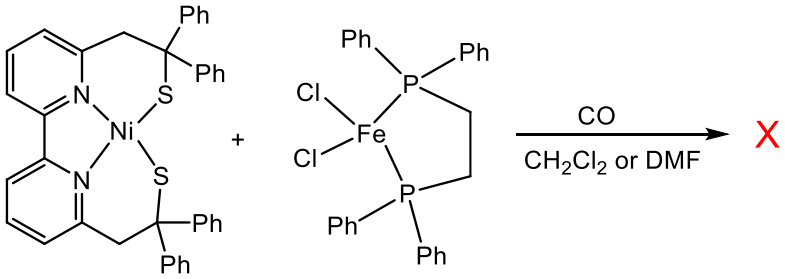

Figure 5.13 Reactions of the [$FeCl_2$dppe] and $AgBF_4$ in CH_2Cl_2.

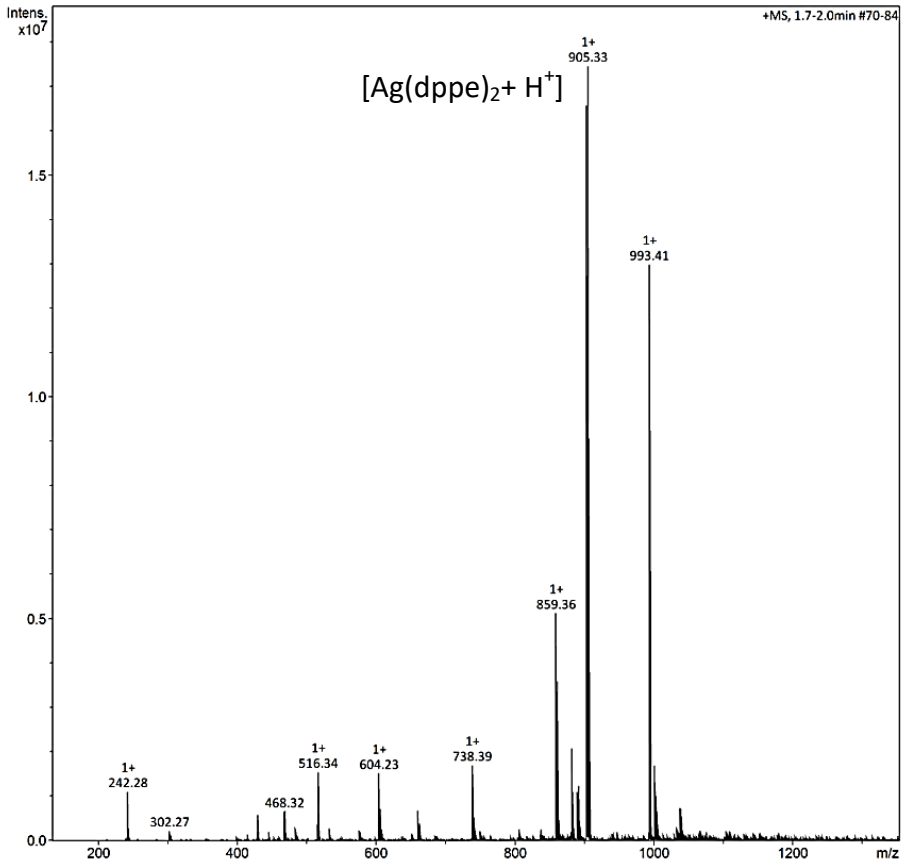

Figure 5.14 ESI-MS of the [$Ag(dppe)_2 + H^+$] complex in CH_2Cl_2.

5.3 Conclusion

We did not succeed to synthesize P-based NiFe complexes even if many different synthetic strategies have been tested. The possible reason is that both NiL and dppv contain four phenyl groups hindering the reaction. Besides, Ag is not a good choice during the synthesis since it impacts the structure of the resulting generated complexes by coordinating units.

Chapter 6 Summary and Perspective

6.1 Summary

Hydrogenases are organometallic enzymes that catalyze reversibly the oxidation of hydrogen into protons and electrons. In this context, many bio-inspired FeFe and NiFe complexes have been developed to catalyze H_2 production. Besides, some FeFe models are also able to catalyze CO_2 reduction. Inspired by these, this thesis has described the design and synthesis of original bio-inspired dinuclear MFe (M= Ni and Co) complexes to modulate electrocatalytic activity for H_2 production and CO_2 reduction.

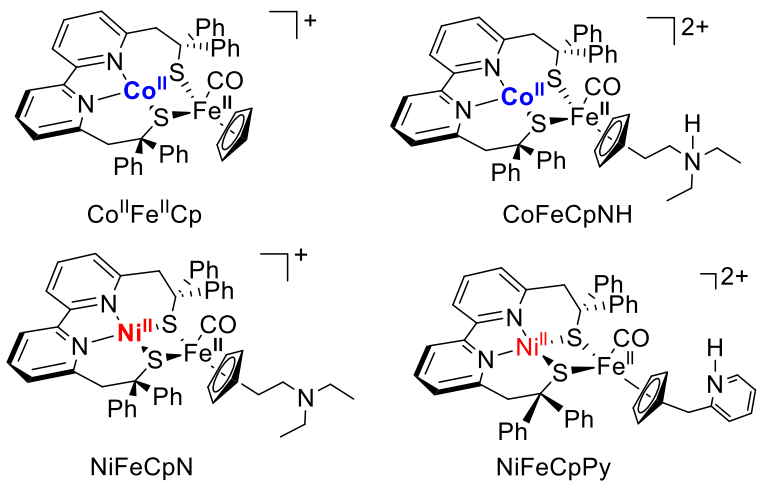

Figure 6.1 Structures of the different bio-inspired complexes investigated during this work.

The heterodinuclear $Co^{II}Fe^{II}Cp$ complex (**Figure 6.1**) has been presented in Chapter 2. $Co^{II}Fe^{II}Cp$ is the easiest to reduce by one electron with respect to the other MFe analogs. The corresponding one-electron reduced species ($Co^{I}Fe^{II}Cp$) has been isolated and characterized. Unexpectedly, this CoFe complex is not active to produce H_2 electrocatalytically, while the parent $Ni^{II}Fe^{II}$ and $Fe^{II}Fe^{II}$ complexes display good performance. Interestingly, when a pendant amine is added in the second coordination sphere of the $Co^{II}Fe^{II}Cp$ complex (**Figure 6.1**), it becomes active for electrocatalytic production of H_2 demonstrating that the pendant amine can act as a proton relay. It has been described in Chapter 3. In addition, it has been experimentally observed that when a weak acid (Et_3NH^+) is present, the electrocatalysts are reduced first; while when a strong acid (HBF_4) is used, the electrocatalysts are first protonated rather than being reduced, demonstrating the impact of the pK_a of the acid on the catalytic mechanism.

Chapter 3 also presented two new NiFe complexes bearing pendant amine, i.e. NiFeCpPy and NiFeCpN (**Figure 6.1**). The NiFeCpPy is less stable than NiFeCpN due to

the easy loss of the last CO ligand. NiFeCpN displays better performance both under homogeneous conditions in MeCN in the presence of Et_3NH^+, and under heterogeneous conditions in an acidic aqueous solution (pH = 4) after its immobilization on a graphite electrode. These data confirm that the pendant amine can play an important role in the electrocatalytic activity for H_2 production by acting as a proton relay and thus enhancing their efficiency.

These NiFe and CoFe complexes with the pendant amine have also been tested toward electrocatalytic activity for CO_2 reduction in the presence of TFE in MeCN or DMF in Chapter 4. The CoFe complex with the pendant amine displays a more positive catalytic potential than the NiFeCpN and $Co^{II}Fe^{II}Cp$ complexes. In the case of NiFeCpN, the activity for CO_2 reduction has been estimated after its immobilization on a graphite electrode. In an acidic aqueous solution (pH = 4), only two products are generated: H_2 (FE = 66%) and CH_4 (FE = 1.3%) as the unique C-based product.

6.2 Perspective

Surprisingly, the dinuclear $Co^{II}Fe^{II}Cp$ complex is not electrocatalytic active for H_2 production in DMF. The investigation of the $Ni^{II}Fe^{II}Cp$ and $Fe^{II}Fe^{II}Cp$ complexes in MeCN seems to show that the key factor controlling their reactivity is the bipyridine unit, not the nature of the metal. Therefore, the origin of this lack of H_2 production reactivity in $Co^{II}Fe^{II}Cp$ is unclear. DFT calculations are currently performed to explain this difference in reactivity.

In order to modify the electrocatalytic activity of this series of MFeCp (M= Ni, Fe and Co) complexes, a pendant amine has been added in the parent $M^{II}Fe^{II}$ complex (M= Ni and Co) to synthesize a new family of MFeCpN complexes for H_2 production and CO_2 reduction under homogeneous or heterogeneous conditions. However, the one-electron reduced species $M^{I}Fe^{II}CpN$ cannot be isolated and characterized. Low-temperature techniques have been employed to stabilize these reduced MFeCpN complexes to characterize intermediates unsuccessfully. DFT calculations will be performed to predict the structure of these intermediate states, which would be helpful to elucidate the catalytic mechanism and thus understand the role of the pendant amine, whether or not a hydride species is formed after its protonation.

For the NiFeCpN complex, more basic conditions should be tried to catalyze CO_2 reduction under heterogeneous conditions, as current experiments show that acidic conditions (pH = 4) are more favorable for H_2 production than for CO_2 reduction. Based on the experiments, CoFeCpNH has better activity than NiFeCpN for CO_2 reduction under homogeneous conditions. Therefore, it will also be investigated for its activity towards CO_2 reduction under heterogeneous conditions and compared with NiFeCpN.

Inspired by the MFeCpN complexes (M = Ni and Co), the FeFeCpNH bearing a pendant amine (**Figure 6.2**) should be synthesized to act as a catalyst for H_2 production and CO_2 reduction, to study the effect of the nature of the metal on

electrocatalytic activity. Indeed, in the case of the FeFeCp complex, the one-electron reduced species is a mixed valent species, contrarily to $Co^{II}Fe^{II}Cp$ and $Ni^{II}Fe^{II}Cp$ for which the reduction occurs mainly on the Co and Ni sites. It would be interesting to see if this difference can impact the efficiency and /or the mechanism with the presence of the pendant amine.

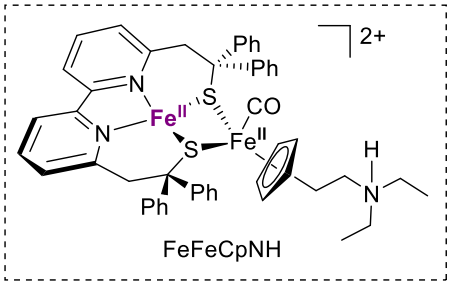

Figure 6.2 Structure of the FeFeCpNH complex.

In Chapter 5, we have targeted the synthesis of a NiFe complex with P-based ligands. Many different synthetic strategies have been attempted, but unsuccessfully. It may be that since each NiL and Fedppv unit contains four phenyl groups, the steric hindrance is too large to allow the reaction to occur.

In future work, the FeFeSH complex (**Figure 6.2**) will replace NiL to synthesize the FeFe(dppv), because this FeFeSH complex containing eight phenyl groups has already been isolated. Alternatively, diphosphine ligands with alkyl groups, such as 1,2-bis(dimethylphosphino)ethane (dmpe), with less steric hindrance could be selected to synthesize dinuclear MFe complexes (**Figure 6.2**).

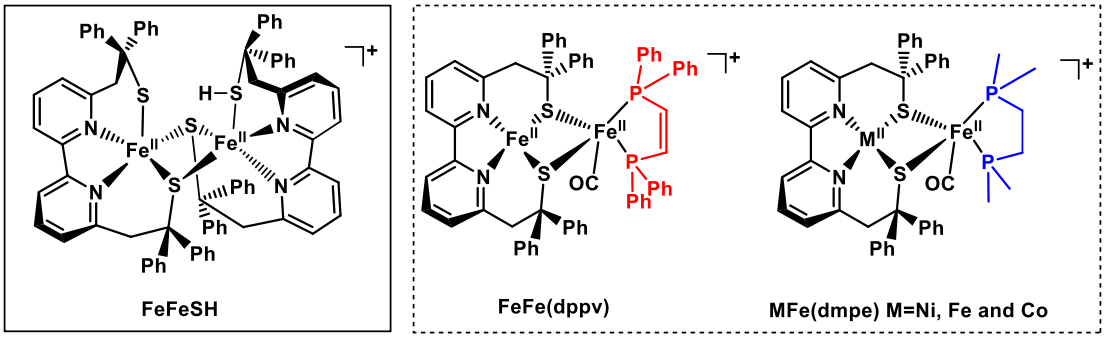

Figure 6.2 Structures of the FeFeSH, FeFe(dppv) and MFe(dmpe) (M = Ni, Fe and Co) complexes.

Appendix

General reagents and Materials

All common reagents are purchased and used as received without further purification. Edge Plane Graphite (EPG) electrodes are purchased from Aldrich. All solvents are distilled and degassed with Ar before use in experiments. All experiments are prepared under Ar atmosphere in Schlenk tubes or gloveboxes. The $[Fe^{II}(MeCN)_2(CO)Cp]BF_4$ complex is prepared according to previously published methods.[117, 158]

Characterization methods

IR measurements are recorded as the average of 4 scans on an Agilent Cary 630 FTIR spectrometer equipped with an attachment for diamond-attenuated total reflectance measurements. Absorption spectra are recorded on a ZEISS MC5601 spectrophotometer in a quartz cell (path length: 10 mm). MS experiments are performed in positive ionization mode on a Bruker Esquire 3000 Plus ion trap spectrometer.

X-band EPR solid state or frozen solution samples are prepared in the glove box in a quartz EPR tube. Spectra were acquired on a Bruker EMX instrument equipped with the ER-4192 ST Bruker cavity and an ER-4131 VT probe. Acquisition parameters: 15 dB, 100 K underflow of liquid nitrogen.

Homogeneous Electrochemistry

Cyclic voltammograms are recorded in a glove box (Ar) equipped with a potentiostat (Metrohm Autolab PGSTAT100N). The following experimental conditions are used: electrolyte: 0.1 M n-Bu_4NClO_4 in DMF or MeCN; reference electrode: $Ag/AgNO_3$ in the electrolyte; counter electrode: Pt wire; scan rate: 100 mV/s; working electrode: 3 mm diameter glassy carbon disk polished with 2 mm diamond paste. All potentials are internally calibrated to the $Fc^{+/0}$ couple using freshly sublimed ferrocene (E_{pa}, anodic peak potential; E_{pc}, cathodic peak potential; $E_{1/2} = (E_{pa} + E_{pc})/2$; $\Delta E_p = E_{pa} - E_{pc}$).

Heterogeneous Electrochemistry

Cyclic voltammograms are recorded on a potentiostat using the modified graphite electrode in 0.1 M phosphate buffer aqueous at different pH values, with the reference electrode Ag/AgCl (3.5 M KCl), with counter electrode Pt plate in 0.1 M KPF_6. The aqueous media is deaerated by bubbling Ar or CO_2 prior to recording the CV as appropriate.

The thermodynamic potential for H^+/H_2 couple at a particular pH is determined using the following equation: $E^o_{H^+/H_2} = -0.059 \times pH$

The potentials are converted to the reversible hydrogen electrode (RHE) scale using

the following equation: $E_{RHE} = E_{Ag/AgCl} + 0.197\ V + pH \times 0.059\ V$; $E_{RHE} = E_{SHE} + pH \times 0.059\ V$

Controlled potential electrolysis (CPE) and gas collection

After deaerating the aqueous media with the appropriate gas (Ar or CO_2), the controlled potential electrolysis is performed on a potentiostat using the modified graphite electrode at different potentials in a well-sealed three-electrode cell (25 ml) for 3 hours. The volume of the solution is 12 ml and hence the headspace 13 ml. The gas evolved is analyzed using GC/MS gas chromatography (Perkin Elmer Clarus 560) instrument with a thermal conductivity detector.

DFT details

All complexes were optimized to a minimum with the Gaussian09[159] program using the BP86[160, 161] (and B3P86)[161, 162] functional and a def2-TZVP[163, 164] basis set. Frequency calculations were performed to ensure that the complexes were optimized to their respective minima. Implicit solvation was performed using the IEFPCM scheme.[165]

To calculate theoretically the redox potential of the complex couple ($[Co^{II}Fe^{II}]^+/[Co^{I}Fe^{II}]$) and the reference complex couple ($Fc^{+/0}$), all the involved complexes were first optimized in acetonitrile (as an implicit solvent i.e., the solvent is represented by a dielectric constant) as proposed by Konezy et al.[166]

The free energy difference between $[Co^{II}Fe^{II}]^+$ and $[Co^{I}Fe^{II}]$ was calculated as well as the free energy difference between [Fc]+ and [Fc]. Thus using the following equation (equation 1), the absolute redox potentials of both the complex $[Co^{II}Fe^{II}]^+$ and the reference complex (RC) were obtained.

$$E_{abs}([Co^{II}Fe^{II}]^+/[Co^{I}Fe^{II}]) = \frac{-\Delta G}{nF} = \frac{-(G([Co^{I}Fe^{II}])-(G([Co^{II}Fe^{II}]^+)}{nF} \qquad (1)$$

$$E_{abs}([Fc]^+/[Fc]) = \frac{-\Delta G}{nF} = \frac{-(G([Fc])-(G([Fc]^+)}{nF} \qquad (2)$$

The redox potential of complex $[Co^{II}Fe^{II}]^+$ referenced to the ($Fc^{+/0}$) couple is thus calculated using the following equation:

$$E_{calc}([Co^{II}Fe^{II}]^+/[Co^{I}Fe^{II}]) = E_{abs}([Co^{II}Fe^{II}]^+/[Co^{I}Fe^{II}]) - E_{abs}([Fc]^+/[Fc]) \quad (3)$$

The results are represented in Tables 2.1 and 2.2.

Preparation of the graphite electrodes

The graphite rod electrodes (1.3 cm in diameter and 3 cm in length) are first sonicated in EtOH for 2 hours and then in deionized water for 1 hour. Ethanol and water are replenished after each 30 min during the sonication. Then it is dried in an oven at 120 °C overnight. The dried electrode is immersed in 0.5 mM CH_2Cl_2 solution

of the catalyst in the glove box under an inert atmosphere. After a half hour, it is removed from the solution and dried with a N_2 stream. Finally, the surface is washed with ethanol to remove any loosely bound catalyst on the surface, then with distilled water, and finally dried under N_2 flow before use in electrolysis experiments.

Preparation of the 0.1 M phosphate buffer

1.361 g of potassium dihydrogen phosphate (KH_2PO_4) and 3.5 g of disodium hydrogen phosphate (NaH_2PO_4) are dissolved in 200 ml of distilled H_2O. The pH is adjusted with 37% of HCl.

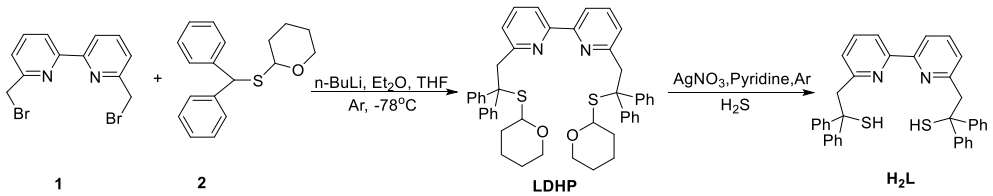

Figure 7.1 Synthesis of LDHP and H_2L ligands.

Synthesis of 6,6'-bis(2,2-diphenyl-2-((tetrahydro-2H-pyran-2-yl)thio)ethyl)-2,2'-bipyridine (LDHP)[167]

A solution of diphenylmethylthiol **2** (4.69 g, 16.51 mmol) in anhydrous diethyl ether (72 ml) is cooled down to -78°C with the colorless solution becoming a colorless precipitate. Then 6.50 mL of $LiBu^n$ (2.5 M in hexane) is added dropwise to give a yellow solution. The mixture solution is allowed to warm up to -10~ 0°C over 2 h and then cooled down again to -78℃. The reaction solution changed from yellow to orange-red (before -10°C) to a yellow precipitate (0°C) and finally returned to a yellow solution (-78°C) during this process. A solution of 6,6'-bis(bromomethyl)-2,2'-bipyridine (**1**, 2.47 g, 7.22 mmol) in THF (20 ml) with $P(NMe_2)_3O$ (15 ml), is added dropwise yielding a lightening of the reaction mixture from brown to yellow. The mixture is allowed to warm to 0°C over 4 h and then added to water. The organic layer is separated and the aqueous layer is extracted with ethyl acetate (3 ×140 ml). The combined organic layers are dried over Na_2SO_4 and filtered. After removal of the solvent, a small amount of acetone is added to crystallize a yellowish product. The product is filtered off and washed with methanol to afford 3.68 g (68%) of a 1:1 mixture of diastereoisomers.

Synthesis of 2,2'-[(2,2'-bipyridine)-6,6'-diyl]bis(1,1-diphenylethane-1-thiol) (H_2L)[167]

To a suspension of compound **LDHP** (3.40 g, 4.54 mmol) in ethyl acetate (14 ml) and methanol (106 ml) is added to a solution of $AgNO_3$ (1.76 g, 10.36 mmol) in pyridine (1.17 ml) and methanol (117 ml). The solid material dissolves immediately and the solution becomes yellow. After 5 h at room temperature the solvent is removed under vacuum yielding a yellow powder. The powder is dissolved in deaerated dichloromethane (20 ml) and H_2S is bubbled through the solution. The black precipitate is filtered off and washed with CH_2Cl_2. The combined filtrates are washed with saturated $NaHCO_3$ aqueous solution and the aqueous layer is extracted with

ether. The combined organic layers are dried over $NaSO_4$ and the solvent is removed to yield 2.10 g (80%) of the product as a white powder.

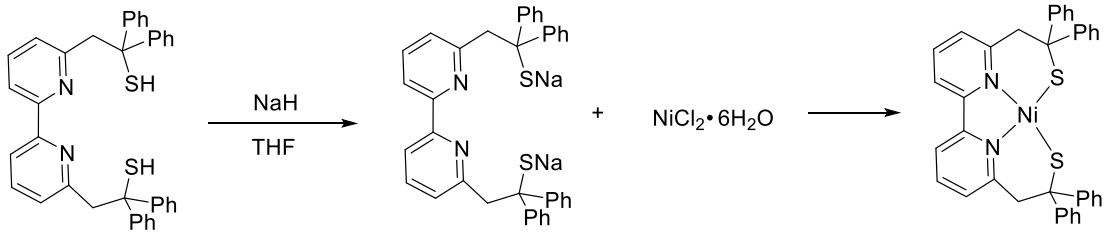

Figure 7.2 Synthesis of the NiL complex.

NiL^{N2S2} (NiL)[168]

H_2L (200 mg, 0.34 mmol) is added to a suspension of NaH (25 mg) in 12 ml of THF. After 20 min, $NiCl_2$•$6H_2O$ (84 mg, 0.35 mmol) is added to the yellow solution, with the consequent formation of a dark violet mixture. After 2 h, a dark purple solid is filtered and redissolved in $CHCl_3$ (excess). A residual solid is filtered off and the solvent is removed in vacuo. The resulting solid is washed with MeOH (20 ml), filtered, dried in vacuo, and collected as a purple powder (163 mg, 74%). UV-vis spectrum (in CH_2Cl_2): 501 nm and 560 nm. ESI-MS (in CH_2Cl_2, m/z): M = [NiL], 637.27 (M).

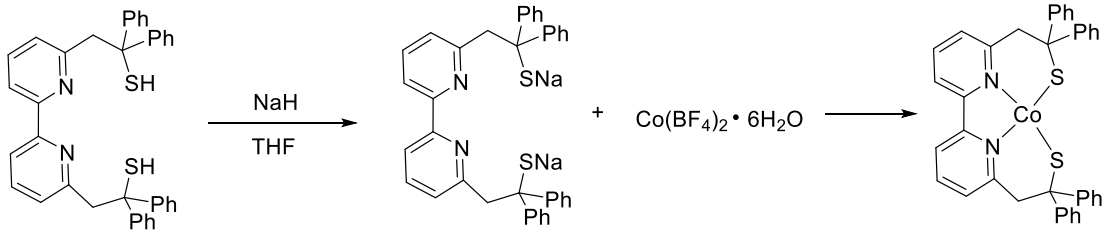

Figure 7.3 Synthesis of the CoL complex.

CoL^{N2S2} (CoL)[169]

H_2L (84 mg, 0.14 mmol) is added to a suspension of NaH (10 mg) in 5 mL of THF. After 20 min, $Co(BF_4)_2$•$6H_2O$ (51.7 mg, 0.15 mmol) is added to the yellow solution, with the consequent formation of a deep black mixture. After 2 h, the dark precipitate was filtered from the black solution, washed with THF (5 ml) and methanol (3 × 10 ml), dried, and collected as a dark brown powder (65 mg, 73%). UV-vis spectrum (in CH_2Cl_2): 416 nm, 491 nm and 769 nm. ESI-MS (in CH_2Cl_2, m/z): M = [CoL], 637.16 (M), 1274.28 (dimer, 2M).

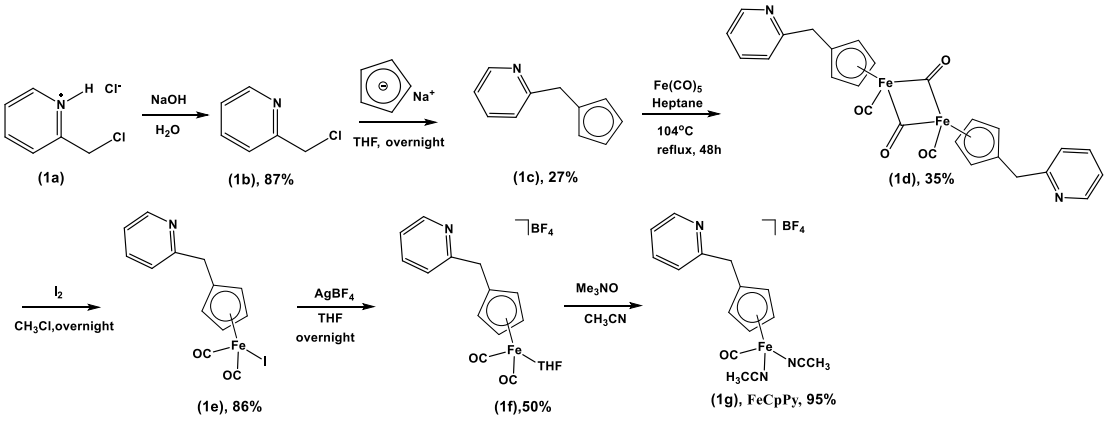

Figure 3.9 Synthetic route for the FePyCp complex.

Synthesis of PyCp (1c)

2-Picolyl chloride hydrochloride (**1a**, 10.60 g, 0.065 mol) is added to an aqueous solution of NaOH (4.07 g, 0.10 mol). The solution is extracted with Et_2O, and the organic layers are combined and dried with $NaSO_4$. The resulting product (1b, 7.61 g, 0.060 mol) is dissolved in 40 mL of THF and a solution of sodium cyclopentadienide (NaCp) in THF (2 M, 29.06 mL) is then slowly added dropwise at 0°C to give a dark brown solution. After overnight, the reaction solution is quenched with H_2O (150 ml), and the aqueous layer is extracted with Et_2O (3 *100 ml). The organic layers are combined and dried with $NaSO_4$. The solvent is removed in vacuo to yield dark brown oil. This dark brown oil is distilled at 80-100°C under vacuum to yield PyCp as a yellowish oil (2.6 g, 0.017 mol). ^{1}H NMR (400 MHz, $CDCl_3$): d 8.47 (m, 2H), 7.52(m, 2H), 7.11~7.08 (m, 2H), 7.06~7.03 (m, 2H), 6.37~6.02 (m, 6H), 3.86 (s, 2H), 3.83 (m, 2H), 2.93 (m, 2H), 2.85 (m, 2H).

Synthesis of $[Fe(CO)_2PyCp]_2$ (1d)

A solution of 2.6 g (0.017 mol) of **1c** is added to 50 mL of n-heptane. 4.2 ml (1.90 eq) of iron pentacarbonyl is then slowly added dropwise at 0°C to give a dark brown solution. The resulting mixture solution is heated at reflux for 40 h to yield a dark precipitate. After cooling down to room temperature, the dark precipitate is collected by filtration and washed with n-heptane to give a black solid (3.19 g, 35%). IR (oil) ν_{CO} (cm^{-1}): 1752 (s), 1975 (s). ESI-MS (in CH_2Cl_2+MeOH, m/z): M = $[Fe(CO)_2PyCp]_2$, 537.04 ($M+H^+$).

Synthesis of $[Fe(CO)_2PyCp(I)]$ (1e)

3.10 g (5.78 mmol) of **1d** is dissolved in 100 ml of chloroform and the solution is stirred in an ice bath for 30 min. I_2 (2.3 eq, 1.68 g) is dissolved in a chloroform solution and added slowly at 0°C to give a dark violet color solution. After overnight, the reaction solution is washed with saturated $Na_2S_2O_3$ aqueous solution (3X20 ml) and H_2O (2X50 ml). The aqueous layer is extracted with CH_2Cl_2 (3X 100 ml). The organic layers are combined and dried over Na_2SO_4 and the solvent is removed under reduced pressure to yield 1.96 g (86%) of the product as a brown oil. IR (oil) ν_{CO} (cm^{-1}): 1984 (s), 2025 (s). ESI-MS (in CH_2Cl_2, m/z): M = $[Fe(CO)_2PyCp(I)]$, 395.86 ($M+H^+$).

Synthesis of $[Fe(CO)_2PyCp(THF)]BF_4$ (1f)

1.38 g (3.49 mmol) of **1e** is dissolved in 20 ml of THF. A THF solution of $AgBF_4$ (0.68 g, 3.49 mmol) is added slowly in the dark to give a dark brown solution. After overnight, the volatile compounds are removed under reduced pressure, and the orange product is extracted with CH_2Cl_2, and filtered through a Celite plug. The solvent is removed under reduced pressure to yield 0.74 g (50%) of the product as a brown oil. IR (oil) ν_{CO} (cm^{-1}): 2028 (s), 2059 (s). ESI-MS (in CH_2Cl_2, m/z): M = $[Fe(CO)_2PyCp(THF)]^+$, 268.02 (M – THF). UV-vis spectrum (in MeCN): 356 nm.

Synthesis of $[Fe(CO)PyCp(MeCN)_2]BF_4$ (1g, FeCpPy)

40 mg (0.09 mmol) of **1f** is dissolved in 5 ml of MeCN solution. A MeCN solution of Me_3NO (1.0 eq, 6.76 mg) is added slowly to give a dark brown solution. After 20 min, the solvent is removed under reduced pressure, and the orange product is washed with n-pentane to give the product (35 mg, 95%) as a brown oil. FeCpPy easily loses its CO ligand and needs to be used as soon as possible for the next step. IR (oil) ν_{CO} (cm^{-1}): 1993 (s). UV-vis spectrum (in MeCN): 441 nm and 579 nm.

Synthesis of $[Fe(CO)HPyCp(MeCN)_2](BF_4)_2$(1g^H, FeCpPyH)

20 mg of **1g** (0.049 mmol) is dissolved in 2 ml of MeCN. A MeCN solution of $HBF_4 \bullet Et_2O$ (1.0 eq, 8 µl) is added slowly and the color of the solution changes from yellow to brown. After 20 min, the solvent is removed under reduced pressure, and the orange product is washed with n-pentane to give the product (24 mg, 98%) as a brown oil. IR (in MeCN) ν_{CO} (cm^{-1}): 1993 (s). UV-vis spectrum (in MeCN): 313 nm, 350 nm, 441 nm and 579 nm.

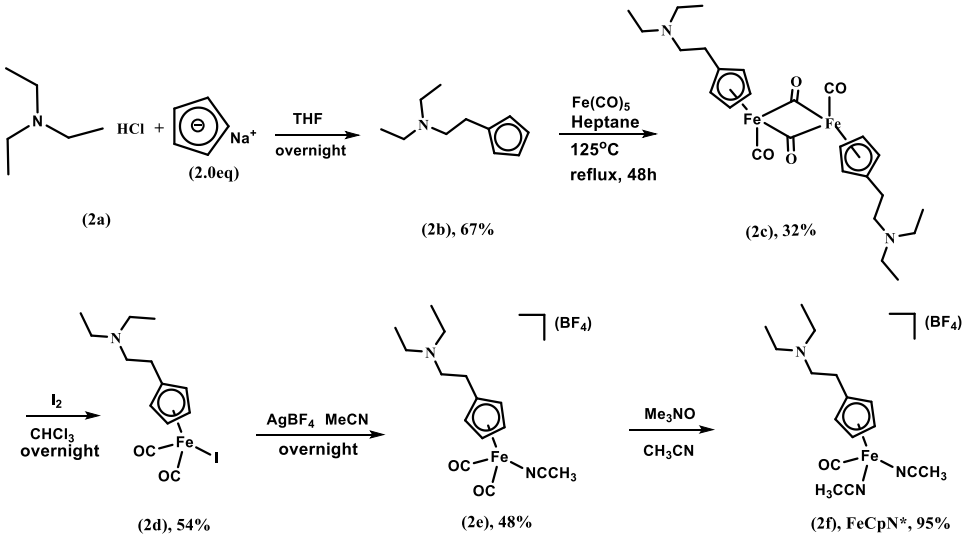

Figure 3.2 Synthetic route for the FeCpPy complex.

Synthesis of $Cp(CH_2)_2N(C_2H_5)_2$ (2b)[170]

2-Picolyl chloride hydrochloride (**2a**, 9.48 g, 0.054 mol) is dissolved in 200 ml of THF and a solution of NaCp in THF (2.4 M, 48.1 ml, 2.0 eq) is then slowly added dropwise at 0°C to give a dark red solution. The resulting solution is refluxed for 4 h. Then, the

reaction solution is quenched with H_2O (140 ml) and the organic phase is collected. The aqueous layer is extracted with Et_2O (3 *100 ml). All organic layers are combined and dried with $NaSO_4$. The solvent is removed in vacuo to yield dark brown oil. This dark brown oil is distilled at 80-100°C under vacuum to yield 5.97 g (67%) of **2b** as a yellowish oil. ESI-MS (in CH_2Cl_2, m/z): M = $[Cp(CH_2)_2N(C_2H_5)_2]$, 166.17 ($M+H^+$).

Synthesis of $[Fe(CO)_2CpN]_2$ (2c)

A solution of 3.3 g (0.020 mol) of **2b** is added to 150 mL of n-heptane. 5.12 mL (1.90 eq) of iron pentacarbonyl is then slowly added dropwise at 0°C to give a brown solution. The resulting mixture solution is heated at reflux for 40 h to yield a dark brown solution. After cooling down the solution to room temperature, the resulting solution is filtered and then dried in vacuo. This product was washed with n-heptane to give a brown oil with a yield of 32% (3.53 g). IR (oil) ν_{CO} (cm^{-1}): 1764 (s), 1958 (s). ESI-MS (in CH_2Cl_2+MeOH, m/z): M = $[Fe(CO)_2CpN]_2$, 553.19 ($M+H^+$).

Synthesis of $[Fe(CO)_2CpN(I)]$ (2d)

4.57 g (8.28 mmol) of **2c** is dissolved in 100 ml of chloroform and the solution is stirred in an ice bath for 30 min. I_2 (2.3 eq, 4.84 g) is dissolved in chloroform and added slowly at 0°C to give a dark violet color solution. After overnight, the reaction solution is washed with a saturated $Na_2S_2O_3$ aqueous solution (3 X 20 ml) and H_2O (2 X 50 ml). The aqueous layer is extracted with CH_2Cl_2 (3 X 100 ml). The organic layers are combined and dried over Na_2SO_4 and the solvent is removed to yield 54% (1.80 g) of the product as a brown oil. IR (oil) ν_{CO} (cm^{-1}): 1981 (s), 2027 (s). ESI-MS (in CH_2Cl_2, m/z): M = $[Fe(CO)_2CpN(I)]$, 404.07 ($M+H^+$). UV-vis spectrum (in MeCN): 359 nm.

Synthesis of $[Fe(CO)_2CpN(MeCN)]BF_4$ (2e)

0.32 g (0.79 mmol) of **2d** is dissolved in 20 ml of MeCN solution. A MeCN/THF solution of $AgBF_4$ (0.15 g) is added slowly in the dark to give a dark brown solution. After overnight, the volatile compounds are removed under reduced pressure; the orange product is extracted with CH_2Cl_2, and filtered through a Celite plug. The solvent is removed in vacuo to yield 48% (153 mg) of the product as a brown oil. IR (oil) ν_{CO} (cm^{-1}): 2027 (s), 2076 (s). ESI-MS (in CH_2Cl_2, m/z): M= $[Fe(CO)_2CpN(MeCN)]^+$, 317.09 (M), 276.01(M – MeCN). UV-vis spectrum (in MeCN): 320 nm and 376 nm.

Synthesis of $[Fe(CO)CpN(MeCN)_2]BF_4$ (2f, FeCpN)

24 mg (0.059 mmol) of **2e** is dissolved in 5 ml of MeCN. A MeCN solution of Me_3NO (1.0 eq, 8.8 mg) is added slowly to give a dark brown solution. After 20 min, the solvent is removed under reduced pressure, and the orange product is washed with n-pentane to give 95% (23 mg) of the product as a brown oil. IR (in CH_2Cl_2) ν_{CO} (cm^{-1}): 1984. UV-vis spectrum (in MeCN): 445 nm.

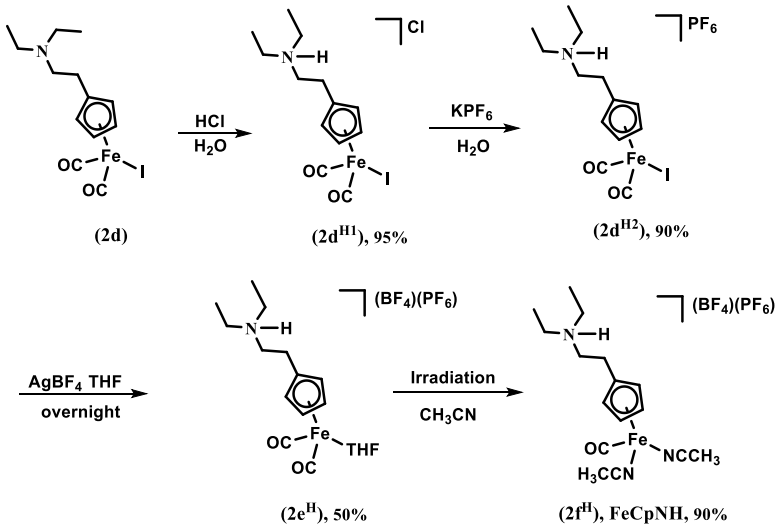

Figure 3.25 Synthetic route for the synthesis of FeCpNH complex.

Synthesis of $[Fe(CO)_2CpNHCl(I)]$ ($2d^{H1}$)

1.00 g (2.47 mmol) of **2d** is dissolved in 50 ml of CH_2Cl_2. Then an aqueous solution of HCl (37%, 1.1eq) is added to give a brown solution. The mixture solutions are shaken. The organic phase is separated. The aqueous layer is extracted with CH_2Cl_2 (3X50 ml). The organic layers are combined and dried over Na_2SO_4 and the solvent is removed in vacuo to yield 95% (1.03 g) of the product as a brown oil. IR (oil) ν_{CO} (cm^{-1}): 1981 (s), 2027 (s). ^1H NMR (400 HM_Z, CD_3CN): 8.35 (br, 1H, -NH), 5.26 (s, 2H), 4.95 (s, 2H), 3.35-3.22 (m, 8H), 1.38-1.34(m, 6H). ESI-MS (in CH_2Cl_2, m/z): M = $[Fe(CO)_2CpNHCl(I)]$, 404.05 (M-HCl+H^+). UV-vis spectrum (in MeCN): 357 nm.

Synthesis of $[Fe(CO)_2CpNH(I)]PF_6$ ($2d^{H2}$)

0.50 g (1.14 mmol) of $\mathbf{2d^{H1}}$ is dissolved in 5 ml of MeCN. Then a saturated KPF_6 aqueous is added. The aqueous layer is extracted with CH_2Cl_2 (3 X 20 ml). The organic layers are combined and dried over Na_2SO_4 and the solvent is removed in vacuo to yield 90% (562 mg) of the product as a brown oil. IR (oil) ν_{CO} (cm^{-1}): 1985 (s), 2032 (s). ^1H NMR (400 HM_Z, CD_3CN): 6.97 (br, 1H, -NH), 5.24 (m, 2H), 4.94 (m, 2H), 3.36-3.23 (m, 8H), 1.33-1.30(m, 6H). ESI-MS (in CH_2Cl_2, m/z): M = $[Fe(CO)_2CpNH(I)]^+$, 377.38 (M-CO+2H^+). UV-vis spectrum (in MeCN): 327 nm.

Synthesis of $[Fe(CO)_2CpNH(THF)](BF_4)(PF_6)$ ($2e^H$)

0.50 g (0.91 mmol) of $\mathbf{2d^{H2}}$ is dissolved in 40 ml of THF. A THF solution of $AgBF_4$ (0.17 g, 0.90 mmol) is added slowly in the dark to give a dark brown solution. After overnight, the volatile compounds are removed under reduced pressure, and the orange product is extracted with CH_2Cl_2, filtered through a Celite plug. The solvent is removed to yield 50% (264 mg) of the product as a brown oil. IR (oil) ν_{CO} (cm^{-1}): 2029 (s), 2078 (s). ^1H NMR (400 HM_Z, CD_3CN): 5.51 (m, 2H), 5.14 (m, 2H), 3.32-3.14 (m, 12H), 1.33-1.30(m, 10H). ESI-MS (in MeCN, m/z): M= $[Fe(CO)_2CpNH(THF)]^{2+}$, 317.17 (M – THF + MeCN). UV-vis spectrum (in MeCN): 375 nm.

Synthesis of $[Fe(CO)CpNH(MeCN)_2](BF_4)(PF_6)$ (FeCpNH, $2f^H$)

0.50 g (0.86 mmol) of $\mathbf{2e^H}$ is dissolved in 5 ml of MeCN and placed in an oven-dried Schlenk tube. This tube is carefully placed under a partial vacuum and exposed to a UV-filtered Hg/Xe lamp, resulting in the evolution of gas bubbles. The reaction is monitored by FTIR. After 16 h, the solution is filtered. The obtained oil is washed with n-pentane to give a brown oil corresponding to $\mathbf{2f^H}$ with a yield of 90% (435 mg). IR (in CH_2Cl_2) ν_{CO} (cm^{-1}): 1983 (s). UV-vis spectrum (in MeCN): 417 nm (broad).

Synthesis of $FeBr_2(CO)_2$dppv[155]

A THF (6 ml) solution of $FeBr_2$ (0.11 g, 0.50 mmol) and dppv (0.20 g, 0.50 mmol) is stirred and CO is through it bubbled at room temperature for 5 h. After the removal of the volatile compounds from the resulting mixture, the residue is purified by silica gel column chromatography using CH_2Cl_2 as an eluent. $FeBr_2(CO)_2$dppv is isolated as an orange-red solid (0.24 g, 72%). IR (solid) ν_{CO} (cm^{-1}): 2019 (s) and 2053 (m). ESI-MS (in CH_2Cl_2, m/z): M = $FeBr_2(CO)_2$dppv, 670.19 ($M - 2Br^- + 2H^+$).

Synthesis of $FeCl_2$dppe[157]

A solution of dppe (1.05 g, 2.63 mmol) in chloroform (4 ml) is added to an acetone (40 ml) solution of $FeCl_2 \bullet 4H_2O$ (0.52 g, 2.62 mmol) to give a yellowish solution. The mixture solution is refluxed for 20 h to give a turbid yellow solution. The yellow precipitate is separated by filtration, and washed three times with diethyl ether, dried under a vacuum, and isolated as a powder with a yield of 19% (260 mg).EPCI-MS (in MeCN, m/z): M = $FeCl_2$dppe, 431.21 (dppe+O_2+H^+); 556.09 (M+O_2+H^+).

Synthesis of the $[(L^{N2S2})Co^{II}Fe^{II}(CO)(Cp)]BF_4$ ($Co^{II}Fe^{II}Cp$)

Solid CoL (100 mg, 0.16 mmol) is added to a stirring solution of $[Fe^{II}(MeCN)_2COCp]BF_4$ (50 mg, 0.16 mmol) in 10 mL of CH_2Cl_2. After overnight, the dark black-brown solid product is filtered and washed with EtOH and dried under a vacuum to give $Co^{II}Fe^{II}Cp$ with a yield of 80% (111 mg). IR (solid) ν_{CO} (cm^{-1}): 1856 (s). ESI-MS (in CH_2Cl_2, m/z): M = $[(L^{N2S2})Co^{II}Fe^{II}(CO)(Cp)]^+$, 786.04 (M); 758.06 (M – CO). UV-vis spectrum (in CH_2Cl_2): 468 nm and 584 nm.

Synthesis of the $[(L^{N2S2})Co^{I}(CO)Fe^{II}(Cp)]$ ($Co^{I}Fe^{II}Cp$).

A slight excess of solid cobaltocene ($CoCp_2$, 23.8 mg) is added to a solution of $\mathbf{Co^{II}Fe^{II}Cp}$ (100 mg, 0.11 mmol) in 10 mL of MeCN. After 2 h, the dark brown-black solution turns to a purple suspension. The solid is filtered and washed with acetonitrile and dried under vacuum to give $Co^{I}Fe^{II}Cp$ with a yield of 85% (73 mg). IR (solid) ν_{CO} (cm^{-1}): 1734 (s). ESI-MS (in CH_2Cl_2, m/z): M = $[(L^{N2S2})Co^{I}Fe^{II}(CO)(Cp)]$, 786.0 (M). UV-vis spectrum (in CH_2Cl_2): 522 nm and 950 nm.

Synthesis of the $[(L^{N2S2})Ni^{II}Fe^{II}(CO)(CpPyH)](BF_4)$ (NiFeCpPy)

Solid **NiL** (32 mg, 0.05 mmol) is added to a stirring solution of **FeCpPyH** (25 mg, 0.05 mmol) in 10 mL of CH_2Cl_2. After overnight, the solvent is removed under a vacuum to

give a brown power. The resulting solid is washed with n-pentane and dried under a vacuum to give NiFeCpPy with a yield of 58% (30 mg). IR (in CH_2Cl_2) ν_{CO} (cm^{-1}): 1922 (s). ESI-MS (in CH_2Cl_2, m/z): M = $[(L^{N2S2})Ni^{II}Fe^{II}(CO)(CpPy)]^+$, 876.19 (M). UV-vis spectrum (in CH_2Cl_2): 391 nm, 497 nm, and 660 nm.

Synthesis of the $[(L^{N2S2})Ni^{II}Fe^{II}(CO)(CpN)]BF_4$ (NiFeCpN)

Solid **NiL** (38 mg, 0.06 mmol) is added to a stirring solution of **FeCpN** (25 mg, 0.06 mmol) in 10 mL of CH_2Cl_2. After 48 h, the solvent is removed under a vacuum to give a brown-red power. The resulting solid is washed with n-pentane and dried under a vacuum to give NiFeCpN with a yield of 66% (38 mg). IR (in CH_2Cl_2) ν_{CO} (cm^{-1}): 1928 (s). ESI-MS (in CH_2Cl_2, m/z): M = $[(L^{N2S2})Ni^{II}Fe^{II}(CO)(CpN)]^+$, 884.31 (M); 856.31 (M – CO). UV-vis spectrum (in CH_2Cl_2): 464 nm.

Synthesis of the $[(L^{N2S2})Co^{II}Fe^{II}(CO)(CpNH)](BF_4)(PF_6)$(CoFeCpNH)

Solid **CoL** (28 mg, 0.04 mmol) is added to a stirring solution of **FeCpNH** (25 mg, 0.04 mmol) in 10 mL of MeCN. After 48 h, the solvent is removed under a vacuum to give a brown power. The resulting solid is washed with n-pentane and dried under vacuum to give CoFeCpNH with a yield of 62% (28 mg). IR (in CH_2Cl_2) ν_{CO} (cm^{-1}): 1896 (s). ESI-MS (in CH_2Cl_2, m/z): M = $[(L^{N2S2})Co^{II}Fe^{II}(CO)(CpNH)]^+$, 885.24 (M); 857.24 (M – CO). UV-vis spectrum (in CH_2Cl_2): 456 nm and 563 nm.

References

1. Renssen, S. v., The hydrogen solution? *Nat. Clim. Change* **2020,** *10* (9), 799-801.
2. Lubitz, W.; Ogata, H.; Rudiger, O.; Reijerse, E., Hydrogenases. *Chem. Rev.* **2014,** *114* (8), 4081-4148.
3. Ogo, S.; Ichikawa, K.; Kishima, T.; Matsumoto, T.; Nakai, H.; Kusaka, K.; Ohhara, T., A functional [NiFe]hydrogenase mimic that catalyzes electron and hydride transfer from H_2. *science* **2013,** *339* (6120), 682-684.
4. Noussan, M.; Raimondi, P. P.; Scita, R.; Hafner, M., The Role of Green and Blue Hydrogen in the Energy Transition-A Technological and Geopolitical Perspective. *Sustainability* **2020,** *13* (1), 298.
5. Lubitz, W.; Ogata, H.; Rüdiger, O.; Reijerse, E., Hydrogenases. *Chem. Rev.* **2014,** *114* (8), 4081-4148.
6. Ghosh, A. C.; Duboc, C.; Gennari, M., Synergy between metals for small molecule activation: Enzymes and bio-inspired complexes. *Coord. Chem. Rev.* **2021,** *428*, 213606.
7. Schilter, D.; Camara, J. M.; Huynh, M. T.; Hammes-Schiffer, S.; Rauchfuss, T. B., Hydrogenase Enzymes and Their Synthetic Models: The Role of Metal Hydrides. *Chem. Rev.* **2016,** *116* (15), 8693-8749.
8. Simmons, T. R.; Berggren, G.; Bacchi, M.; Fontecave, M.; Artero, V., Mimicking hydrogenases: From biomimetics to artificial enzymes. *Coord. Chem. Rev.* **2014,** *270-271*, 127-150.
9. Ahmed, M. E.; Dey, A., Recent developments in bioinspired modelling of [NiFe]- and [FeFe]-hydrogenases. *Curr. Opin. Electrochem.* **2019,** *15*, 155-164.
10. Dawson, J.; Perotto, C.; McMaster, J.; Schröder, M., [NiFe] Hydrogenases. In *Bioinspired Catalysis*, Wiley-VCH Verlag GmbH & Co KGaA: 2014; pp 49-78.
11. Volbeda, A.; Charon, M. H.; Piras, C.; Hatchikian, E. C.; Frey, M.; Fontecilla-Camps, J. C., Crystal structure of the nickel-iron hydrogenase from Desulfovibrio gigas. *Nature* **1995,** *373* (6515), 580-587.
12. Nicolet, Y.; Piras, C.; Legrand, P.; Hatchikian, C. E.; Fontecilla-Camps, J. C., Desulfovibrio desulfuricans iron hydrogenase: the structure shows unusual coordination to an active site Fe binuclear center. *Structure* **1999,** *7* (1), 13-23.
13. Kleinhaus, J. T.; Wittkamp, F.; Yadav, S.; Siegmund, D.; Apfel, U. P., [FeFe]-Hydrogenases: maturation and reactivity of enzymatic systems and overview of biomimetic models. *Chem. Soc. Rev.* **2021,** *50* (3), 1668-1784.
14. Birrell, J. A.; Rodríguez-Maciá, P.; Reijerse, E. J.; Martini, M. A.; Lubitz, W., The catalytic cycle of [FeFe] hydrogenase: A tale of two sites. *Coord. Chem. Rev.* **2021,** *449*, 214191.
15. Ash, P. A.; Kendall-Price, S. E. T.; Vincent, K. A., Unifying Activity, Structure, and Spectroscopy of [NiFe] Hydrogenases: Combining Techniques To Clarify Mechanistic Understanding. *Acc. Chem. Res.* **2019,** *52* (11), 3120-3131.
16. Land, H.; Senger, M.; Berggren, G.; Stripp, S. T., Current State of [FeFe]-Hydrogenase Research: Biodiversity and Spectroscopic Investigations. *ACS Catal.* **2020,** *10* (13), 7069-7086.
17. Ogata, H.; Nishikawa, K.; Lubitz, W., Hydrogens detected by subatomic resolution protein crystallography in a [NiFe] hydrogenase. *Nature* **2015,** *520* (7548), 571-574.
18. Ogata, H.; Kramer, T.; Wang, H.; Schilter, D.; Pelmenschikov, V.; van Gastel, M.; Neese, F.; Rauchfuss, T. B.; Gee, L. B.; Scott, A. D.; Yoda, Y.; Tanaka, Y.; Lubitz, W.; Cramer, S. P.,

Hydride bridge in [NiFe]-hydrogenase observed by nuclear resonance vibrational spectroscopy. *Nat. Commun.* **2015,** *6*, 7890.

19. Mulder, D. W.; Guo, Y.; Ratzloff, M. W.; King, P. W., Identification of a Catalytic Iron-Hydride at the H-Cluster of [FeFe]-Hydrogenase. *J. Am. Chem. Soc.* **2017,** *139* (1), 83-86.

20. Winkler, M.; Senger, M.; Duan, J.; Esselborn, J.; Wittkamp, F.; Hofmann, E.; Apfel, U. P.; Stripp, S. T.; Happe, T., Accumulating the hydride state in the catalytic cycle of [FeFe]-hydrogenases. *Nat. Commun.* **2017,** *8*, 16115.

21. Reijerse, E. J.; Pham, C. C.; Pelmenschikov, V.; Gilbert-Wilson, R.; Adamska-Venkatesh, A.; Siebel, J. F.; Gee, L. B.; Yoda, Y.; Tamasaku, K.; Lubitz, W.; Rauchfuss, T. B.; Cramer, S. P., Direct Observation of an Iron-Bound Terminal Hydride in [FeFe]-Hydrogenase by Nuclear Resonance Vibrational Spectroscopy. *J. Am. Chem. Soc.* **2017,** *139* (12), 4306-4309.

22. Darensbourg, M. Y.; Lyon, E. J.; Smee, J. J., The bio-organometallic chemistry of active site iron in hydrogenases. *Coord. Chem. Rev.* **2000,** *206-207*, 533-561.

23. Böck, A.; King, P. W.; Blokesch, M.; Posewitz, M. C., Maturation of Hydrogenases. In *Advances in Microbial Physiology Volume 51*, 2006; pp 1-71.

24. Fontecilla-Camps, J. C.; Volbeda, A.; Cavazza, C.; Nicolet, Y., Structure/function relationships of [NiFe]- and [FeFe]-hydrogenases. *Chem. Rev.* **2007,** *107* (10), 4273-4303.

25. Tai, H.; Hirota, S., Mechanism and Application of the Catalytic Reaction of [NiFe] Hydrogenase: Recent Developments. *Chembiochem* **2020,** *21* (11), 1573-1581.

26. Tard, C.; Liu, X.; Ibrahim, S. K.; Bruschi, M.; Gioia, L. D.; Davies, S. C.; Yang, X.; Wang, L.-S.; Sawers, G.; Pickett, C. J., Synthesis of the H-cluster framework of iron-only hydrogenase. *Nature* **2005,** *433* (7026), 610-613.

27. Esmieu, C.; Guo, M.; Redman, H. J.; Lundberg, M.; Berggren, G., Synthesis of a miniaturized [FeFe] hydrogenase model system. *Dalton Trans.* **2019,** *48* (7), 2280-2284.

28. Camara, J. M.; Rauchfuss, T. B., Combining acid–base, redox and substrate binding functionalities to give a complete model for the [FeFe]-hydrogenase. *Nat. Chem.* **2011,** *4* (1), 26-30.

29. Lansing, J. C.; Camara, J. M.; Gray, D. E.; Rauchfuss, T. B., Hydrogen Production Catalyzed by Bidirectional, Biomimetic Models of the [FeFe]-Hydrogenase Active Site. *Organometallics* **2014,** *33* (20), 5897-5906.

30. Roy, S.; Groy, T. L.; Jones, A. K., Biomimetic model for [FeFe]-hydrogenase: asymmetrically disubstituted diiron complex with a redox-active 2,2'-bipyridyl ligand. *Dalton Trans.* **2013,** *42* (11), 3843-3853.

31. Orain, P. Y.; Capon, J. F.; Kervarec, N.; Gloaguen, F.; Petillon, F.; Pichon, R.; Schollhammer, P.; Talarmin, J., Use of 1,10-phenanthroline in diiron dithiolate derivatives related to the [Fe-Fe] hydrogenase active site. *Dalton Trans.* **2007,** (34), 3754-3756.

32. Wang, L.; Gennari, M.; Barrozo, A.; Fize, J.; Philouze, C.; Demeshko, S.; Meyer, F.; Orio, M.; Artero, V.; Duboc, C., Role of the Metal Ion in Bio-Inspired Hydrogenase Models: Investigation of a Homodinuclear FeFe Complex vs Its Heterodinuclear NiFe Analogue. *ACS Catal.* **2019,** *10* (1), 177-186.

33. Brazzolotto, D.; Gennari, M.; Queyriaux, N.; Simmons, T. R.; Pécaut, J.; Demeshko, S.; Meyer, F.; Orio, M.; Artero, V.; Duboc, C., Nickel-centred proton reduction catalysis in a model of [NiFe] hydrogenase. *Nat. Chem.* **2016,** *8* (11), 1054-1060.

34. Brazzolotto, D.; Wang, L.; Tang, H.; Gennari, M.; Queyriaux, N.; Philouze, C.; Demeshko, S.; Meyer, F.; Orio, M.; Artero, V.; Hall, M. B.; Duboc, C., Tuning Reactivity of

Bioinspired [NiFe]-Hydrogenase Models by Ligand Design and Modeling the CO Inhibition Process. *ACS Catal.* **2018,** *8* (11), 10658-10667.

35. Ahmed, M. E.; Saha, D.; Wang, L.; Gennari, M.; Ghosh Dey, S.; Artero, V.; Dey, A.; Duboc, C., An [FeFe] - Hydrogenase Mimic Immobilized through Simple Physiadsorption and Active for Aqueous H_2 Production. *ChemElectroChem* **2021,** *8* (9), 1674-1677.

36. Ahmed, M. E.; Chattopadhyay, S.; Wang, L.; Brazzolotto, D.; Pramanik, D.; Aldakov, D.; Fize, J.; Morozan, A.; Gennari, M.; Duboc, C.; Dey, A.; Artero, V., Hydrogen Evolution from Aqueous Solutions Mediated by a Heterogenized [NiFe]-Hydrogenase Model: Low pH Enables Catalysis through an Enzyme-Relevant Mechanism. *Angew. Chem. Int. Ed.* **2018,** *57* (49), 16001-16004.

37. Chambers, G. M.; Huynh, M. T.; Li, Y.; Hammes-Schiffer, S.; Rauchfuss, T. B.; Reijerse, E.; Lubitz, W., Models of the Ni-L and Ni-SIa States of the [NiFe]-Hydrogenase Active Site. *Inorg. Chem.* **2016,** *55* (2), 419-431.

38. Becker, R.; Amirjalayer, S.; Li, P.; Woutersen, S.; Reek, J. N., An iron-iron hydrogenase mimic with appended electron reservoir for efficient proton reduction in aqueous media. *Sci. Adv.* **2016,** *2* (1), e1501014.

39. Sommer, C.; Adamska-Venkatesh, A.; Pawlak, K.; Birrell, J. A.; Rudiger, O.; Reijerse, E. J.; Lubitz, W., Proton Coupled Electronic Rearrangement within the H-Cluster as an Essential Step in the Catalytic Cycle of [FeFe] Hydrogenases. *J. Am. Chem. Soc.* **2017,** *139* (4), 1440-1443.

40. Haumann, M.; Stripp, S. T., The Molecular Proceedings of Biological Hydrogen Turnover. *Acc. Chem. Res.* **2018,** *51* (8), 1755-1763.

41. Berggren, G.; Adamska, A.; Lambertz, C.; Simmons, T. R.; Esselborn, J.; Atta, M.; Gambarelli, S.; Mouesca, J. M.; Reijerse, E.; Lubitz, W.; Happe, T.; Artero, V.; Fontecave, M., Biomimetic assembly and activation of [FeFe]-hydrogenases. *Nature* **2013,** *499* (7456), 66-69.

42. Bourrez, M.; Steinmetz, R.; Gloaguen, F., Mechanistic insights into the catalysis of electrochemical proton reduction by a diiron azadithiolate complex. *Inorg. Chem.* **2014,** *53* (19), 10667-10673.

43. Aster, A.; Wang, S.; Mirmohades, M.; Esmieu, C.; Berggren, G.; Hammarstrom, L.; Lomoth, R., Metal vs. ligand protonation and the alleged proton-shuttling role of the azadithiolate ligand in catalytic H_2 formation with FeFe hydrogenase model complexes. *Chem. Sci.* **2019,** *10* (21), 5582-5588.

44. Zhao, P.-H.; Hu, M.-Y.; Li, J.-R.; Ma, Z.-Y.; Wang, Y.-Z.; He, J.; Li, Y.-L.; Liu, X.-F., Influence of Dithiolate Bridges on the Structures and Electrocatalytic Performance of Small Bite-Angle PNP-Chelated Diiron Complexes $Fe_2(\mu\text{-xdt})(CO)_4\{\kappa^2\text{-}(Ph_2P)_2NR\}$ Related to [FeFe]-Hydrogenases. *Organometallics* **2019,** *38* (2), 385-394.

45. Gao, S.; Liang, Q.; Duan, Q.; Jiang, D.; Zhao, J., Electrochemical proton reductions in varying acidic media by a simple synthetic hydrogenase mimic. *Int. J. Hydrog. Energy* **2018,** *43* (15), 7245-7256.

46. Quentel, F.; Gloaguen, F., Kinetic and thermodynamic aspects of the electrocatalysis of acid reduction in organic solvent using molecular diiron-dithiolate compounds. *Electrochim. Acta* **2013,** *110*, 641-645.

47. Carroll, M. E.; Barton, B. E.; Rauchfuss, T. B.; Carroll, P. J., Synthetic models for the active site of the [FeFe]-hydrogenase: catalytic proton reduction and the structure of the doubly protonated intermediate. *J. Am. Chem. Soc.* **2012,** *134* (45), 18843-18852.

48. Song, L.-C.; Liu, B.-B.; Liu, W.-B.; Tan, Z.-L., Heterodinuclear nickel(II)–iron(II) azadithiolates as

structural and functional models for the active site of [NiFe]-hydrogenases. *RSC Adv.* **2020,** *10* (53), 32069-32077.

49. Almazahreh, L. R.; Apfel, U.-P.; Imhof, W.; Rudolph, M.; Görls, H.; Talarmin, J.; Schollhammer, P.; El-khateeb, M.; Weigand, W., A Novel [FeFe] Hydrogenase Model with a $(SCH_2)_2P{=}O$ Moiety. *Organometallics* **2013,** *32* (16), 4523-4530.

50. Almazahreh, L. R.; Arrigoni, F.; Abul-Futouh, H.; El-khateeb, M.; Görls, H.; Elleouet, C.; Schollhammer, P.; Bertini, L.; De Gioia, L.; Rudolph, M.; Zampella, G.; Weigand, W., Proton Shuttle Mediated by $(SCH_2)_2P{=}O$ Moiety in [FeFe]-Hydrogenase Mimics: Electrochemical and DFT Studies. *ACS Catal.* **2021,** *11* (12), 7080-7098.

51. Greco, C.; Zampella, G.; Bertini, L.; Bruschi, M.; Fantucci, P.; De Gioia, L., Insights into the mechanism of electrocatalytic hydrogen evolution mediated by $Fe_2(S_2C_3H_6)(CO)_6$: the simplest functional model of the Fe-hydrogenase active site. *Inorg. Chem.* **2007,** *46* (1), 108-116.

52. Borg, S. J.; Behrsing, T.; Best, S. P.; Razavet, M.; Liu, X.; Pickett, C. J., Electron transfer at a dithiolate-bridged diiron assembly: electrocatalytic hydrogen evolution. *J. Am. Chem. Soc.* **2004,** *126* (51), 16988-16999.

53. Ding, S.; Ghosh, P.; Lunsford, A. M.; Wang, N.; Bhuvanesh, N.; Hall, M. B.; Darensbourg, M. Y., Hemilabile Bridging Thiolates as Proton Shuttles in Bioinspired H_2 Production Electrocatalysts. *J. Am. Chem. Soc.* **2016,** *138* (39), 12920-12927.

54. Tang, H.; Hall, M. B., Biomimetics of [NiFe]-Hydrogenase: Nickel- or Iron-Centered Proton Reduction Catalysis? *J. Am. Chem. Soc.* **2017,** *139* (49), 18065-18070.

55. Weber, K.; Kramer, T.; Shafaat, H. S.; Weyhermuller, T.; Bill, E.; van Gastel, M.; Neese, F.; Lubitz, W., A functional [NiFe]-hydrogenase model compound that undergoes biologically relevant reversible thiolate protonation. *J. Am. Chem. Soc.* **2012,** *134* (51), 20745-20755.

56. Tai, H.; Nishikawa, K.; Higuchi, Y.; Mao, Z. W.; Hirota, S., Cysteine SH and Glutamate COOH Contributions to [NiFe] Hydrogenase Proton Transfer Revealed by Highly Sensitive FTIR Spectroscopy. *Angew. Chem. Int. Ed.* **2019,** *58* (38), 13285-13290.

57. Tai, H.; Hirota, S.; Stripp, S. T., Proton Transfer Mechanisms in Bimetallic Hydrogenases. *Acc. Chem. Res.* **2021,** *54* (1), 232-241.

58. Ratzloff, M. W.; Artz, J. H.; Mulder, D. W.; Collins, R. T.; Furtak, T. E.; King, P. W., CO-Bridged H-Cluster Intermediates in the Catalytic Mechanism of [FeFe]-Hydrogenase CaI. *J. Am. Chem. Soc.* **2018,** *140* (24), 7623-7628.

59. Birrell, J. A.; Pelmenschikov, V.; Mishra, N.; Wang, H.; Yoda, Y.; Tamasaku, K.; Rauchfuss, T. B.; Cramer, S. P.; Lubitz, W.; DeBeer, S., Spectroscopic and Computational Evidence that [FeFe] Hydrogenases Operate Exclusively with CO-Bridged Intermediates. *J. Am. Chem. Soc.* **2020,** *142* (1), 222-232.

60. Zhao, X.; Georgakaki, I. P.; Miller, M. L.; Yarbrough, J. C.; Darensbourg, M. Y., H/D exchange reactions in dinuclear iron thiolates as activity assay models of Fe-H_2ase. *J. Am. Chem. Soc.* **2001,** *123* (39), 9710-9711.

61. Zhao, X.; Georgakaki, I. P.; Miller, M. L.; Mejia-Rodriguez, R.; Chiang, C. Y.; Darensbourg, M. Y., Catalysis of H_2/D_2 scrambling and other H/D exchange processes by [Fe]-hydrogenase model complexes. *Inorg. Chem.* **2002,** *41* (15), 3917-3928.

62. Fauvel, K.; Mathieu, R.; Poilblanc, R., Protonation of the metal-metal bond in $[\mu\text{-}(SCH_3)Fe(CO)_2L]_2$ complexes ($L = P(CH_3)_{3-x}(C_6H_5)_x$). Experimental evidence of the variation of nucleophilicity of the metal-metal bond with donor properties of phosphorus ligands. *Inorg. Chem.*

1976, *15* (4), 976-978.

63. Arabi, M. S.; Mathieu, R.; Poilblanc, R., Protonation of the metal-metal bond in $Fe_2(\mu\text{-}A)(\mu\text{-}A')(CO)_4L_2$ complexes (A=A′ =SC_6H_5, $P(C_6H_5)_2$, $P(CH_3)_2$; A=SC_6H_5, A′ =$P(C_6H_5)_2$; L=$P(C_6H_5)_{3-n}(CH_3)_n$). *J. Organomet. Chem.* **1979,** *177* (1), 199-209.

64. Matthews, S. L.; Heinekey, D. M., A Carbonyl-Rich Bridging Hydride Complex Relevant to the Fe-Fe Hydrogenase Active Site. *Inorg. Chem.* **2010,** *49* (21), 9746-9748.

65. Barton, B. E.; Rauchfuss, T. B., Terminal hydride in [FeFe]-hydrogenase model has lower potential for H_2 production than the isomeric bridging hydride. *Inorg. Chem.* **2008,** *47* (7), 2261-2263.

66. Justice, A. K.; Linck, R. C.; Rauchfuss, T. B.; Wilson, S. R., Dihydrogen activation by a diruthenium analogue of the Fe-only hydrogenase active site. *J. Am. Chem. Soc.* **2004,** *126* (41), 13214-13215.

67. van der Vlugt, J. I.; Rauchfuss, T. B.; Wilson, S. R., Electron-rich diferrous-phosphane-thiolates relevant to Fe-only hydrogenase: is cyanide "nature's trimethylphosphane"? *Chem.* **2005,** *12* (1), 90-98.

68. Nicolet, Y.; de Lacey, A. L.; Vernede, X.; Fernandez, V. M.; Hatchikian, E. C.; Fontecilla-Camps, J. C., Crystallographic and FTIR spectroscopic evidence of changes in Fe coordination upon reduction of the active site of the Fe-only hydrogenase from Desulfovibrio desulfuricans. *J. Am. Chem. Soc.* **2001,** *123* (8), 1596-1601.

69. Ogo, S.; Kabe, R.; Uehara, K.; Kure, B.; Nishimura, T.; Menon, S. C.; Harada, R.; Fukuzumi, S.; Higuchi, Y.; Ohhara, T.; Tamada, T.; Kuroki, R., A dinuclear Ni(μ-H)Ru complex derived from H_2. *science* **2007,** *316* (5824), 585-587.

70. Bertini, L.; Fantucci, P.; De Gioia, L.; Zampella, G., Excited state properties of diiron dithiolate hydrides: implications in the unsensitized photocatalysis of H_2 evolution. *Inorg. Chem.* **2013,** *52* (17), 9826-9841.

71. van Haaster, D. J.; Hagedoorn, P. L.; Jongejan, J. A.; Hagen, W. R., On the relationship between affinity for molecular hydrogen and the physiological directionality of hydrogenases. *Biochem. Soc. Trans.* **2005,** *33* (Pt 1), 12-14.

72. Huynh, M. T.; Schilter, D.; Hammes-Schiffer, S.; Rauchfuss, T. B., Protonation of nickel-iron hydrogenase models proceeds after isomerization at nickel. *J. Am. Chem. Soc.* **2014,** *136* (35), 12385-12395.

73. Barton, B. E.; Whaley, C. M.; Rauchfuss, T. B.; Gray, D. L., Nickel-iron dithiolato hydrides relevant to the [NiFe]-hydrogenase active site. *J. Am. Chem. Soc.* **2009,** *131* (20), 6942-6943.

74. Barton, B. E.; Rauchfuss, T. B., Hydride-containing models for the active site of the nickel-iron hydrogenases. *J. Am. Chem. Soc.* **2010,** *132* (42), 14877-14885.

75. Ulloa, O. A.; Huynh, M. T.; Richers, C. P.; Bertke, J. A.; Nilges, M. J.; Hammes-Schiffer, S.; Rauchfuss, T. B., Mechanism of H_2 Production by Models for the [NiFe]-Hydrogenases: Role of Reduced Hydrides. *J. Am. Chem. Soc.* **2016,** *138* (29), 9234-9245.

76. Ghosh, P.; Quiroz, M.; Wang, N.; Bhuvanesh, N.; Darensbourg, M. Y., Complexes of $MN_2S_2.Fe(\eta^5\text{-}C_5R_5)(CO)$ as platform for exploring cooperative heterobimetallic effects in HER electrocatalysis. *Dalton Trans.* **2017,** *46* (17), 5617-5624.

77. Chu, X.; Jin, J.; Ming, B.; Pang, M.; Yu, X.; Tung, C. H.; Wang, W., Bimetallic nickel-cobalt hydrides in H_2 activation and catalytic proton reduction. *Chem. Sci.* **2019,** *10* (3), 761-767.

78. Chu, X.; Yu, X.; Raje, S.; Angamuthu, R.; Ma, J.; Tung, C. H.; Wang, W., Synthetic [NiFe] models with a fluxional CO ligand. *Dalton Trans.* **2017,** *46* (40), 13681-13685.

79. Glass, R. S.; Pyun, J.; Lichtenberger, D. L.; Brezinski, W. P.; Karayilan, M.; Clary, K. E.; Pavlopoulos, N. G.; Evans, D. H., Water-soluble and air-stable [2Fe-2S]-metallopolymers: A new class of electrocatalysts for H_2 production via water splitting. *Phosphorus Sulfur Silicon Relat. Elem.* **2019,** *194* (7), 701-706.

80. Balestri, D.; Roux, Y.; Mattarozzi, M.; Mucchino, C.; Heux, L.; Brazzolotto, D.; Artero, V.; Duboc, C.; Pelagatti, P.; Marchio, L.; Gennari, M., Heterogenization of a [NiFe] Hydrogenase Mimic through Simple and Efficient Encapsulation into a Mesoporous MOF. *Inorg. Chem.* **2017,** *56* (24), 14801-14808.

81. Ahmed, M. E.; Chattopadhyay, S.; Wang, L.; Brazzolotto, D.; Pramanik, D.; Aldakov, D.; Fize, J.; Morozan, A.; Gennari, M.; Duboc, C.; Dey, A.; Artero, V., Hydrogen Evolution from Aqueous Solutions Mediated by a Heterogenized [NiFe]-Hydrogenase Model: Low pH Enables Catalysis through an Enzyme-Relevant Mechanism. *Angew. Chem. Int. Ed. Engl.* **2018,** *57* (49), 16001-16004.

82. Appel, A. M.; Bercaw, J. E.; Bocarsly, A. B.; Dobbek, H.; DuBois, D. L.; Dupuis, M.; Ferry, J. G.; Fujita, E.; Hille, R.; Kenis, P. J.; Kerfeld, C. A.; Morris, R. H.; Peden, C. H.; Portis, A. R.; Ragsdale, S. W.; Rauchfuss, T. B.; Reek, J. N.; Seefeldt, L. C.; Thauer, R. K.; Waldrop, G. L., Frontiers, opportunities, and challenges in biochemical and chemical catalysis of CO_2 fixation. *Chem. Rev.* **2013,** *113* (8), 6621-6658.

83. Wang, W. H.; Himeda, Y.; Muckerman, J. T.; Manbeck, G. F.; Fujita, E., CO_2 Hydrogenation to Formate and Methanol as an Alternative to Photo- and Electrochemical CO_2 Reduction. *Chem. Rev.* **2015,** *115* (23), 12936-12973.

84. Leung, C.-F.; Ho, P.-Y., Molecular Catalysis for Utilizing CO_2 in Fuel Electro-Generation and in Chemical Feedstock. *Catalysts* **2019,** *9* (9), 760.

85. Valluri, S.; Claremboux, V.; Kawatra, S., Opportunities and challenges in CO_2 utilization. *J. Environ. Sci. (China)* **2022,** *113*, 322-344.

86. Zhou, Z.-Y.; Sun, S.-G., A breakthrough in electrocatalysis of CO_2 conversion. *Natl. Sci. Rev.* **2017,** *4* (2), 155-156.

87. Kou, Z.; Li, X.; Wang, T.; Ma, Y.; Zang, W.; Nie, G.; Wang, J., Fundamentals, On-Going Advances and Challenges of Electrochemical Carbon Dioxide Reduction. *Electrochem. Energy Rev.* **2022,** *5* (1), 82-111.

88. Jhong, H.-R. M.; Ma, S.; Kenis, P. J. A., Electrochemical conversion of CO_2 to useful chemicals: current status, remaining challenges, and future opportunities. *Curr. Opin. Chem. Eng.* **2013,** *2* (2), 191-199.

89. Rakowski DuBois, M.; DuBois, D. L., Development of molecular electrocatalysts for CO_2 reduction and H_2 production/oxidation. *Acc. Chem. Res.* **2009,** *42* (12), 1974-1982.

90. Zhao, Z.; Lu, G., Circumventing the scaling relationship on bimetallic monolayer electrocatalysts for selective CO_2 reduction. *Chem. Sci.* **2022,** *13* (13), 3880-3887.

91. Yu, J.; Wang, J.; Ma, Y.; Zhou, J.; Wang, Y.; Lu, P.; Yin, J.; Ye, R.; Zhu, Z.; Fan, Z., Recent Progresses in Electrochemical Carbon Dioxide Reduction on Copper‐Based Catalysts toward Multicarbon Products. *Adv. Funct. Mater.* **2021,** *31* (37), 2102151.

92. Chen, Z.; Chen, C.; Weinberg, D. R.; Kang, P.; Concepcion, J. J.; Harrison, D. P.; Brookhart, M. S.; Meyer, T. J., Electrocatalytic reduction of CO_2 to CO by polypyridyl ruthenium complexes. *Chem. Commun.* **2011,** *47* (47), 12607-12609.

93. DuBois, D. L., Electrochemical Reactions of Carbon Dioxide. *10.1002/9783527610426.bard070602*.

94. Drennan, C. L.; Heo, J.; Sintchak, M. D.; Schreiter, E.; Ludden, P. W., Life on carbon monoxide: X-ray structure of Rhodospirillum rubrum Ni-Fe-S carbon monoxide dehydrogenase. *Proc. Natl. Acad. Sci. USA* **2001,** *98* (21), 11973-11978.

95. Jeoung, J. H.; Dobbek, H., Carbon dioxide activation at the Ni,Fe-cluster of anaerobic carbon monoxide dehydrogenase. *science* **2007,** *318* (5855), 1461-1464.

96. Trevino, R. E.; Shafaat, H. S., Protein-based models offer mechanistic insight into complex nickel metalloenzymes. *Curr. Opin. Chem. Biol.* **2022,** *67*, 102110.

97. Saha, P.; Amanullah, S.; Dey, A., Selectivity in Electrochemical CO_2 Reduction. *Acc. Chem. Res.* **2022,** *55* (2), 134-144.

98. Dey, S.; Ahmed, M. E.; Dey, A., Activation of Co(I) State in a Cobalt-Dithiolato Catalyst for Selective and Efficient CO_2 Reduction to CO. *Inorg. Chem.* **2018,** *57* (10), 5939-5947.

99. Cheng, M.; Yu, Y.; Zhou, X.; Luo, Y.; Wang, M., Chemical Versatility of [FeFe]-Hydrogenase Models: Distinctive Activity of $[\mu\text{-}C_6H_4\text{-}1,2\text{-}(\kappa^2\text{-}S)_2][Fe_2(CO)_6]$ for Electrocatalytic CO_2 Reduction. *ACS Catal.* **2018,** *9* (1), 768-774.

100. Ahmed, M. E.; Adam, S.; Saha, D.; Fize, J.; Artero, V.; Dey, A.; Duboc, C., Repurposing a Bio-Inspired NiFe Hydrogenase Model for CO_2 Reduction with Selective Production of Methane as the Unique C-Based Product. *ACS Energy Lett.* **2020,** *5* (12), 3837-3842.

101. Amanullah, S.; Saha, P.; Dey, A., Activating the Fe(I) State of Iron Porphyrinoid with Second-Sphere Proton Transfer Residues for Selective Reduction of CO_2 to HCOOH via Fe(III/II)-COOH Intermediate(s). *J. Am. Chem. Soc.* **2021,** *143* (34), 13579-13592.

102. Bose, P.; Mukherjee, C.; Golder, A. K., A NiII complex of the tetradentate salen ligand H_2L^{NH2} comprising an anchoring $-NH_2$ group: synthesis, characterization and electrocatalytic CO_2 reduction to alcohols. *Inorg. Chem. Front.* **2019,** *6* (7), 1721-1728.

103. Lubitz, W.; Ogata, H.; Rüdiger, O.; Reijerse, E., Hydrogenases. *Chem. Rev.* **2014,** *114* (8), 4081-4148.

104. Schilter, D.; Camara, J. M.; Huynh, M. T.; Hammes-Schiffer, S.; Rauchfuss, T. B., Hydrogenase Enzymes and Their Synthetic Models: The Role of Metal Hydrides. *Chem. Rev.* **2016,** *116* (15), 8693-8749.

105. Volbeda, A.; Charon, M.-H.; Piras, C.; Hatchikian, E. C.; Frey, M.; Fontecilla-Camps, J. C., Crystal structure of the nickel-iron hydrogenase from Desulfovibrio gigas. *Nature* **1995,** *373* (6515), 580-587.

106. Kaur-Ghumaan, S.; Stein, M., [NiFe] hydrogenases: how close do structural and functional mimics approach the active site? *Dalton Trans.* **2014,** *43* (25), 9392-9405.

107. Coutard, N.; Kaeffer, N.; Artero, V., Molecular engineered nanomaterials for catalytic hydrogen evolution and oxidation. *Chem. Commun.* **2016,** *52* (95), 13728-13748.

108. Kleinhaus, J. T.; Wittkamp, F.; Yadav, S.; Siegmund, D.; Apfel, U.-P., [FeFe]-Hydrogenases: maturation and reactivity of enzymatic systems and overview of biomimetic models. *Chem. Soc. Rev.* **2021,** *50* (3), 1668-1784.

109. Brazzolotto, D.; Gennari, M.; Queyriaux, N.; Simmons, T. R.; Pécaut, J.; Demeshko, S.; Meyer, F.; Orio, M.; Artero, V.; Duboc, C., Nickel-centred proton reduction catalysis in a model of [NiFe] hydrogenase. *Nat. Chem.* **2016,** *8*, 1054–1060.

110. Wang, L.; Gennari, M.; Barrozo, A.; Fize, J.; Philouze, C.; Demeshko, S.; Meyer, F.; Orio, M.; Artero, V.; Duboc, C., Role of the Metal Ion in Bio-Inspired Hydrogenase Models: Investigation of a Homodinuclear FeFe Complex vs Its Heterodinuclear NiFe Analogue. *ACS Catal.* **2020,**

10 (1), 177-186.

111. Ahmed, M. E.; Saha, D.; Wang, L.; Gennari, M.; Ghosh Dey, S.; Artero, V.; Dey, A.; Duboc, C., An [FeFe]-Hydrogenase Mimic Immobilized through Simple Physiadsorption and Active for Aqueous H_2 Production. *ChemElectroChem* **2021,** *8* (9), 1674-1677.

112. Gennari, M.; Duboc, C., Bio-inspired, Multifunctional Metal-Thiolate Motif: From Electron Transfer to Sulfur Reactivity and Small-Molecule Activation. *Acc. Chem. Res.* **2020,** *53* (11), 2753-2761.

113. Artero, V.; Saveant, J.-M., Toward the rational benchmarking of homogeneous H_2-evolving catalysts. *Energ. Environ. Sci.* **2014,** *7* (11), 3808-3814.

114. Luo, G.-G.; Zhang, H.-L.; Tao, Y.-W.; Wu, Q.-Y.; Tian, D.; Zhang, Q., Recent progress in ligand-centered homogeneous electrocatalysts for hydrogen evolution reaction. *Inorg. Chem. Front.* **2019,** *6* (2), 343-354.

115. Queyriaux, N.; Jane, R. T.; Massin, J.; Artero, V.; Chavarot-Kerlidou, M., Recent developments in hydrogen evolving molecular cobalt(II)–polypyridyl catalysts. *Coord. Chem. Rev.* **2015,** *304-305*, 3-19.

116. Dolui, D.; Khandelwal, S.; Majumder, P.; Dutta, A., The odyssey of cobaloximes for catalytic H_2 production and their recent revival with enzyme-inspired design. *Chem. Commun.* **2020,** *56* (59), 8166-8181.

117. Cutler, A. R.; Todaro, A. B., Characterization of the organometallic Lewis acid $(\eta^5\text{-}C_5H_5)(CO)Fe(OR_2)(\eta^2\text{-}CH_2{:}CHCH_3)^+BF_4^-$. *Organometallics* **1988,** *7* (8), 1782-1787.

118. Li, Y.; Zhou, L.; Guo, S., Noble metal-free electrocatalytic materials for water splitting in alkaline electrolyte. *EnergyChem* **2021,** *3* (2), 100053.

119. Tai, H.; Nishikawa, K.; Higuchi, Y.; Mao, Z. W.; Hirota, S., Cysteine SH and Glutamate COOH Contributions to [NiFe] Hydrogenase Proton Transfer Revealed by Highly Sensitive FTIR Spectroscopy. *Angew. Chem. Int. Ed. Engl.* **2019,** *58* (38), 13285-13290.

120. Fan, H. J.; Hall, M. B., A capable bridging ligand for Fe-only hydrogenase: density functional calculations of a low-energy route for heterolytic cleavage and formation of dihydrogen. *J. Am. Chem. Soc.* **2001,** *123* (16), 3828-3829.

121. Potter, G. D.; Baird, M. C.; Cole, S. P. C., A new series of titanocene dichloride derivatives bearing cyclic alkylammonium groups: Assessment of their cytotoxic properties. *J. Organomet. Chem.* **2007,** *692* (16), 3508-3518.

122. Enders, M.; Fernández, P.; Kaschke, M.; Kohl, G.; Ludwig, G.; Pritzkow, H.; Rudolph, R., Coordination chemistry of neutral quinolyl- and aminophenylcyclopentadiene derivatives. *J. Organomet. Chem.* **2002,** *641* (1-2), 81-89.

123. Zhang, S.; Liu, K.; Zhu, B., Reactions of pyridine-2-ethyl/methyl cyclopentadienes with metal carbonyls. *J. Coord. Chem.* **2018,** *71* (16-18), 2965-2977.

124. Brazzolotto, D.; Gennari, M.; Queyriaux, N.; Simmons, T. R.; Pecaut, J.; Demeshko, S.; Meyer, F.; Orio, M.; Artero, V.; Duboc, C., Nickel-centred proton reduction catalysis in a model of [NiFe] hydrogenase. *Nat. Chem.* **2016,** *8* (11), 1054-1060.

125. Causey, P. W.; Baird, M. C.; Cole, S. P. C., Synthesis, Characterization, and Assessment of Cytotoxic Properties of a Series of Titanocene Dichloride Derivatives. *Organometallics* **2004,** *23* (19), 4486-4494.

126. Ezzaher, S.; Capon, J. F.; Gloaguen, F.; Petillon, F. Y.; Schollhammer, P.; Talarmin, J., Influence of a pendant amine in the second coordination sphere on proton transfer at a dissymmetrically disubstituted diiron system related to the [2Fe]H subsite of $[FeFe]H_2$ase. *Inorg. Chem.*

2009, *48* (1), 2-4.

127. Olsen, M. T.; Rauchfuss, T. B.; Wilson, S. R., Role of the azadithiolate cofactor in models for [FeFe]-hydrogenase: novel structures and catalytic implications. *J. Am. Chem. Soc.* **2010,** *132* (50), 17733-17740.

128. Eilers, G.; Schwartz, L.; Stein, M.; Zampella, G.; de Gioia, L.; Ott, S.; Lomoth, R., Ligand versus metal protonation of an iron hydrogenase active site mimic. *Chem.* **2007,** *13* (25), 7075-7084.

129. Fourmond, V.; Jacques, P. A.; Fontecave, M.; Artero, V., H_2 evolution and molecular electrocatalysts: determination of overpotentials and effect of homoconjugation. *Inorg. Chem.* **2010,** *49* (22), 10338-10347.

130. Ghosh, P.; Quiroz, M.; Wang, N.; Bhuvanesh, N.; Darensbourg, M. Y., Complexes of MN2S2.Fe(eta(5)-C5R5)(CO) as platform for exploring cooperative heterobimetallic effects in HER electrocatalysis. *Dalton Trans.* **2017,** *46* (17), 5617-5624.

131. Queyriaux, N.; Sun, D.; Fize, J.; Pecaut, J.; Field, M. J.; Chavarot-Kerlidou, M.; Artero, V., Electrocatalytic Hydrogen Evolution with a Cobalt Complex Bearing Pendant Proton Relays: Acid Strength and Applied Potential Govern Mechanism and Stability. *J. Am. Chem. Soc.* **2020,** *142* (1), 274-282.

132. Gao, S.; Liu, Y.; Shao, Y.; Jiang, D.; Duan, Q., Iron carbonyl compounds with aromatic dithiolate bridges as organometallic mimics of [FeFe] hydrogenases. *Coordination Chemistry Reviews* **2020,** *402*.

133. Walaijai, K.; Cavill, S. A.; Whitwood, A. C.; Douthwaite, R. E.; Perutz, R. N. J. I. C., Electrocatalytic proton reduction by a cobalt (III) hydride complex with phosphinopyridine PN ligands. **2020,** *59* (24), 18055-18067.

134. Kaeffer, N.; Chavarot-Kerlidou, M.; Artero, V., Hydrogen evolution catalyzed by cobalt diimine-dioxime complexes. *Acc. Chem. Res.* **2015,** *48* (5), 1286-1295.

135. Canaguier, S.; Field, M.; Oudart, Y.; Pecaut, J.; Fontecave, M.; Artero, V., A structural and functional mimic of the active site of NiFe hydrogenases. *Chem. Commun. (Camb)* **2010,** *46* (32), 5876-8.

136. Zhu, W.; Marr, A. C.; Wang, Q.; Neese, F.; Spencer, D. J.; Blake, A. J.; Cooke, P. A.; Wilson, C.; Schroder, M., Modulation of the electronic structure and the Ni-Fe distance in heterobimetallic models for the active site in [NiFe]hydrogenase. *Proc. Natl. Acad. Sci. USA* **2005,** *102* (51), 18280-5.

137. DuBois, D. L., Development of molecular electrocatalysts for energy storage. *Inorg. Chem.* **2014,** *53* (8), 3935-3960.

138. Chambers, G. M.; Johnson, S. I.; Raugei, S.; Bullock, R. M., Anion control of tautomeric equilibria: Fe-H vs. N-H influenced by NH...F hydrogen bonding. *Chem. Sci.* **2019,** *10* (5), 1410-1418.

139. Evans, D., Chemistry relating to the nickel enzymes CODH and ACS. *Coord. Chem. Rev.* **2005,** *249* (15-16), 1582-1595.

140. Can, M.; Armstrong, F. A.; Ragsdale, S. W., Structure, function, and mechanism of the nickel metalloenzymes, CO dehydrogenase, and acetyl-CoA synthase. *Chem. Rev.* **2014,** *114* (8), 4149-4174.

141. Sinhababu, S.; Lakliang, Y.; Mankad, N. P., Recent advances in cooperative activation of CO_2 and N_2O by bimetallic coordination complexes or binuclear reaction pathways. *Dalton Trans.* **2022,** *51* (16), 6129-6147.

142. Liu, D.-C.; Zhong, D.-C.; Lu, T.-B., Non-noble metal-based molecular complexes for CO_2 reduction: From the ligand design perspective. *EnergyChem* **2020,** *2* (3), 100034.

143. Abdinejad, M.; Seifitokaldani, A.; Dao, C.; Sargent, E. H.; Zhang, X.-a.; Kraatz, H. B., Enhanced Electrochemical Reduction of CO_2 Catalyzed by Cobalt and Iron Amino Porphyrin Complexes. *ACS Appl. Energy Mater.* **2019,** *2* (2), 1330-1335.

144. Zhu, D. D.; Liu, J. L.; Qiao, S. Z. J. A. m., Recent advances in inorganic heterogeneous electrocatalysts for reduction of carbon dioxide. *Adv. Mater.* **2016,** *28* (18), 3423-3452.

145. Song, Y.; Chen, W.; Zhao, C.; Li, S.; Wei, W.; Sun, Y., Metal-Free Nitrogen-Doped Mesoporous Carbon for Electroreduction of CO_2 to Ethanol. *Angew. Chem. Int. Ed.* **2017,** *56* (36), 10840-10844.

146. Torbensen, K.; Boudy, B.; Joulié, D.; von Wolff, N.; Robert, M., Emergence of CO_2 electrolyzers including supported molecular catalysts. *Curr. Opin. Electrochem.* **2020,** *24*, 49-55.

147. Ahmed, M. E.; Nayek, A.; Krizan, A.; Coutard, N.; Morozan, A.; Ghosh Dey, S.; Lomoth, R.; Hammarstrom, L.; Artero, V.; Dey, A., A Bidirectional Bioinspired [FeFe]-Hydrogenase Model. *J. Am. Chem. Soc.* **2022,** *144* (8), 3614-3625.

148. Turner, J. A. J. S., Sustainable hydrogen production. *science* **2004,** *305* (5686), 972-974.

149. Zhao, J.; Shi, Q.; Song, D.; Li, B.; Ren, H.; Zhang, D.; Sun, X.; Li, J.; Wang, N., Effect of the NiN_2S_2 Metallothiolate Ligands on the Preparation, Structure, and Property of Dinickel Complexes Related to [NiFe]-Hydrogenases Active Site. *Catal. Lett.* **2021**, 98–105.

150. Isegawa, M.; Matsumoto, T.; Ogo, S., H_2 activation by hydrogenase-inspired NiFe catalyst using frustrated Lewis pair: effect of buffer and halide ion in the heterolytic H–H bond cleavage. *RSC Adv.* **2021,** *11* (45), 28420-28432.

151. Ohki, Y.; Tatsumi, K., Thiolate-Bridged Iron-Nickel Models for the Active Site of [NiFe] Hydrogenase. *Eur. J. Inorg. Chem.* **2010,** *2011* (7), 973-985.

152. Ogo, S.; Kishima, T.; Yatabe, T.; Miyazawa, K.; Yamasaki, R.; Matsumoto, T.; Ando, T.; Kikkawa, M.; Isegawa, M.; Yoon, K. S.; Hayami, S., [NiFe], [FeFe], and [Fe] hydrogenase models from isomers. *Sci. Adv.* **2020,** *6* (24), eaaz8181.

153. Carroll, M. E.; Barton, B. E.; Gray, D. L.; Mack, A. E.; Rauchfuss, T. B., Active-site models for the nickel-iron hydrogenases: effects of ligands on reactivity and catalytic properties. *Inorg. Chem.* **2011,** *50* (19), 9554-9563.

154. Carroll, M. E.; Chen, J.; Gray, D. E.; Lansing, J. C.; Rauchfuss, T. B.; Schilter, D.; Volkers, P. I.; Wilson, S. R., Ferrous Carbonyl Dithiolates as Precursors to FeFe, FeCo, and FeMn Carbonyl Dithiolates. *Organometallics* **2014,** *33* (4), 858-867.

155. Song, L.-C.; Hong, D.-J.; Guo, Y.-Q.; Wang, X.-Y., Dinuclear $Fe^{II}Fe^{II}$ Biomimetics for the Oxidized State Active Site of [FeFe]-Hydrogenases: Synthesis, Characterization, and Electrocatalytic H_2 Production. *Organometallics* **2018,** *37* (24), 4744-4752.

156. Basu, D.; Gray, D. L.; Woods, T. J.; Rauchfuss, T. B.; Arrigoni, F.; Zampella, G., Challenges in the Synthesis of Active Site Mimics for [NiFe]-Hydrogenases. *Organometallics* **2021,** *40* (19), 3306-3312.

157. Langer, R.; Bönisch, F.; Maser, L.; Pietzonka, C.; Vondung, L.; Zimmermann, T. P., Substitutional Lability of Diphosphine Ligands in Tetrahedral Iron(II) Chloro Complexes. *Eur. J. Inorg. Chem.* **2014,** *2015* (1), 141-148.

158. Akita, M.; Terada, M.; Tanaka, M.; Morooka, Y., Some additional aspects of versatile starting compounds for cationic organoiron complexes: molecular structure of the aqua complex $[(\eta^5\text{-}C_5Me_4Et)Fe(CO)_2(OH_2)]BF_4$ and solution behavior of the THF complex $[(\eta^5\text{-}C_5R_5)Fe(CO)_2(THF)]BF_4$. *J. Organomet. Chem.* **1996,** *510* (1-2), 255-261.

159. Frisch, M. J. T., G. W.; Schlegel, H. B.; Scuseria, G. E.; Robb, M. A.; Cheeseman, J.; R.; Scalmani, G. B., V.; Mennucci, B.; Petersson, G. A.; et al., Gaussian 09 Revision D.01. Gaussian Inc. Wallingford CT **2009**. **2009**.

160. Becke, A. D. J. P. r. A., Density-functional exchange-energy approximation with correct asymptotic behavior. **1988,** *38* (6), 3098.

161. Perdew, J. P., Density-functional approximation for the correlation energy of the inhomogeneous electron gas. *Phys. Rev. B* **1986,** *33* (12), 8822-8824.

162. Becke, A. D., Density‐functional thermochemistry. III. The role of exact exchange. *J. Chem. Phys.* **1993,** *98* (7), 5648-5652.

163. Weigend, F., Ahlrichs, Reinhart Balanced basis sets of split valence, triple zeta valence and quadruple zeta valence quality for H to Rn: Design and assessment of accuracy. *PCCP* **2005,** *7* (18), 3297-3305.

164. Weigend, F., Accurate Coulomb-fitting basis sets for H to Rn. *Phys. Chem. Chem. Phys.* **2006,** *8* (9), 1057-1065.

165. Tomasi, J.; Mennucci, B.; Cancès, E., The IEF version of the PCM solvation method: an overview of a new method addressed to study molecular solutes at the QM ab initio level. *J. Mol. Struct. THEOCHEM* **1999,** *464* (1-3), 211-226.

166. Konezny, S. J.; Doherty, M. D.; Luca, O. R.; Crabtree, R. H.; Soloveichik, G. L.; Batista, V. S. J. T. J. o. P. C. C., Reduction of systematic uncertainty in DFT redox potentials of transition-metal complexes. *J. Phys. Chem. C* **2012,** *116* (10), 6349-6356.

167. Kopf, M.-A.; Varech, D.; Tuchagues, J.-P.; Mansuy, D.; Artaud, I., New intermediate-spin chloroiron (III) complex with a mixed nitrogen–sulfur co-ordination sphere. *J. Chem. Soc., Dalton Trans.* **1998,** (6), 991-998.

168. Gennari, M.; Orio, M.; Pecaut, J.; Neese, F.; Collomb, M. N.; Duboc, C., Reversible apical coordination of imidazole between the Ni(III) and Ni(II) oxidation states of a dithiolate complex: a process related to the Ni superoxide dismutase. *Inorg. Chem.* **2010,** *49* (14), 6399-6401.

169. Gennari, M.; Gerey, B.; Hall, N.; Pecaut, J.; Vezin, H.; Collomb, M. N.; Orio, M.; Duboc, C., Structural, spectroscopic and redox properties of a mononuclear Co(II) thiolate complex--the reactivity toward S-alkylation: an experimental and theoretical study. *Dalton Trans.* **2012,** *41* (40), 12586-12594.

170. Mrózek, O.; Šebestová, L.; Vinklárek, J.; Řezáčová, M.; Eisner, A.; Růžičková, Z.; Honzíček, J., Highly Water-Soluble Cyclopentadienyl and Indenyl Molybdenum(II) Complexes-Second Generation of Molybdenum-Based Cytotoxic Agents. *Eur. J. Inorg. Chem.* **2016,** *2016* (4), 519-529.